Fakultät für Physik der
Technischen Universität München

Abteilung Molekulare Strukturbiologie
Max-Planck Institut für Biochemie

From Axons to Synapses:
Cryo-Electron Tomography of Neurons

Nikolas Johannes Schrod

Vollständiger Abdruck der von der Fakultät für Physik
der Technischen Universität München
zur Erlangung des akademischen Grades eines
Doktors der Naturwissenschaften (Dr. rer. nat.)
genehmigten Dissertation.

Vorsitzender: Univ.-Prof. Dr. M. Zacharias
Prüfer der Dissertation: 1. Hon.-Prof. Dr. W. Baumeister
                       2. Univ.-Prof. Dr. M. Rief

Die Dissertation wurde am 07.07.2016 bei der Technischen Universität München
eingereicht und durch die Fakultät für Physik am 04.10.2016 angenommen.

Contents

Chapter 1

Abstract

Cryo-electron tomography can provide an open view into the unaltered ultrastructure of neurons. We obtained tomograms of the distal regions of vitrified neuronal processes in developing neurons. We characterized the morphology of axonal processes and their content. In addition we analyzed synaptic vesicles, their distribution and interconnectivity in a quantitative matter.

Two additional studies have been performed in synaptosomes. We investigated the influence of human α-Synuclein on the synaptic ultrastructure by comparing different genotypes: synuclein-triple knockout, human α-Synuclein overexpression on wildtype and triple-knockout background as well as mice overexpressing the α-Synuclein A30P mutation linked to Parkinson's disease. In a separate study, SynCAM I overexpressor and knockout mice have been used to determine the distribution of SynCAM I within the synaptic cleft, revealing a preferential localization towards the edge of the synaptic cleft.

Chapter 2

Summary of studies described in this work

Neuronal cultures: During development neurons form many varicosities among their dendrites and axons. In axons they often transport packages of vesicles or other membranous structures carrying proteins required for synaptogenesis, or even represent functioning presynaptic boutons. By using cryo-electron tomography we obtained three dimensional tomograms of fully hydrated neuronal processes in vitro. Our analysis focused on axonal varicosities, especially those rich in synaptic vesicles or containing packs of synaptic vesicles. We furthermore employed a correlated microscopy approach, using cryo-light microscopy imaging of vitrified specimen before imaging in the electron microscope to target presynaptic boutons.

We observed and categorized a wide range of varicosities of varying morphology and content. We were able to describe multiple (putative) transport events and reveal connections between packets of synaptic vesicles to microtubules and to the network of smooth endoplasmic reticulum. We performed a quantitative analysis of the distribution of synaptic vesicles in boutons and the filamentous connectors between them. Automated segmentation methods were used to visualize cortical actin and actin bundles in varicosities and filopodia.

Correlative light and electron microscopy was used to target synaptic vesicle release and recycling events. Although we could successfully image several presynaptic boutons in axons we could not access mature synapses without further thinning steps.

α-Synuclein: α-Synuclein is the main component of Lewy-bodies associated with Parkinson's disease. Despite many efforts, its function in the healthy brain

is still unclear. Using synaptosomes from brains of mice we tried to elucidate the role of α-Synuclein by detecting differences in the distribution of synaptic vesicles, their interconnections and their tethering to the membrane at different levels of α-Synuclein. We investigated mice with either normal synuclein levels, with a triple-kockout of α-Synuclein, overexpressing native human α-Synuclein on wild-type or on triple-knockout background, as well as mice overexpressing the A30P mutation variant of alpha-synuclein on wild-type background. Humans with the A30P α-Synuclein mutation are prone to Parkinson's disease. α-Synuclein knock-out reduced the amount of filamentous connections among synaptic vesicles and they showed more structural indicators of release competence. Synaptosomes prepared from mice overexpressing human α-Synuclein revealed release defects not present in mice overexpressing the mutant A30P variant. Interestingly, overexpressin of α-Synuclein often showed different effects depending on the genetic background (wild-type or triple-knockout).

SynCAM I: SynCAM I is a protein in the synaptic cleft that plays an important role in synaptogenesis and synaptic plasticity. In order to visualize the synaptic cleft and investigate the distribution of SynCAM, together with Geoffrey Kong we established a collaboration with Geoffrey-Kong and Tom Blanpied. Cryo-electron tomography of synaptosomes prepared from mouse genotypes lacking or overexpressing SynCAM I revealed a preferential location of SynCAM I towards the edge of the synaptic cleft. This could be confirmed by superresolution microscopy data and immunolabeling experiments, both performed by Thomas Biederer's lab.

Chapter 3

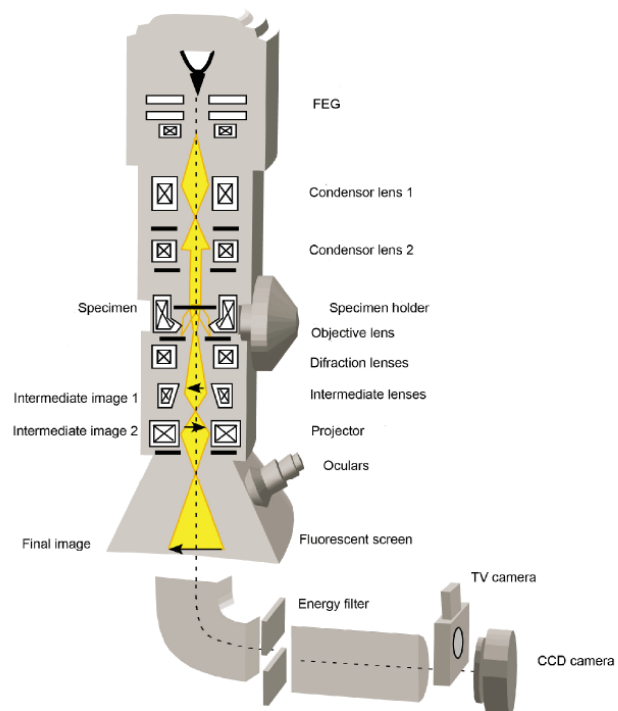# Electron microscopy

3.1   Electron microscopy

Since its introduction in 1932 by Ruska and Knoll [50], electron microscopy (EM) has seen huge developments and has advanced our knowledge in fields from solid state physics to life science and medicine. While electron microscopy does not require crystallized specimen, biological samples need to be immobilized to resist the vacuum in the electron microscope. In conventional electron microscopy, samples are fixed with aldehydes (formaldehydes and glutaraldehydes) to preserve their structure. After the chemical fixation the water is replaced by an epoxy resign. Chemical fixation and resin embedding was the fixation method of choice until the advent of cryo-electron microscopy. Cooling speeds of $> 10^5$ Kelvin per second solidify the water in and around the specimen in a vitreous state and preserve the ultrastructure even on the scale of proteins [22].

The setup of an electron microscope is analogous to a classic light microscope (see fig. 3.1) in the sense that it comprises an electron source, an array of lenses to manipulate the beam and the resulting image and a camera.

In light microscopy the resolution d is mainly limited by the wavelength of visible light: $d = \frac{\lambda}{2n \sin \theta}$, with λ between 400 nm and 700 nm. The wavelength of the electrons depends on their velocity and is small compared to visible light with 1.97 pm at 300 kV acceleration voltage[1]. When a sample is irradiated with the beam in the electron microscope, the incident electrons deposit energy in the sample, leading to its degradation. This effect limits the dose that can be applied to the specimen and hence the obtainable signal to noise ratio (SNR). It is especially

---

[1] $\lambda = \frac{h}{\sqrt{2m_0 eU}} \cdot \frac{1}{1 + \frac{eU}{2m_0 c^2}}$

Figure 3.1: Schematic representation of an electron microscope. From [84]

prominent in cryo-electron microscopy (cryo-EM) where the electron dose that can be applied to the specimen is much lower compared to electron microscopy of conventionally fixed specimen. Aside from electron sensitivity of the specimen, the specimen thickness is another limiting factor. Electrons that undergo multiple scattering events add additional noise to the image and reduce the attainable resolution. Additionally, not all spacial frequencies are represented equally in the acquired image. This is described by the contrast transfer function (CTF), see section 3.3 below.

Electron source

Nowadays the illumination source of choice in the electron microscope is a field emission gun (FEG). The electron beam it provides has a higher temporal and spacial coherence compared to thermionic or Lathidium-Hexabromide emission guns. This is important for the resulting image formation as it decreases the attenuation of the CTF (see fig. 3.2).

A FEG consists of a Schottky type tungsten crystal and two anodes, operated at around 1700 K. The sharp (100nm) tip of the crystal is covered by a thin layer of zirconia to lower the work function. A potential of +4.2 kV is used to extract electrons from the tip before they are accelerated by the second anode. For biological applications an acceleration voltage between 120 kV and 300 kV is typically used.

Lenses and apertures

Lenses in an electron microscope are electromagnetic, so while their position is fixed, their focal length is adjustable. Two (e.g. FEI Tecnai Polara G2) to three (FEI Titan Krios) condensor lenses and corresponding apertures are used to shape the beam to evenly illuminate the sample. The sample is located almost within the objective lens which collects the scattered electrons. The objective aperture filters out electrons scattered to higher angles and enhances the contrast. Diffraction and projection lenses further magnify the image and either project in on a phosphor screen or on the camera. They are also required to view the diffraction pattern of the specimen.

Energy filter

As described below (chapter 3.2), elastically scattered electrons convey useful information in cryo-electron tomography. An energy filter can be employed to only allow electrons within a certain energy range to pass towards the detector. This filter can either be located within the column of the microscope (Ω-filter) or below the column ('post-column filter'). A post-column filter further magnifies the image, an effect that can be compensated by reduced magnification within the column.

Detection systems

Originally photographic film was used to record images in the electron microscope, a practice that is still relevant today. While electronic cameras allow for automatic image recording and speed up the data acquisition process substantially, film was long considered the gold standard for single particle acquisition because of the superior field of view and the good transfer of high spacial frequencies. The latter is often described by the modulation transfer function (MTF).

Charge coupled device (CCD) cameras are the most common detectors used in electron microscopy. Most importantly, electronic readout allows for automated imaging adjustments between acquisitions. It removes the necessity of manual change of the photographic plates and allows the computer to adjust the microscope between acquisitions, greatly facilitating electron tomography and the acquisition of large datasets in single particle analysis. CCD chips are only capable of detecting photons, therefore a scintillator has to be used to initially convert the incident electrons into photons that are subsequently detected by the CCD chip and converted back into an electronic signal. The angular distribution of the photons, the physical thickness of the scintillator and the fact that one electron can produce an avalanche of photons induce a spread of the signal.

Direct detectors were developed to circumvent the aforementioned limitations of CCD detectors. They are based on CMOS chips are able to detect electrons directly, without the use of a scintillator. This allows for a much lower physical pixel size on the chip and much better MTF [2]. An additional advantage over CCD chips is the fast readout speed of up to 400 frames per second. An image can now be recorded as single frames that are later aligned, eliminating the drift of the specimen during acquisition.

3.2 The interaction of the specimen with the electron beam

This chapter will discuss the two ways in which electrons interact with the specimen: Elastic and inelastic scattering. During elastic scattering events, the kinetic energy is preserved. The interaction between incident electrons and the nucleus of the atoms in the specimen is of elastic nature, while the interaction with the electron shell results in inelastic scattering.

3.2.1 Elastic scattering

Elastic scattering occurs at the Coulomb potential of the nucleus of the sample. In the Wentzel approximation, the Coulomb potential of the nucleus can be described as[2]:

$$V(r) = -\frac{e^2 Z}{4\pi\epsilon_0 r} \cdot e^{-r/R} \tag{3.1}$$

R is being the screening radius $R = a_H Z^{-1/3}$ with the Bohr radius a_H. It is evident, that the potential is proportional to the atomic number Z.

We can describe incident electron as a plane wave $\Psi_{inc} = \Psi_0 e^{2\pi i k r}$. The observer of a scattering event is far from the event and close to the optical axis, therefore, we can describe the scattered electron in Frauenhofer approximation as:

$$\Psi_{sc}(r) = \Psi_0 a_{sc}(r) \cdot e^{i\varphi_s(r)} \cdot e^{2\pi i k r} = \Psi_{inc} + \Psi_{inc}[e^{i\varphi(r)} - 1] \tag{3.2}$$

$a_{sc}(r)$ is the decrease of amplitude and equal to 1 in case of elastic scattering and $\varphi_s(\vec{r})$ is the phase shift induced by the specimen:

$$\varphi_s(\vec{r}) = \int V(\vec{r}, z) dz \tag{3.3}$$

The first term on the right hand side of eq. 3.2 describes the unscattered wave and the second term yields the amplitude of the scattered wave $f(\theta)$ [78]:

$$f(\theta) = -2i\pi k \int_0^\infty [e^{[i\varphi_s(r)]} - 1] J_0(2\pi q r) r \, dr \tag{3.4}$$

---

[2]Z: atomic number, ϵ_0: vacuum permittivity, e: electron charge, r: radius, R: screening radius

Wherein J_0 is the Bessel function. In biological materials most molecules consist of atoms with low atomic numbers and the induced phase shift is very small. Therefore the 'weak-phase approximation' (Born approximation) $\varphi_s \ll 1$ can be applied and the exponential can be expanded to a Taylor series that can be truncated after the second term:

$$e^{i\varphi_s(\vec{r})} = 1 + i\varphi_s(\vec{r}) + \frac{1}{2}\varphi^2(\vec{r}) + \ldots \qquad (3.5)$$

If we apply the Taylor series expansion to eq. 3.4 and truncate after the second term, the scattering amplitude $f(\theta)$ is a real quantity. Using the Wentzel model (eq. 3.1, 3.3) we obtain [78]:

$$f(\theta) = \frac{\lambda^2(1 + E/E_0)}{8\pi^2 a_H}(Z - f_x)\frac{1}{sin^2(\theta/2)} \qquad (3.6)$$

$$E_0 = m_e c^2 \qquad (3.7)$$

In which $f_x = \frac{Z}{1+4\pi q^2 R^2}$ is the scattering amplitude for X-rays. For small angles $sin(\theta/2) \approx \theta/2$, the differential cross-section $\frac{d\sigma_{el}}{d\Omega} = |f(\theta)|^2$ can be calculated:

$$\frac{d\sigma_{el}}{d\Omega} = \frac{4Z^2 R^4(1 + E/E_0)^2}{a_H^2}\frac{1}{[1 + (\theta/\theta_0)]} \qquad (3.8)$$

With $\theta_0 = \frac{\lambda}{2\pi R}$. The total cross section can be approximated:

$$\sigma_{el} = 2\pi \int \frac{d\sigma_{el}}{d\Omega} sin\theta d\theta \propto \lambda^2 Z^{4/3} \qquad (3.9)$$

For $\theta = \theta_0$ the differential cross section drops to a forth of the value for $\theta = 0$.

3.2.2 Inelastic Scattering

Inelastic interactions comprise phonon excitation (20 meV - 1 eV), intra- and interband excitations of outer electrons and plasmon excitation (3 eV - 25 eV) and ionization of core electrons (>100 eV). This complicates the calculation of the cross section for inelastic scattering, but an experimental value of $\frac{\sigma_{inel}}{\sigma_{el}} \approx \frac{20}{Z}$ indicates that for low atomic numbers, inelastic scattering dominates [78]. In biological

samples, the mean free path of electrons for inelastic scattering events therefore much shorter than for elastic scattering (180 nm and 450 nm respectively [84].

Inelastic scattering can provide insight into the elemental composition and is exploited in methods such as electron energy loss spectroscopy (EELS) and electron spectroscopic imaging (ESI). In cryo-electron microscopy, it is desirable to filter out inelastically scattered electrons because inelastic scattering events are less localized (e.g. plasmon interactions) and thus do not provide high frequency information. Furthermore, the lower mean free path for inelastically scattered electrons means that if an electron has undergone multiple scattering events, at least one of them was with high probability inelastic. Notably, the characteristic angle is much lower compared to to the characteristic angle for elastic scattering events. Therefore, inelastically scattered electrons are scattered at much lower angles and are not effectively blocked out by the objective aperture [78].

An energy filter can be employed to selectively remove electrons that do not have the desired kinetic energy. This method is called *zero loss imaging*. As the filter allows a spread of usually 20 eV, phonon interactions cannot be filtered out.

3.3   Image formation in the electron microscope

Two mechanisms play a role in contrast formation in the electron microscope: phase and amplitude contrast. Amplitude contrast is also termed scattering contrast and stems from the removal of scattered electrons at the objective aperture. In biological specimen, scattering contrast is very weak due to the low atomic number of atoms present in proteins and lipids. Staining with heavy metal ions or their salts, such as uranyl acetate, can increase the contrast. The electron beam mainly interacts with the stain. The volume of the particle excludes the stain and stands out brightly from the background. This technique is hence called negative staining. However, the granularity of the salt limits the penetration of the salt into the molecule, for example leading to cavities in the protein not being stained. Uneven staining of the protein surface may further impede the interpretation of the results. Lastly, the resolution that can be achieved is limited to the size of the molecule used for staining and is typically around 20 Å.

Phase contrast

In cryo-EM of biological samples, where molecules consist of atoms with low atomic number, amplitude contrast is not sufficient to successfully image the specimen.

Phase contrast is influenced by the spherical aberration of the objective lens and by defocussing the sample. Phase contrast can therefore be adjusted by the user and dominates contrast formation in biological specimen.

To form phase contrast, the scattered electron has to experience a phaseshift φ. For small phase shifts (small angles and low Z), we can describe the wave as:

$$\Psi_{sc} = \Psi_{inc}e^{i\Phi} \approx \Psi_{inc} \cdot (1 + i\varphi) \tag{3.10}$$

Electrons scattered beyond an angle defined by the objective aperture are filtered out. The objective aperture acts like a bandpass filter in Fourier space:

$$\Theta_{OA}(\vec{k}) = \begin{cases} 1 & \text{if } |\vec{k}| \leq k_{max}; \\ 0 & \text{if } |\vec{k}| \text{ elsewhere.} \end{cases} \tag{3.11}$$

Lens aberration and defocussing play an important role in phase contrast formation. Their contribution can be summarized in the contrast transfer function (CTF):

$$CTF(\vec{k}) = 2sin\left(\frac{\pi}{2}[C_s\lambda^3k^4 - 2\Delta z\lambda k^2]\right) \tag{3.12}$$

Wherein C_s is the spherical aberration of the objective lens and Δz is the defocus value. The CTF acts as an additional phaseshift in the back focal plane of the objective lense and can be mathematically described as a convolution. The resulting electron wave is therefore:

$$\psi_{final}(\vec{k}) = \mathcal{F}^{-1}\left\{\Theta_{OA}(\vec{k})\mathcal{F}\left\{\psi_{sc}\right\} \cdot CTF(\vec{k})\right\} \tag{3.13}$$

The recorded image depends on the intensity $I = |\Psi_{final}|^2$. It can be shown that:

$$\mathcal{F}(I) \propto sin(\frac{\pi}{2}[C_s\lambda^3k^4 - 2\Delta z\lambda k^2]) \tag{3.14}$$

Therefore, not all frequencies are equally well transfered in the final image (see fig. 3.2). To accommodate for this, CTF correction is routinely applied in single particle analysis. In low dose electron tomography the low signal to noise ratio in an individual image impedes defocus determination. To make matters worse, the defocus value is not constant within one image due to the tilted specimen. CTF correction is still possible but not employed widely [26, 104].
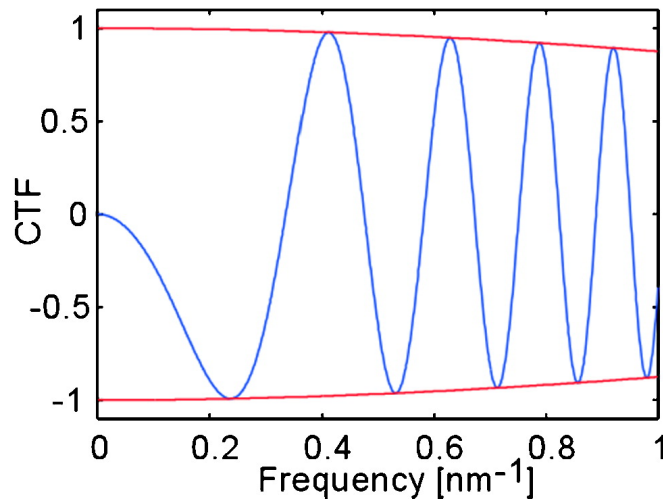
Figure 3.2: CTF (blue) and envelope function (red) for a FEG microscope at 300kV acceleration voltage. From [58]

3.4   Cryo-electron microscopy

Cryo-electron microscopy allows us to directly view many biological specimen without the need of labeling or crystal formation. In addition to two dimensional images, two methods exist to generate a three dimensional view of the specimen. They both are based on the reconstruction of the three dimensional volume based on two dimensional projections, described by Radon in 1917 [77].

If the object of interest is a stable protein or protein complex that can be purified, single particle analysis (SPA) is often the method of choice. SPA makes use of the different views of one molecule that can be recorded in a single image of purified molecules. All views of the molecule are extracted ('picked') and then aligned to a three dimensional model. A temporary model is calculated and the projections are re-aligned iteratively, until a stable solution has been found. SPA projects make use of thousands to millions of projections of a protein. Nowadays the resulting reconstructions of a protein can reach close to atomic resolution and can even detect subtle conformational shifts [95].

Electron tomography (ET) has firstly been used in 1974 [44] and is widely used in cellular tomography, where each specimen is unique. Tomography is also used when averaging multiple protein complexes is not viable, for example when visualizing the protein together with its environment.

In electron tomography, the sample is tilted in the microscope and a projection

image is recorded at defined angular steps. The *dose fractioning theorem* states that the final resolution of the reconstruction is the same as in an individual image that has been exposed to the same electron dose as the sum of the projection images [45]. The Crowther criterion [17] describes the highest obtainable isotropic resolution depending on specimen thickness d and number of projections N:

$$r = \frac{\pi d}{N} \tag{3.15}$$

This is never attained in practical applications because the sample holder and the increased specimen thickness at high angles restrict the tilting range. As a result, a fraction of the Fourier space cannot be sampled and those frequencies are missing in the final reconstruction. This leads to an *missing wedge* effect and an elongation of the sample along the imaging axis. The dependence of the final reconstruction on tilting step and tilting range is illustrated in fig. 3.3.

Even in the specimen plane the resolution is not uniform. Along the tilt axis it only depends on the microscope and camera, as well as the number of images, while the resolution perpendicular to it depends on the tilting range and step (see fig. 3.3).

Both effects can be mitigated by acquiring two separate tilt series in between which the specimen is rotated by 90°. The reduced signal along the tiltaxis is compensated by the rotation and the missing frequencies in Fourier space are partly sampled. The missing information along the imaging axis becomes a smaller cone instead of a wedge.

Different algorithms exist to calculate the three dimensional volume from the projection images. A projection of an object of thickness d samples a slice in Fourier space of thickness 1/d. Therefore, when collecting projections at various angles, spacial frequencies are not sampled evenly (see fig. 3.4). Apart from the missing wedge region, the Fourier space up to the spacial frequency $k_C = 1/r$ is completely sampled. As can be seen in figure 3.4, low spacial frequencies are oversampled. The weighted back projection (WBP) algorithm takes this into account and weights the frequencies accordingly. As the amount of oversampling depends on the specimen thickness, and it thus has to be known to calculate an exact solution. A common alternative reconstruction algorithm is the simultaneous iterative reconstructive technique (SIRT). Here, an estimated reconstruction is generated. Afterwards the projections of the initial reconstruction are calculated *in silico* (forward projection) and compared to the recorded projections. The differences between the two sets of projections are then used to correct the estimated volume. This process is repeated iteratively until the solution converges.
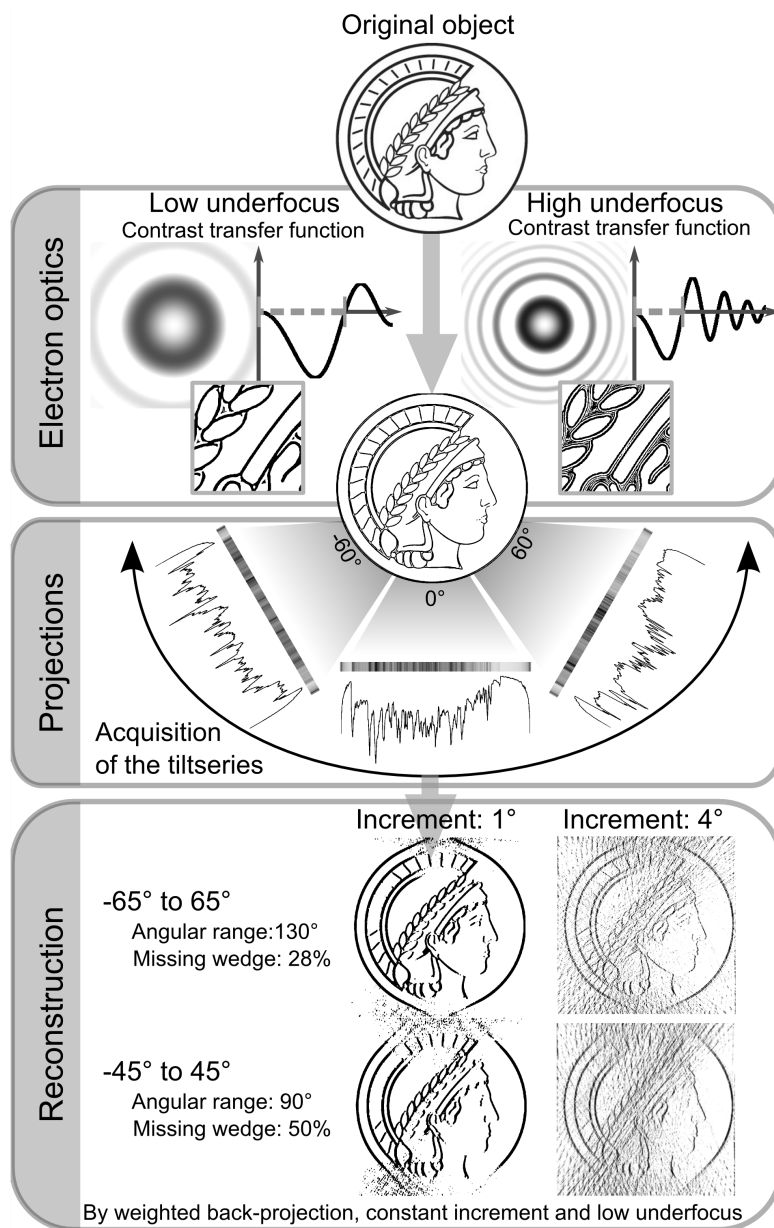
Figure 3.3: Electron tomography scheme. Top: Influence of the CTF on a 2d image. Middle: Projections are depicted both as a one dimensional image and line graph. Bottom: Influence of the overall tilting range and increment on the reconstruction.
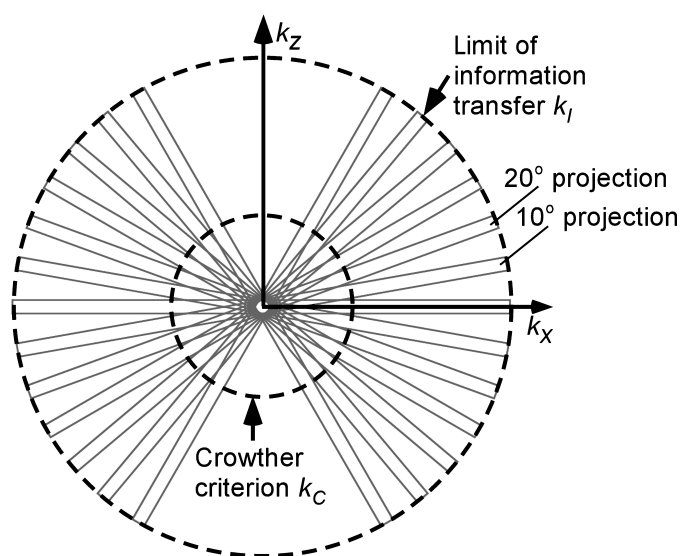
Figure 3.4: Data sampling in Fourier space. The object is sampled at discreet angles. Each projection of an object of size d samples a slice of thickness 1/d in Fourier space. From [58].

Chapter 4

Correlative Microscopy

Light microscopy has greatly advanced our understanding in biology. Immunostaining can be used to identify proteins or lipids and advanced methods like superresolution microscopy allow an even more precise localization of the protein. Even the relative distance of protein domains can be studied with fluorescence energy transfer (FRET) microsopy. While all of these techniques provide important pieces to the puzzle, staining techniques always show the label and not the stained target itself. Electron microscopy on the other hand can provide a detailed view of the specimen's structure but lacks the functional information that light microscopy can provide. In addition, electron microscopy does not only show a stained target protein or lipid but provides an open view in the target cell. This can be a double edged sword because it can give new insights into the arrangement or interaction between the target and its environment but it also can impede the proper identification of the target.

Correlative light- and electron microscopy (CLEM) aims to combine the advantages of the two techniques. It has been widely used in medicine where immunostaining and conventional electron microsopy are often used in sync, as well in diagnosis as in research. In life sciences, common applications of CLEM are for example the identification of cells affected by a drug or treatment or the localization of an object of interest within a large cell.

Slow processes and fixed cells can often be stained and imaged before immobilization by vitrification or conventional means. Fast processes and cells in solution need to be fixed before imaging in the light microscope. While this is generally unproblematic for chemically fixed samples, imaging after vitrification requires the specimen to be kept below -150°C.

There are currently two approaches to keep the specimen vitrified during light

microscopy (LM). In an integrated approach the light microscope is inserted into the column of the electron microscope [24]. While requiring substantial changes to the electron microscope, this approach allows the user to quickly switch between light and electron microscopy by rotating the grid by 90°.

A modular approach uses a light microscope in combination with an special specimen holder that is cooled to cryo-temperatures in order to preserve the vitrification of the specimen. The user is not restricted to one electron microscope. Additionally, changes to the light microscope do not require the column of the electron microscope to be opened. On the flipside, the additional transfer step can lead to deformation or even loss of the sample.

4.1 Correlative approach

This study made use of the Cryostage[2] setup on a Zeiss Axiovert M200 microscope [79]. The correlation method is described in more detail in section 8.5 in the Materials and methods chapter. Briefly, landmarks that can be identified in both light and electron microscopy images were selected and exported from ImageJ. After that a python script written by Vladan Lucic was used to establish a two step correlation: First between the LM images and a low-magnification electron microscopy (EM) image (EM-overview image), then between the EM-overview image and physical stage coordinates. It is possible to calculate both the physical coordinates in the electron microscope from the position of features of interest in the LM image and the other way round.

In order to test the precision of the calculation, we used fluorescent beads with 1 µm diameter on a standard EM grid. The fluorescent beads can easily be identified in LM and EM images and provide a means to directly verify the precision of the correlation. The calculated error was 0.7 µm for the LM to EM overview correlation. For the correlation of the EM overview image to EM coordinates we calculated an error of 0.3 µm and 0.6 µm for the two implemented modes respectively (see method section 8.5 and corresponding figure 8.2 for details). We used the established correlation to calculate the coordinates of the fluorescent beads and found the true error of the correlation from LM images to EM coordinates to be below 0.4 µm.

In real data applications, the calculated error of LM to EM-overview correlation ranges from 0.5 to 1.9 micrometer, mostly depending on the quality and precision of the landmarks used to establish the correlation. The position of holes in the carbon and cracks in the ice or carbon - if well preserved - can be determined with

higher precision than for example the corners of the gridbars. The pixel size of the LM images also plays a major role. Results achieved using a 63x objective (NA 0.75) in the light microscope were slightly better compared to a 20x objective (NA 0.4).

The error of EM-overview to EM-search correlation was usually between 0.6 and 1.1 micrometer, although larger errors have been observed. The imperfect precision of the stage likely plays a significant role. We tested the stage precision by arbitrarily moving the stage in x and y directions and measuring the displacement from the initial stage position when the stage was set to return to the starting coordinates. For movements between 10 and 100 µm, corresponding to the movement within one gridsquare, we found a stage error of 370 ± 184 nm and 336 ± 209 nm in x and y direction respectively (mean $\pm$ std, N = 10). For larger movements (200 - 500 µm) the error increases substantially to 299 ± 135 nm and 1021 ± 392 nm in x and y direction respectively. In addition, the gold grids used in cell culture are easily deformed. A support ring (Autogrid, FEI, The Netherlands) can be used to stabilize the grid. It is possible to use the support ring before cryo-fixation of the grid, but the liquid retained by the ring can obstruct large areas of the grid from direct access by EM or even impede the proper vitrification during plunge-feezing.

Fluorescent probes are routinely used to identify proteins. We therefore compared fluorescent intensities at room temperature and under cryo-conditions. For Hela cells transiently expressing a GFP construct, we found a ratio of 0.41 ± 0.37 (mean $\pm$ std, $N = 10$, p<0.05 by paired t-test) and for an mCherry construct 0.53 ± 0.23 (mean $\pm$ std, $N = 15$, p<0.001 by paired t-test). Both dyes performed better under cryo conditions than at room temperature. During low dose cryo-electron tomography (cryo-ET) the specimen is typically exposed to a cumulative electron dose of ~100 electrons per square Ångström. We illuminated a Hela cell expressing a transient GFP construct in the electron microscope with an equivalent dose at low magnification and compared the fluorescence intensities before and after illumination. Fluorescence was reduced by 27% compared to cells not illuminated in the electron microscope.

4.2 Targeting Eph/Ephrin interaction in large cells

This work was performed together with Dimitri Vanhecke[1] in collaboration with Maria Sakkou[2] and Rüdiger Klein[2]

The development of the mammalian brain is a lengthy process with multiple stages. In the initial phase, neurons have to travel to their designated brain areas and form connections to the correct neurons. Both of these processes are regulated by a myriad of proteins.

Among those are Ephrins and their respective Eph receptors (reviewed in [73]). Eph-receptors belong to the receptor tyrosine kinase (RTK) family. While most RTK interact with soluble ligangs, Ephrins are membrane bound extracellular proteins and can be classified into Ephrin A and Ephrin B families. Members of the Ephrin A family comprise a transmembrane domain, while Ephrin B proteins are connected to the membrane via a GPI linker. Ephrin A ligands preferably bind to Eph-A receptors and Ephrin B ligands respectively to Eph-B receptors. However, exceptions to the rule do exist.

Upon contact with Ephrins, Eph receptors can activate a variety of cellular pathways. Apart from this forward signaling, Eph-Ephrin interaction allows reverse signaling which is less understood [103]. The interaction of Ephrins with their respective receptors usually invokes a repulsive response between the cells but an attractive interaction does happen in some cases. For example, low levels of Ephrin can promote attraction while higher levels promote repulsion [65]. Interstingly, even initial attraction changing into repulsion in a time-dependend manner has been observed [64].

After Hela cells transiently expressing fluorescently labeled Ephrin have come into contact with Hela cells expressing a fluorscently labeled Eph-receptor and undergo a repulsive reaction, the Eph/Ephrin complex does not dissociate but is endocytosed as a whole in both cells. As this process has never been directly visualized, we attempted to use cryo-CLEM to capture and identify Eph/Ephrin endocytosis events.

---

[1]at that time MPI for Biochemistry, Martinsried, Germany; currently at Adolphe Merkle Institute, Fribourg, Switzerland

[2]MPI for Neurobiology, Martinsried, Germany

Eph-Ephrin interaction causes fragmentation of the cell membrane

Two experimental setups were used in this study: The first was a cell-cell assay with the two cell populations transiently expressing the Ephrin-B1 protein and the Ephrin receptor Ehp-B2 respectively. The Ephrin-B2 receptor construct we used lacked the C terminus (Eph-B2-ΔC) and cannot be endocytosed by the host cell. In the second assay cells expressing Ephrin-B1 were exposed to preclustered soluble Eph-B2 receptors.

In both cases the Ephrin-B1 expressing cells were grown on poly-L-lysine coated gold grids and the Eph-B2-ΔC containing cells or the preclustered Eph-B2 were added to the grids. After 10 minutes, cells were washed and the grids were directly plunge frozen. The cells added in the cell-cell assay often detached during plunging, facilitating the access to the Ephrin-B1 expressing cells.

Even with extensive blotting, Hela cells often were not directly accessible by cryo-EM. Cos7 cells are overall thinner compared to Hela cells and have a more favorable cell profile. After initial attempts with Hela cells all further experiments were performed with Cos7 cells. This allowed us to directly target the cell edge on the grid without use of thinning steps. As far as we could tell from light microscopic data and our limited EM data with Hela cells, there were no apparent differences between Hela and Cos7 cells in our assays.

Cos7 cells showed a heavy fragmentation of the cell membrane after Eph-Ephrin contact (see fig. 4.1), independent of the assay. In control cells expressing Ephrin without being exposed to Eph receptors, we find a low amount of membrane fragmentation, likely occurring from auto-clustering of the Ephrin. The fragmentation is much more pronounced after contact with Eph-B2 receptors and correlates with the sites of Eph-Ephrin co-fluorescence. Surprisingly, we find many large vesicles of 25 - 500 nm diameter with multiple membraneous layers. We expected to see differences between the cell-cell assay and the non-membrane bound Eph-B2 but found similar vesicles in both cases.

Events inside cells were much harder to target and we only could obtain a few images. Most fluorescent spots either corresponded to regions with high cell membrane fragmentation or were located too far off the cell edge to be accessible by cryo-ET.

We next tried to target fluorescent signals outside of cells. Although rarely, we found fluorescent signals outside of cells. In addition, we found vesicles with a double membrane, even in assays with soluble cells (see fig. 4.2).
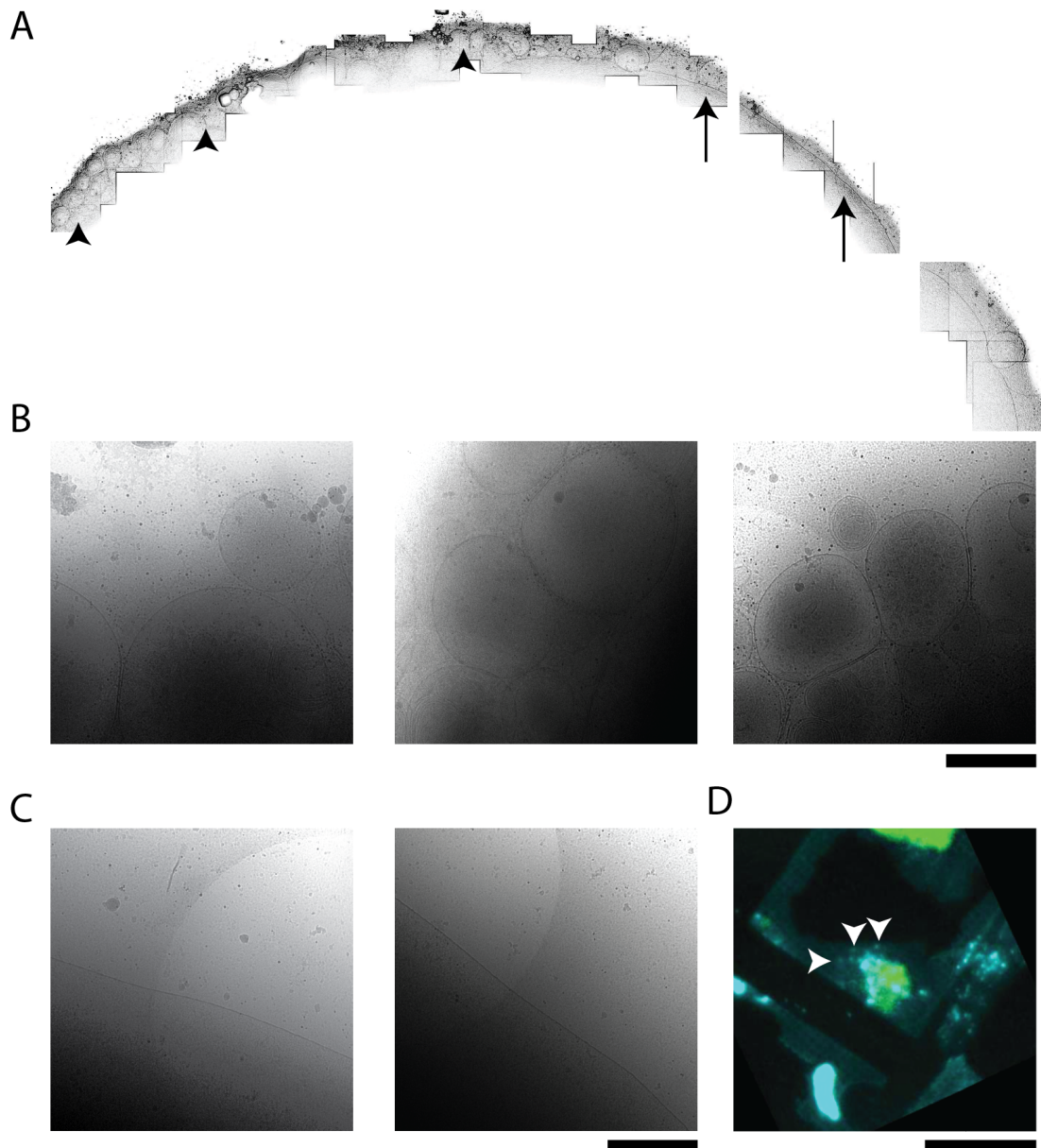
Figure 4.1: Edge of a Cos7 cell in EM after a cell-cell assay. **A**: Stiched images of a Cos7 cell. Locations corresponding to Fluorescent spots are marked with arrowheads. **B**: Electron micrographs of locations marked by arrowheads in (A). The cell membrane is heavily fragmented into vesicular structures. Scalebar 500 nm. **C**: Areas devoid of fluorescent spots show a smooth surface. Electron micrographs correspond to locations marked by arrows in (A). Scalbar 500 nm. **D**: Cryo-fluorescence of the grid square the cell in (A) is located in. Cyan: Ephrin-B1, green: Eph-B2-ΔC. Arrowheads mark the same locations as in (A). Scalebar: 50 µm.

Overall, we could show that Ephrin-B1 and Eph-B2 interaction causes the cell membrane to form vesicles of various sizes and frequently with multiple membranes. At least a fraction of them must contain Eph-Ephrin complexes as supported by our CLEM data. It is known that most Eph-Ephrin complexes are endocytosed and transported towards the center of the cell and it has been suggested that double vesicles are formed during the endocytosis process. However, we could not visualize these structures within the cell due to specimen thickness. The structures found outside of cells do partly resemble the suggested structures within the cell, however the fact that they often comprise more than two membranes and are also found in assays where one cell was exposed to soluble Eph-B2 instead of a second cell expressing the protein opens up the possibility that it may be an artifact of the assay stemming from Ephrin overexpression.
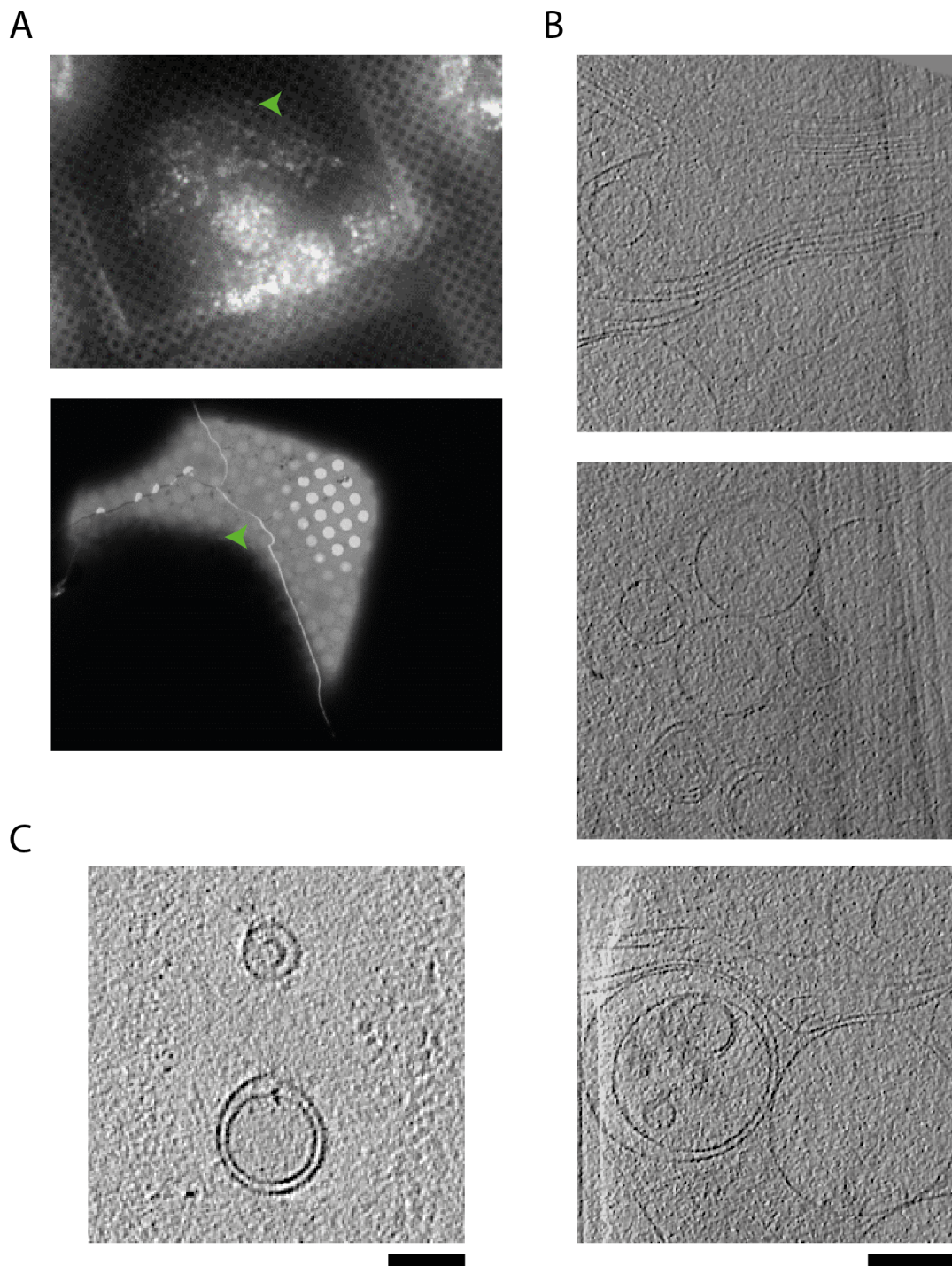
Figure 4.2: CLEM of the Eph-Ephrin complex. **A**: Light and electron microscopy image of Ephrin-B1 expressing Cos7 cell after contact with an Eph-B2-ΔC expressing cell. **B**: Slices from the tomogram taken at the position marked in (A) with an green arrowhead. Scalebar 200 µm. **C**: Example of an external vesicle with double membrane found near a fluorescent spot after the cell was in contact with soluble Eph-B2. Scalebar 100 µm.

4.3 Locating presynaptic terminals in cultured neurons

Neurons form a very dense mesh of neuronal processes on the grid. In order to locate structures of interest, for example mature or orphan synapses, one needs to scan wide areas of the grid, often switching between magnifications to get a clear view of the process. We employed correlative light- and electron microscopy (CLEM) to narrow down the location of such structures in advance. As neurites are often dynamic and boutons can move along the axon we chose to perform imaging in the light microscope after vitrification of the specimen.

FM dyes can be used to visualize synaptic endo- and exocytosis in neurons [34] and can be used to label synapses and orphan synapses, presynaptic boutons that are also capable of synaptic vesicle release [54]. FM dyes are styryl dyes that comprise a lipophilic tail group, an aromatic bridge region that creates the fluorophore and a charged head group. The dye binds lipid bilayer but cannot cross the membrane due to the charged head group. When cultured neurons are stimulated while the dye is present in the buffer it is internalized during synaptic vesicle recycling. The dye remaining outside the cells is easily washed away and sites of endocytosis can readily be identified. We applied a stimulation and staining protocol to facilitate synapse detection in the EM. An example of neurons stained with FM dye and imaged under cryo-conditions can is depicted in fig. 4.3, A.

After staining, neurons showed a punctuated fluorescent signal in cryo-LM. Costaining with more specific synaptic markers showed that only a subpopulation of the varicosities labeled by FM dyes were costained.

A precision of $\sim 1.5 - 2\mu m$ was often sufficient to locate presynaptic boutons as they can be identified visually once the area has been narrowed down. However, the density of neuronal processes does not allow us to correlate a fluorescent spot unambiguously to a single process. An example of a correlation can be found in fig. 4.3. Neurons at days *in vitro* (DIV) 9 were stained with FM1-43 and imaged under cryo-conditions after vitrification (fig 4.3, A). For grid squares that had both fluorescent signal as well as sufficiently thin, vitreous ice a correlation was established. Fluorescent spots of interest that were targeted in the electron microscope are marked with green dots in the LM (B) and corresponding low magnification EM image (C). The location of tomograms taken on this grid square is marked by red dots in (C). White arrowheads point out tomograms that where acquired at positions correlating with fluorescent spots.

Synaptotagmin is a membrane protein present in synaptic vesicles. If the synaptic vesicle fuses with the postsynaptic membrane, the luminal domain is exposed to

the extracellular medium and can be targeted with an antibody [100]. An antibody against the luminal domain of synaptotagmin-1 coupled to Oyster blue was used to label varicosities that undergo synaptic vesicle recycling. Only a fraction of varicosities labeled with a FM dye was also labeled positive by the antibody (fig. 4.4, B). Oyster blue puncta were less bright than FM1-43 puncta but showed almost no background fluorescence. There may be several reasons for the lower amount of Oyster blue staining: The antibody may not stain as efficiently as the FM dye. The interaction surface of the luminal side of the synaptic vesicle membrane is much larger than the binding region of the antibody to the exposed luminal domain of synaptotagmin, making it more likely that a vesicle is stained by FM dye than by synaptotagmin antibody staining. Another possibility is that vesicles in at least a fraction of the presynaptic boutons undergoing synaptic vesicle exocytosis and recycling may be immature and may still lack proteins present in mature synaptic vesicles.

In order to assess the possibility of having a dye visible in both the light and the electron microscope, a secondary antibody coupled to the quantum dot QD605 was used to specifically target the synaptotagmin antibody. Unfortunately, QD605 puncta were even less bright than Oyster blue puncta, most likely due to the fact that most of the synaptotagmin antibody was already internalized and the secondary antibody could not bind to it. Cryo-EM of the antibody did not show sufficient contrast for detection of the quantum dot in low dose electron microscopy images. While in thin specimen quantum dots may be used for protein identification or even to align a tiltseries, this was not possible in our case, where we wanted to directly observe neuronal processes, presynaptic terminals and synapses. Under low dose imaging conditions the signal to noise ratio was not sufficient to We therefore did not further pursue the use of quantum dots for labeling.

Bassoon is transported along axons in developing neurons and recruited to nascent synapses [85]. In order to locate these transport packages, cells were transfected with a Bsn-GFP construct on DIV 7 using Lipofectamine transfection [18]. Successfully transfected cells showed distinct puncta after 4 days of incubation (fig. 4.4, C). Background fluorescence was significantly lower compared to FM dyes (fig. 4.4, A) [21]. On average, only 3 cells per grid showed sufficient GFP expression. Many of those cells were located on top or directly next to grid bars, impeding or preventing potential tomogram acquisition. Considering the many steps necessary until the cells can be imaged in the electron microscope and the requirement of thin, vitreous ice surrounding the cell, Lipofectamine transfection rate was not sufficient for correlative microscopy.
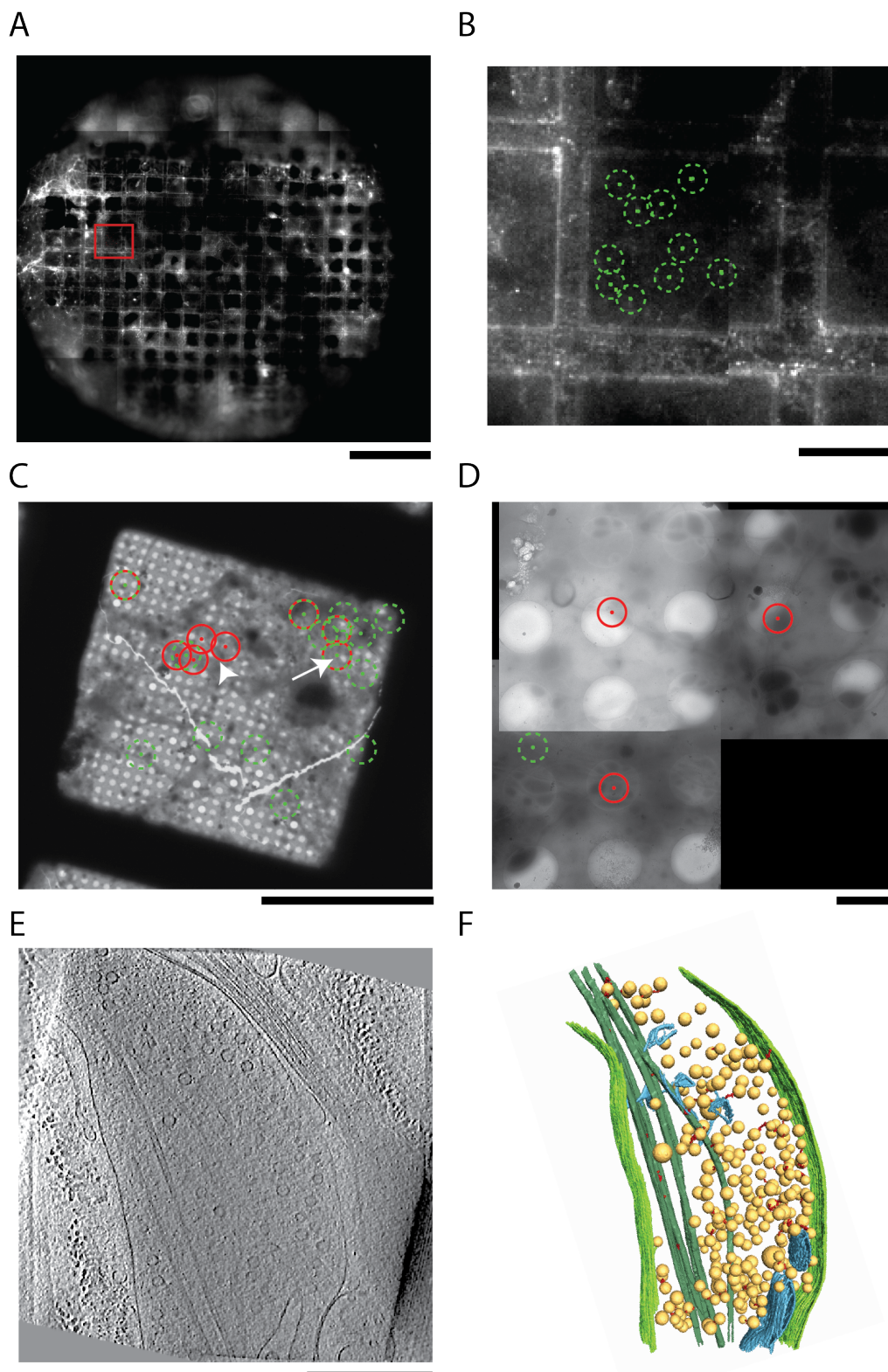
Figure 4.3: CLEM of hippocampal neurons. **A**: Scan of the entire grid in cryo-LM. Scalebar 500 µm. **B**: Blowup of the area marked in red in A. Green dots with dotted circles mark selected fluorescent spots. Scalebar 50 µm. **C**: EM image at 175x magnification. Red dots with circles mark location of tomograms taken, green markings correspond to spots from B. Green dots with red/green circle mark spots where tomogram and fluorescent signal colocalize well. Scalebar 50 µm. **D** Area of adjacent to the arrowhead in C. Scalebar 5 µm. **E,F** Slice through tomogram taken at the location marked by white arrow in C, and corresponding segmentation. Scalebar 5 µm.
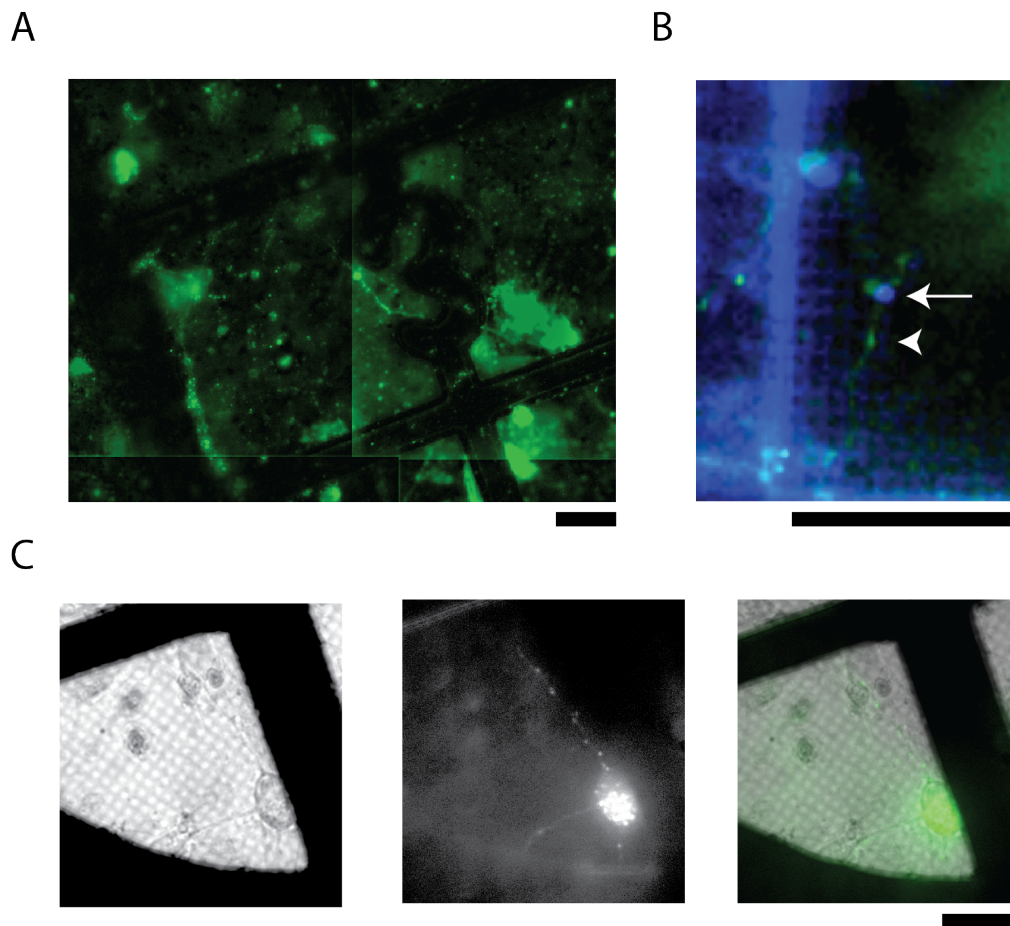
Figure 4.4: Fluroescent staining of cultured neurons. **A**: Fluorescent image of neurons stained with FM1-43 dye. **B**: Neurons stained with FM1-43 and in parallel with a primary antibody against synaptotagmin covalently coupled to Oyster blue. **C**: Neuron transfected with Bassoon-GFP construct. Phase contrast (left), fluorescence (middle) and composite image (right). All Scalebars 25 µm.

Chapter 5

Presynaptic boutons and axonal transport in neuronal cultures

Neurons form the core of the central and periphal nervous system. They are electrically excitable and able to pass this excitation to other neurons or to muscle cells. This transfer of information happens at contacts termed synapses. Synapses can be of electrical or chemical nature. At electrical synapses, the plasma membrane of the two cells is in direct contact with each other and are connected via gap junctions, allowing charged ions to pass. Electrical synapses are symmetric and provide a direct link between neighboring neurons. They are thought to serve the synchronization of neurons [43], but their role in the central nervous system is still poorly understood [57]. Chemical synapses play the arguably more important role in our nervous system. At a chemical synapse the presynaptic cell is attached to the postsynaptic cell via an array of proteins, forming a synaptic cleft of a defined distance. Upon stimulation, vesicles containing neurotransmitter fuse with the plasma membrane in a region termed the active zone (AZ). The released neurotransmitter diffuse through the synaptic cleft to the postsynaptic cell where they cause ion channels to open, allowing the influx of ions and depolarization of the cell. Chemical synapses can be of excitatory or inhibitory nature. They are capable of synaptic plasticity, changing the strength of the synaptic transmission either in the short- or long-term in response to the activity of the synapse itself (homosynaptic plasticity) or the activity of other synapses (heterosynaptic plasticity). Strengthening of the transmission is termed potentiation and weakening is called depression. Long-term potentiation (LTP) and long-term depression (LTD) are, among with the formation of new synapses and the loss of existing ones, thought to form the basis of learning.

5.1 Synaptogenesis

The formation of synapses is termed synaptogenesis. As one of the most fundamental processes during development and learning, it has been extensively studied by by immunochemistry and genetic mutations [16, 99] as well as by conventional electron microscopy [98] . While many molecules have been identified and mechanisms have been revealed, a lot of open questions remain [35].

The development of the mammalian brain is a lengthy process with multiple stages. In the initial phase, neurons have to travel to their designated brain areas and form connections to the correct neurons [12]. Both of these processes are regulated by a myriad of proteins.

While Ephrins (introduced in chapter 4.2) can induce both cell adhesion or repulsion, neuroligins, neurexins and SynCAMs on the other hand induce cell adhesion. SynCAM 1 is also known as Cadm1 (cell adhesion molecule 1) or nectin-like molecule 2. Four proteins belong to the SynCAM family. SynCAM 1-4 are lg superfamily members and consist of a single transmembrane domain and three extracellular Ig like domains [31]. SynCAMs 1, 2 and 3 can form homomultimers, but SynCAM 1 binds preferentially to SynCAM 2, as well as SynCAM 3 to SynCAM 4 [32]. SynCAM 1 promotes the formation of excitatory synapses, is involved in synapse regulation and learning [81], and regulates neuronal growth cones [90]. In non-neuronal cells, transiently coexpressed SynCAM 1 and glutamate receptors are sufficient to reconstitute glutamatergic synaptic transmission [7].

Presynaptic differentiation most likely starts prior to postsynaptic differentiation, however, immunolabeling experiments suggest that stationary packages of postsynaptic proteins can form postsynaptic 'hotspots' that can readily recruit the presynaptic machinery upon contact with an axon [37]. In a next step, various synaptic proteins and synaptic vesicles are recruited to the contact site. Immature synapses are functional but still sensitive to perturbations of the cytoskeleton. The synapse now matures within hours to days until it has reached its final protein composition and morphology.

Chemical synapses are often formed on specialized protrusions of the dendrite, so called dendritic spines. These can adopt a variety of morphologies and are most commonly categorized as thin (long neck with small head), mushroom shaped (thin neck with large head) or stubby (short neck with no discernible head). The dendritic spine functions as a compartmentalization of the dendrite, limiting for example the influx of Ca^{2+} to an individual spine [83]. Dendritic spines have been implicated in learning [82] and develop their final form during the maturation of the synapse.

Ahmari et al. [1] and colleagues proposed that proteins required for synaptogenesis were not transported individually, but in discrete packages. Later, it was found that Piccolo was transported along with Bassoon and various proteins associated with the presynaptic active zone [85, 106]. Among these proteins are syntaxin, Munc13, Rim and calcium channel α-domain. None of the proteins found are associated with synaptic vesicles. Immunostaining EM studies revealed that Piccolo is transported with vesicles with a diameter of 80 nm and a dark, granular lumen [106]. Further experiments indicate that active zones consist of a unitary amount of these vesicles and that they can be incorporated in nascent synapses forming *en passent* [85].

Bassoon is another protein of the presynaptic cytomatrix involved in synaptogenesis [105]. Using a GFP-tagged Basson mutant (GFP-Bsn), Dresbach et al. could show that Bassoon strongly colocalizes with Piccolo and the 80 nm dense core vesicles and that they originate from a trans-golgi compartment [21]. These vesicles were hence termed Piccolo/Bassoon transport vesicles (PTVs). Bassoon binds to Dynein light chains DLC1 and DLC2 as well as to Myosin V [25]. Furthermore, if the DLC binding sites in Bassoon are mutated, PTV transport is impaired, indicating that Bassoon is involved in linking the PTV and Dynein. On the other hand, Syntabulin is known to bind to Kinesin I and syntaxin [91]. If Syntubulin is knocked down, Syntaxin motility in axons is impaired [91], implicating a role of Kinesin I in the transport of PTVs. By which mechanism and molecules the transport vesicles are eventually recruited to a nascent synapse still remains unclear.

5.2   Axonal varicosities

Neurons are known to form thickenings along their axons *in vivo* as well as *in vitro* [51]. These thickenings are referred to as varicosities. Their frequency depends on the axon type. In hippocampal neurons from the CA3-CA1 region, a frequency of 3.7 ± 0.7 µm has been observed [87]. Studies utilizing conventional electron microscopy have revealed varicosities filled with organelles as well as seemingly empty ones [86]. The content of axons and varicosities has been described in conventional electron microscopy studies, but few have made an attempt at a thorough classification. One such effort is being made by Kirstin Harris' lab, who set out to create an atlas of the three dimensional ultrastructure of the brain on their internet platform 'SynapseWeb' (http://synapses.clm.utexas.edu/). They have adopted a classification based on the early studies by Bodian in 1970 [8] in order to classify axonal boutons according to vesicular content.

Many axonal varicosities contain synaptic vesicles. The number of synaptic vesicles is highly variable, as is their distribution within the bouton. A fraction of boutons is capable of induced vesicle release and re-uptake despite lacking a postsynaptic partner: In culture dissociated hippocampal neurons stained for the presynaptic proteins Bassoon and VAMP2 at 14 - 21 DIV (days *in vitro*), over a third of both the Bassoon and VAMP clusters are found away from dendritic contact sites. Among those, 67% of Bassoon and 63% of VAMP2 clusters co-localize with puncta of FM1-43 staining, indicating endocytosis after induced synaptic vesicle exocytosis [54]. The requirement of extracellular calcium suggest a similar molecular machinery as in mature synapses [63]. These boutons are often termed orphan synapses and it has been suggested that they display an alternative method of synaptogenesis. If and how this is related to the previously described PTVs is not known. Fluorescent microscopy observations of orphan synapses developing next to and fusing with synapses which possess a opposing PSD indicate that this form of synaptogenesis or synapse modification might play a role later in development [54].

5.3 Primary cultures of hippocampal neurons

Neurons of E19 and P0 rats were cultivated in low density ($5-20\cdot10^4$ cells/35mm dish) and observed in the light and electron microscope after 9 to 15 days in vitro (DIV). To assess the viability of our neuronal cultures, we used immunofluorescence staining against the presynaptic protein synapsin and the postsynaptic PSD-95 (see fig. 5.1). By DIV 9 neurons show a dense network of neuronal processes and start forming first synapses in low density cultures. Synapse density is lower compared to the literature [38], but due to our approach by direct CLEM without thinning steps we are planting neurons with a 10 fold lower density. Although synaptogenesis strongly increases after two weeks in culture [38], our neurons were grown at maximum two weeks in culture, again due to specimen thickness considerations.

Cryo-fixation circumvents many artifacts present in chemically fixed and resin embedded specimen [22] and preserves the structure or organelles and proteins. Two cryo-fixation techniques are routinely applied to neurons: plunge freezing and high pressure freezing (HPF). While the latter allows vitrification of thicker specimen and was used to vitrify brain sections, it requires further thinning steps to make the section accessible by cryo-TEM, such as cryo-sectioning or cryo-milling. Cryosectioning is prone to damage the specimen and even if perfectly executed distorts the sample through the force of the diamond knife used for cutting. Focused ion-
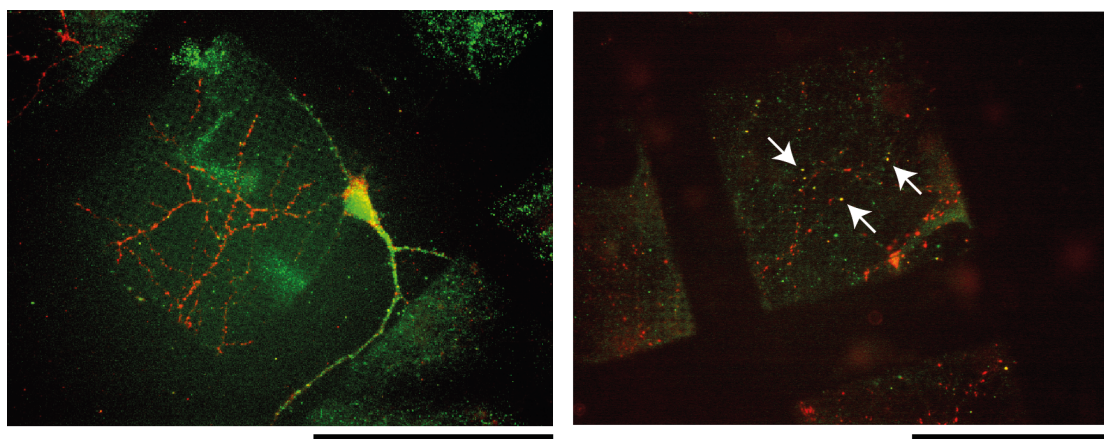
Figure 5.1: Immunofluorescence of neurons grown in low density cultures stained at DIV 9 (left) and DIV 14 (right). Green: postsynaptic PSD95, red: presynaptic synapsin. Scalebars $100\mu m$

beam milling (FIB milling) has been developed recently and allows the sample to be thinned while preserving the ultrastructure. However, further optimization is required to make it suitable for routine work with neuronal cultures. Direct plunge freezing is only possible for thin specimen, as the cooling rate is not sufficient in thick specimen to avoid the formation of ice crystals that damage the specimen and can even prevent imaging in TEM.

Therefore specimen thickness is not only important in order to be able to observe the specimen without further thinning but also for proper vitrification. While cryo-light microscopic imaging can already give us an impression of the ice thickness and may reveal contamination on the grid, vitrification has to be assessed in the electron microscope. Improper vitrification often leads to broken or distorted membranes and can be seen in the ice by creating 'shadows' or reflections. We therefore paid close attention to ensure data was only acquired from neurons with smooth membranes and organelles.

An important aspect of neuronal cultures is that the neurons can be manipulated by a variety of treatments. We mainly used FM staining to target presynaptic boutons or synapses but also applied synaptotagmin staining and overexpression of a protein labeled with a fluorescent dye. Examples are presented in chapter 4.3 and methods section 8.5. After staining with a fluorescent dye, cells were imaged in the light and electron microscope. For the work presented in this chapter, light microscopy was typically performed after vitrification to preserve the state between light and electron microscopy as well as possible.

5.4 Morphological properties of varicosities

Neurons plated in low density on a Quantifoil coated EM grid quickly grow neuronal processes. At DIV 9, these have grown in a dense mesh of overlapping processes. While soma of the cell and the surrounding region are too thick for direct cryo-TEM observation, distal neuronal processes are thin enough to be accessible. They frequently form varicosities or boutons of different sizes and shapes (see fig. 5.2). On a holey carbon film they are formed both in holes and on the carbon support film. A variety of cellular organelles can be found in boutons including mitochondria, smooth endoplasmic reticulum (sER), multi-vesicular body (MVB), lysosomes, dense core vesicles (DCVs), synaptic vesicles (SVs), and a plethora of membraneous compartments of different size and shape.

Tomograms were screened for varicosities and those were categorized by size, shape and content. For further analysis we only selected varicosities that satisfied technical standards (signal to noise ratio, good vitrification, alignment and reconstruction) and contained significant biological material. The latter could be either a larger number of synaptic vesicles or a combination of different organelles. If no large amount of SVs was present, the varicosity had to have at least 3 of the following: Smooth endoplasmic reticulum, mitochondria, clear vesicles, dense core vesicles, multivesicular bodies or other membraneous compartments. Dendrites were identified by the presence of ribosomes and excluded from the analysis. We cannot completely exclude the possibility of dendritic processes in our dataset but the presence of synaptic vesicles and lack or ribosomes are a strong indicator for processes being of axonal nature. After excluding processes of dendritic or unsure nature our analysis comprised 76 axonal boutons out of 124 boutons categorized.

Distinction between big and small varicosities was done manually: Boutons with more than twice the diameter of the axon were classified as big boutons. If the bouton was not fully in the FOV this had to be estimated. Out of the 76 axonal boutons 61 were categorized as big and 15 as small boutons.

Depending on the symmetry of the bouton we characterize big boutons as spindle (28) or sack-like (22) boutons. Spindle type boutons wind around the central microtubules or are symmetrical to it. Sack-like boutons clearly bulge to one side with little volume left on the opposing side of the microtubules. Examples of both categories are depicted in fig. 5.3. Some boutons could not be categorized because they were either not fully in the field of view or they did not fit in either category, e.g. varicosities at bifurcations.

We also utilized a classification from Kirsten Harris' lab[1] to categorize large bou-

---

[1]http://synapses.clm.utexas.edu/anatomy/axon/table.stm, adapted from [8].

| Type	Content	Count
S	spherical synaptic vesicles	19
F	predominantly flat or elongated synaptic vesicles	–
P	pleiomorphic vesicles with or without dense core vesicles	16
S/C	colocalized spherical and dense core vesicles	17
F/C	colocalized elongated and dense core vesicles	–
P/t	pleiomorphic vesicles and many intracytoplamic tubules (not sER)	5

Table 5.1: Types of varicosities

| Type	spindle	sack	other	total
S	7	10	2	19
F	–	–	–	–
P	9	2	5	16
S/C	8	7	1	16
F/C	–	–	–	–
P/T	3	0	2	5
total	27	19	11	57

Table 5.2: Classification of spindle-type and sack-type varicosities

tons according to their vesicular content (see table 5.1). Interestingly, although we do find isolated elongated vesicles in varicosities, we do not find boutons predominantly filled with them. This suggests that a large number of elongated vesicles may be an artifact of fixation or resin embedding.

'S' and 'S/C' type varicosities contain synaptic vesicles, usually more than 10 (80% and 100% respectively). Considering only boutons categorized as clear spindle or sack morphology, the majority of varicosities fall the 'S' and 'S/C' category. Spindle type varicosities are more variable in their content compared to varicosities with sack morphology: 56% of them contain predominantly synaptic vesicles with or without dense core vesicles. In sack-like varicosities, this number rises to 80% (see table 5.2). We categorize varicosities containing more than 10 synaptic vesicles as SV-rich, independent of bouton size and synaptic vesicle density. In the 61 analyzed big boutons, 41 were SV-rich while of the 15 small boutons 6 were categorized as SV-rich. Overall, SV containing boutons are predominant in our dataset, with no significant differences between spindle and sack morphology.
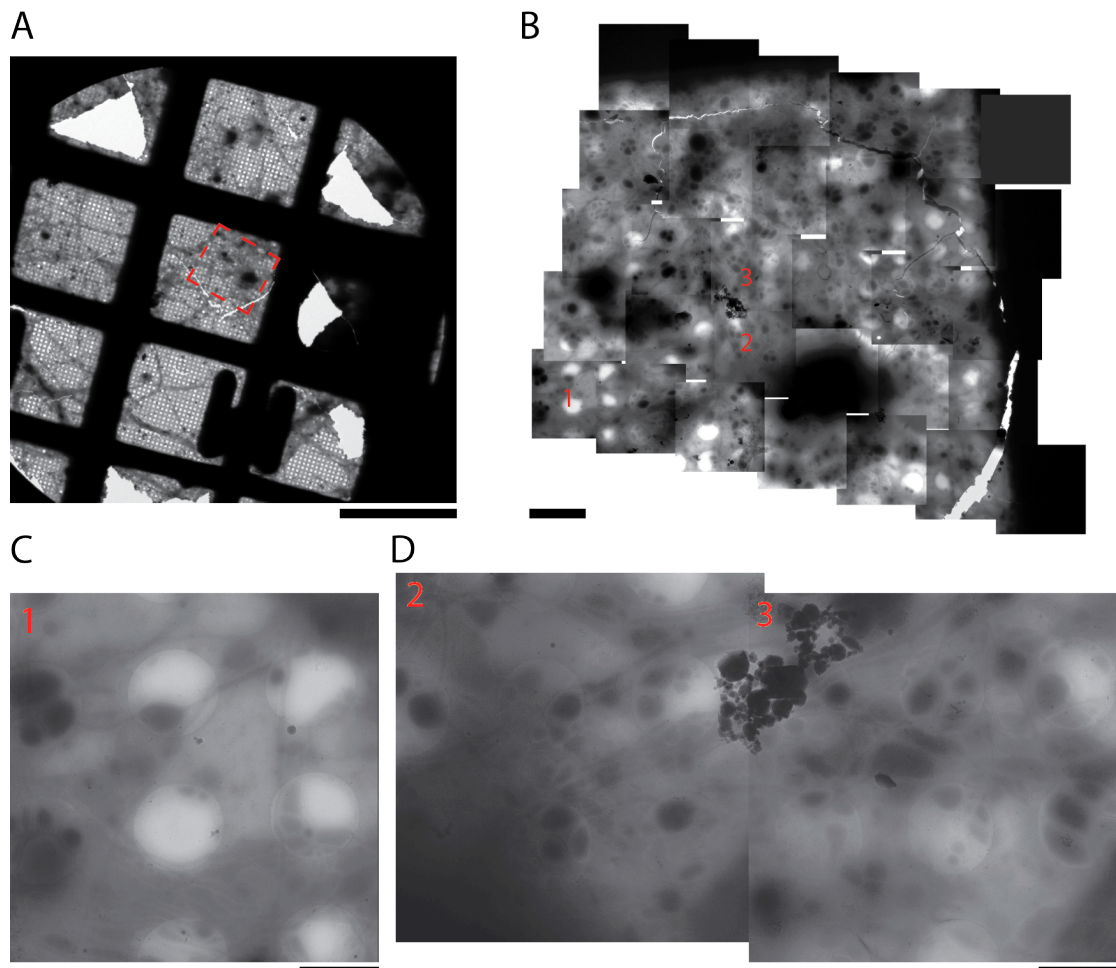
Figure 5.2: Neurons on the grid. **A**: EM image at 100x of neurons at DIV 9. Scalebar 100µm. **B**: Region in (A) marked by red rectangle at 4500x, individual images stiched together manually. Scalebar 5µm. **C, D**: Individual images from B. (D) is rotated by 90°in regard to (B). Scalebars 2µm
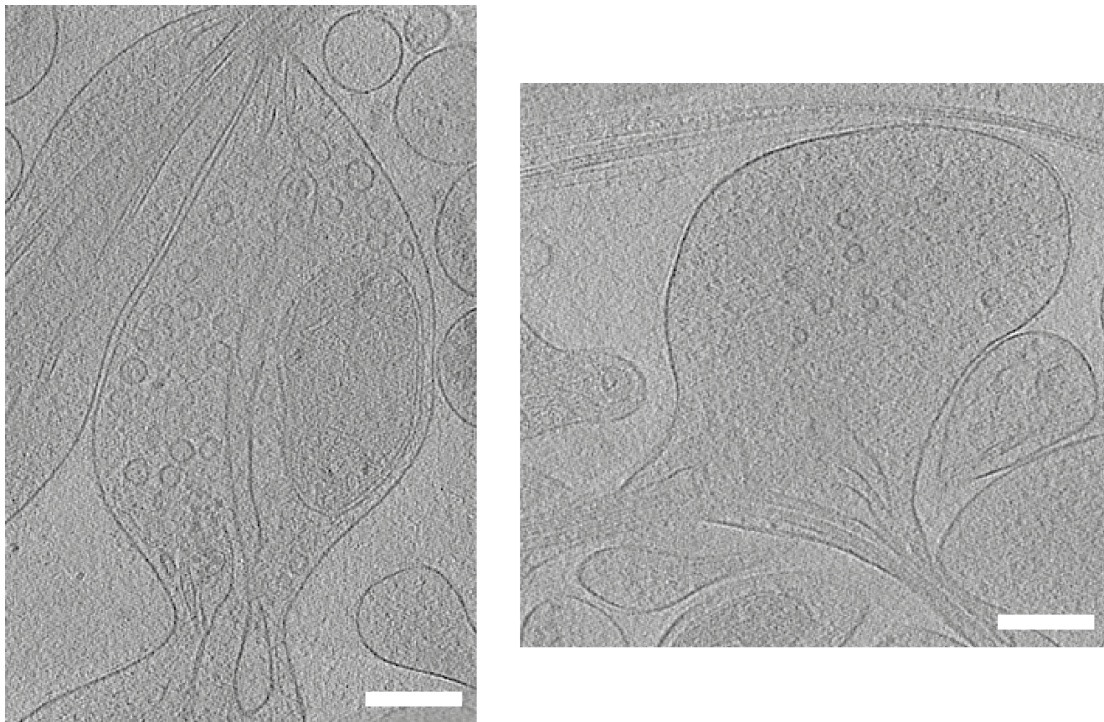
Figure 5.3: Example of different types of boutons. Left: Spindle like P/T type axon with synaptic vesicles, tubular vesicles, membrane compartments and mitochondrion. Right: Sack-like S-type axon with only spherical vesicles and smooth endoplasmic reticulum. Scalebars 100µm.

5.5   The cytoskeleton of axonal varicosities

The predominant cytoskeletal element in axonal boutons are microtubules. With the exception of filopodia and very few, very small processes, microtubules are present in all boutons. They are the main component of the cytoskeleton and an important highway for transportation of proteins and lipids towards the growing end of the processes. They most often occur in pairs or triplets with a median of 4 microtubules per varicosity. We tested if microtubule number follows a Poisson distribution, but found that they do not if processes of all sizes are considered (n = 130 axonal processes, fig. 5.4, A). Therefore, some underlying process must regulate microtubule number in axons.

Only one out of five processes with more than 12 microtubules was rich in other organelles, but such processes may be too thick for direct observation in the EM and therefore elude us. In our data, these microtubule highways are usually devoid of other organelles and only contain isolated or small groups of vesicles embedded within a bundle of microtubules. Interestingly, microtubule disassembly is a very rare event in neurons. In over 160 neurites captured in tomograms, only three events of breaking or ending microtubules have been captured. At the same time, curvatures as high as 2.04 µm^{-1} have been observed without the microtubule breaking. This points to a very high and tightly regulated stability of microtubules in distal axonal processes.

A luminal densitiy within the microtubules can be observed in most tomograms with a sufficient signal to noise ratio (SNR), both as a continuous density over as much as 100 nm and and a punctuated pattern (fig. 5.4, B, C). In the latter case, the density seems to occur at rather fixed distances. To assess if there was a fixed periodicity within the density, we selected microtubules from different tomograms that were oriented in the xy-plane perpendicular to the viewing axis. The pixel values of a line graph along the luminal density were saved and an automated algorithm[2] was used to extract local minima corresponding to luminal densities (fig. 5.4, F). The distance between the minima was on average $13.4nm \pm 4.9$ (n = 74 densities extracted from 5 microtubules from 3 tomograms, fig. 5.4, G), similar to earlier reports [36]. As mentioned before, microtubule disassembly or breakage is very uncommon in neuronal processes. The luminal particles may play a role in regulating microtubule stability or flexibility, as high bending angles lead to significant deformation of the microtubule cross-section. The inter-tubulin binding sites could be stabilized by intraluminal proteins [92]. Another possibility would be that they represent a slow transport mechanism. The depolimerizing kinesin MCAK for example is known to diffuse through microtubules in order to

---

[2]argrelextrema from the signal module in scipy package

target both the plus and minus end more efficiently [42].

Actin can commonly be detected in neuronal processes. We find both cortical actin and actin bundles of 5-10 actin filaments. While cortical actin is found both in axonal boutons and in filopodia, bundles of actin are mostly found in filopodia. Only in two cases we found actin bundles in the lumen of boutons. They are on average 80nm wide and consist of 4-12 filaments. The distance between actin filaments in bundles is ~10 nm. In only two cases we identified actin in processes with more than 10 synaptic vesicles. An actin scaffold surrounding presynaptic boutons as suggested by Malkinson and colleagues for orphan synapses [63] was not observed.

In filopodia, actin bundles can be detected in the filopodia itself and at its base within the neuronal process. Actin is responsible for the proliferation of the filopodia and axonal growth cones can extend in the order of $40\mu/h$. We used automated segmentation in Amira [80] to segment and visualize the actin distribution within and around the filopodia. Actin in within the filopodia is predominantly arranged in bundles pushing the protruding membrane while actin at the base forms a loose network of single actin strands and actin bundles (fig. 5.5). We only detect few short actin filaments in the z-direction (direction of observation). This is likely due to the low thickness of the specimen and the growth of the process on a two-dimensional surface, resulting in a actin network that is build up mostly parallel to the surface.

In fig. 5.5, A a small filopodium is depicted that grows on the carbon support film, adopting a simple actin organizationn. In contrast, the filopodium in fig. 5.5, B is growing over an adjacent neurite. The topology of the actin network hence is much more complex, with actin bundles reaching into the lumen of the varicosity.

Recently Xu and colleagues reported an repetitive actin-spectrin pattern in cultured hippocampal neurons with a periodicity of 182 - 194 nm [102]. They suggest a pattern of actin ring interconnected and spaced by spectrin tetramers. At the pixel-size we collected our tomograms, the field of view spans 1.5 μm. However, we do not observe these actin/spectrin rings in our data. The putative orientation of the actin ring follows the membrane and is perpendicular to the central axis of the process in the specimen plane. Due to the missing wedge the observable section of the ring is almost parallel to the optical axis of the electron microscope, making it challenging to detect such a structure in our data. However, we also could not observe a regular spectrin pattern along the plasma membrane. A possible explanation is the occurrence of these ring-like structures only in larger axons or in axons of a stable diameter. As our data acquisition focused on varicosities and smaller axons these rings might not be present in our dataset.
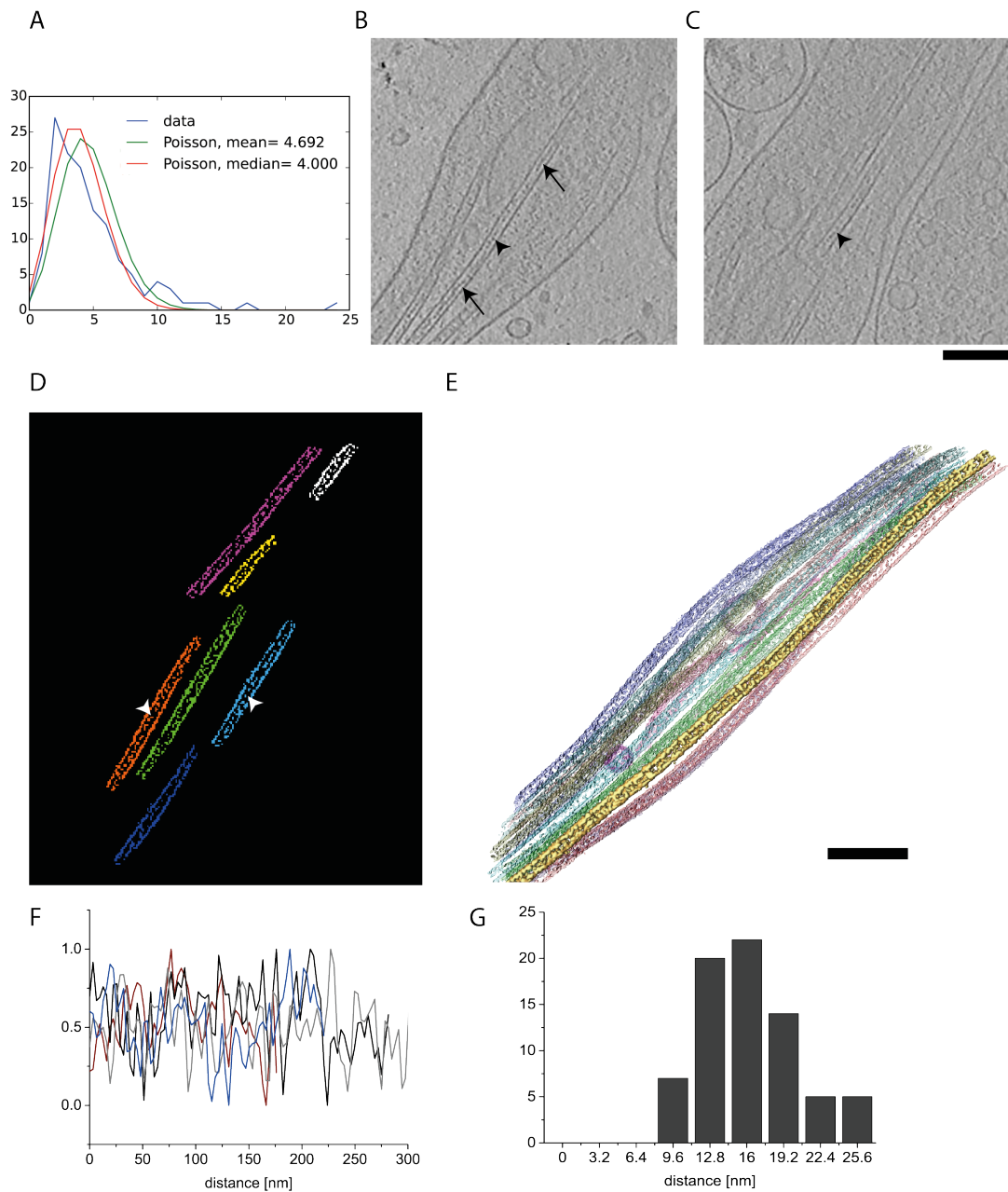
Figure 5.4: Microtubules in varicosities. **A**: Number of microtubules in axonal processes. **B,C**: Slices from tomograms of microtubules in varicosities. Arrow: stretch of continuous luminal density. Arrowheads: punctuated luminal density. **D**: Slice through a tomogram of microtubules at a fixed density threshold illustrates central density. Arrowheads indicate punctuated pattern. Note that not all microtubules are sliced in their central plane. **E** Threedimensional image of the microtubules from (D). **F**: Examples of linegraphs used to measure the periodicity of the luminal density. **G**: Histogram of luminal density spacing. Scalebars 100nm.

A

B
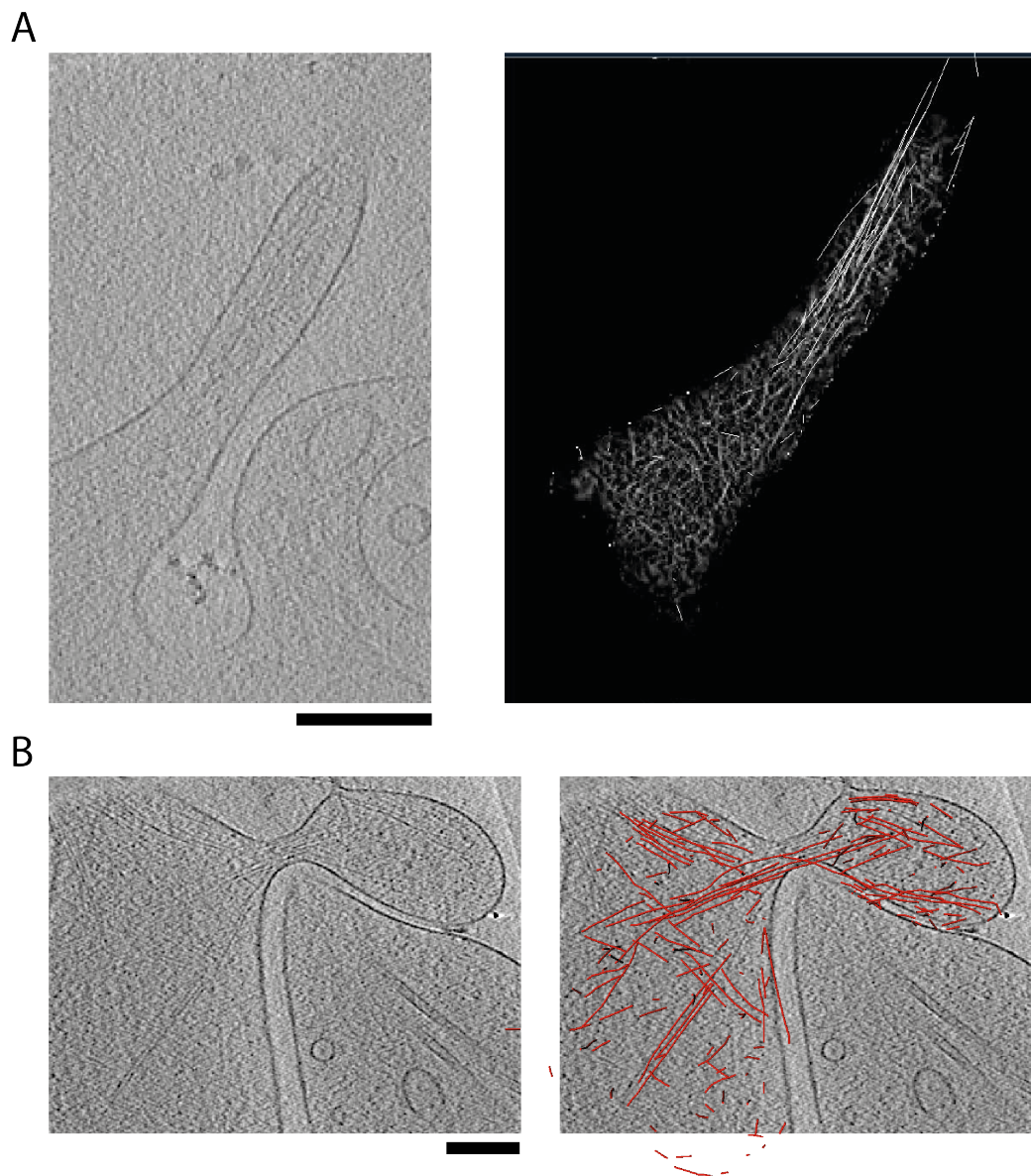
Figure 5.5: Actin structure in filopodia. **A**: Left: Slice through a tomogram of a small filopodium on the carbon support film. Right: correlation field for automated actin detection. Lighter color represents higher correlation values. **B**: Left: Slice through a tomogram of a filpodium crossing another axon. Right: Overlay with the actin detected by the algorithm. Scalebars 200 nm.

5.6 Smooth endoplasmic reticulum and other membranous structures in neuronal processes

A continuous intracellular membrane network that spans almost all neuronal processes was observed in all neuronal processes of sufficient signal to noise ratio. The membranous network was morphologically characterized as part of the distal smooth endoplasmic reticulum (sER). Its function is still not entirely clear but it is postulated to be involved in protein transport or as a Calcium storage.

The network consists of thin tubular membranous structures that frequently expand in diameter to adopt a variety of shapes, from thin tubules or sickles to voluminous sacks. It seems to form a continuous network. In most cases sER closely accompanies the microtubules and can frequently be observed to engulf them. Despite being in close proximity of the microtubules, in less than ten cases of sER we could identify thin filamentous connectors between the sER and the microtubules. An example of sER engulfing a microtubule and also being connected to it can be found in fig. 5.6. It can be difficult to distinguish between vesicles and sER 'bubbles' (yellow in fig. 5.7). Putative connections of the sER to 80nm dense core vesicles and to packs of interconnected synaptic vesicles (see chapter 5.8) are present in a small subset of varicosities.

Multivesicular bodies (MVBs) are an important part of the endosomal pathway and occur frequently in the soma and dendrites of neurons but are more rare in their axons [5]. In our analysis of large axonal boutons, we found 12 multivesicular bodies. They are either round (6 cases) or oval shaped (6 cases) and range in size from 160 to 500 nm, with an average of 280 nm. The number of luminal vesicles was between 4 and 27, with an average of 11. It does not correlate with the size of the MVB. Budding or fusion events were observed in two cases, both in oval shaped MVBs. A segmented MVB with an internal budding site can be found in fig. 5.8. In contrast to a study performed in a human B-cell line, we did not find a Clathrin coat at the edges of the budding sites [67]. Multivesicular bodies fuse into lysosomes to degrade proteins. Lysosomes are more rare than MVBs, with only two occurrences in our dataset.

A

B   C

D

E
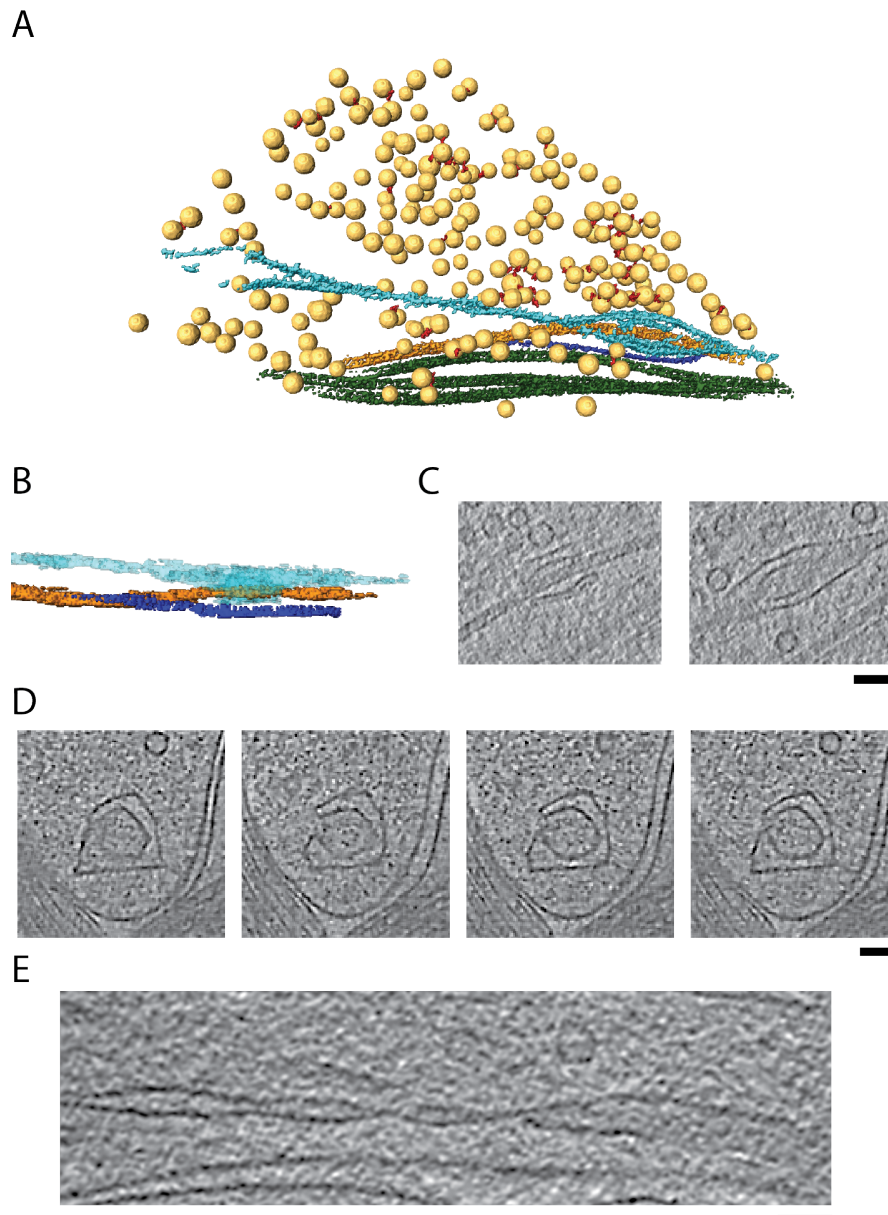
Figure 5.6: Smooth endoplasmic reticulum (sER) in varicosities. **A**: Segmentation of a varicosity including sER (light blue), vesicles (yellow), connectors (red), and microtubules (dark green). Note the filament connecting the sER and the microtubule (dark blue). **B**: Segmentation from (A) rotated by 90° with vesicles and connectors removed. **C**: Slices from the tomogram at the location where the sER engulfs the microtubule. Scalebar 50 nm. **D**: Slices through a tomogram with the sER forming an open cavity. Slices are additionally binned twice in z direction. Scalebar 50 nm. **E**: Slice through a tomogram of long, stretched out sER. Scalebar 50 nm.
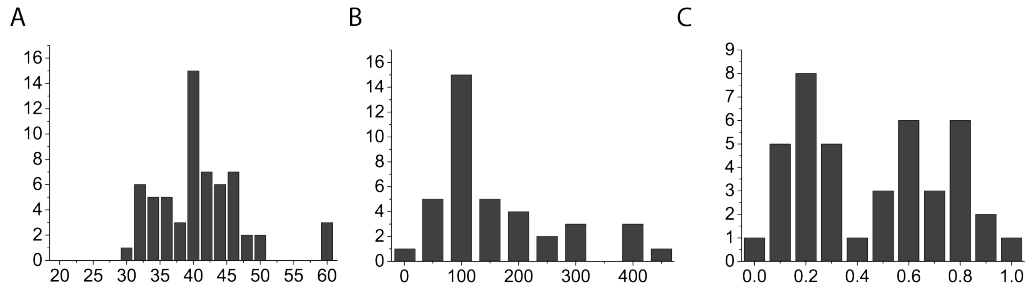
A
B
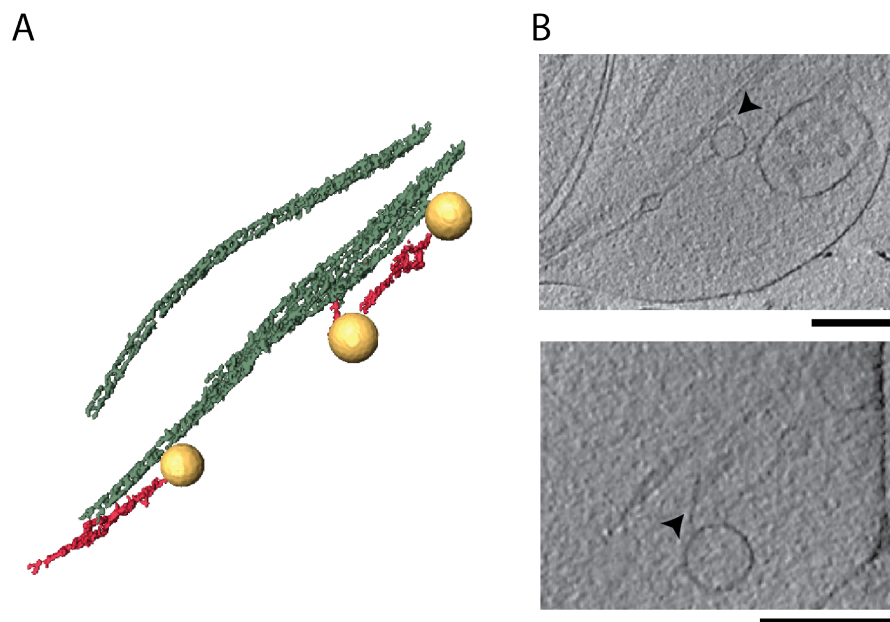
Figure 5.7: A: Smooth endoplasmic reticulum (sER, red) bound to putative vesicles (yellow) and connected to microtubules (dark green). **B**: Slices from the corresponding tomogram. Putative connectors to the microtubule are marked by arrowheads. Scalebar 250 nm.
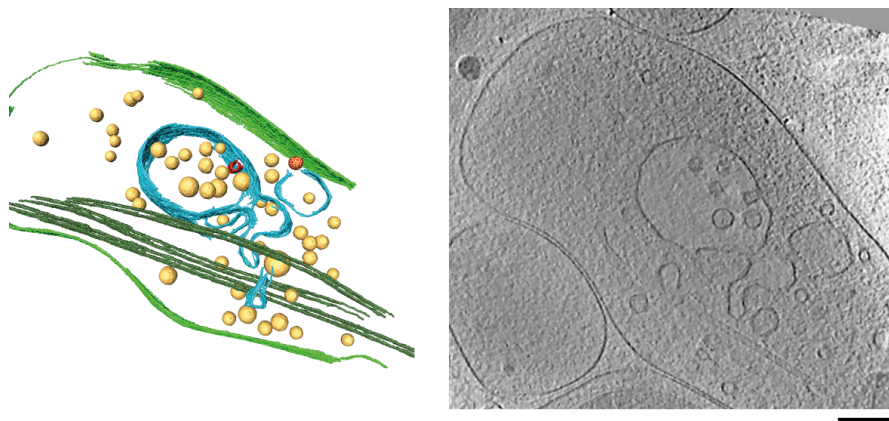
Figure 5.8: Multivesicular body with internal budding site, Scalebar 100nm

5.7 80 nm vesicles

Figure 5.9: Dense core vesicles in varicosities. **A**: Radius histogram of all vesicles identified as having a dense core. Vesicles with a diameter between 70 nm and 90 nm are considered dense core vesicles (DCVs). **B**: Distance of DCVs to the nearest microtubule. **C**: Distance of DCVs to the nearest microtubule as a fraction of the distance between microtubule and plasma membrane.

Varicosities are rich in vesicular content. Apart from synaptic vesicles with an average diameter of ~ 40 nm, vesicles with a radius of around 80 nm occur frequently. In all neuronal processes we find in total 54 vesicles with a radius between 70 nm and 90 nm.

Conventional electron microscopy studies have revealed vesicles of ≈ 80 nm size at axo-dendritic contact sites that show signs of early synapse formation [98]. After staining for conventional EM vesicles show a granular electron density in their lumen and are occasionally decorated with electron dense spicules. They are often termed DCVs. Vesicles of the same size and appearance have been described to be associated with synaptic vesicles in axonal varicosities of developing neurons [89]. After periods of strong synaptogenesis they are depleted from the axons [89] and contain Piccolo, Bassoon and other proteins of the active zone [106]. They are believed to carry protein and lipids required for the formation of active zones [6]. Due to their cargo, they are also referred to as Piccolo/Bassoon transport vesicles (PTVs).

We categorized all vesicles with an radius between 70 and 90 nm as light core, putative dark core and dark core vesicles. In addition to the vesicles we screened all tomograms for the presence of vesicles of all sizes with a dark lumen. The dataset in this study comprised a total of 64 vesicles with a dark lumen. The average diameter was 40.7 ± 8.2 nm (mean $\pm$ std). Among them were 42 vesicles with a vesicle diameter between 70 nm and 90 nm (see fig. 5.9, A), from here on referred to as dense core vesicles, or DCVs. We focused our analysis on those DCVs, because they likely represent PTVs and are functionally different from
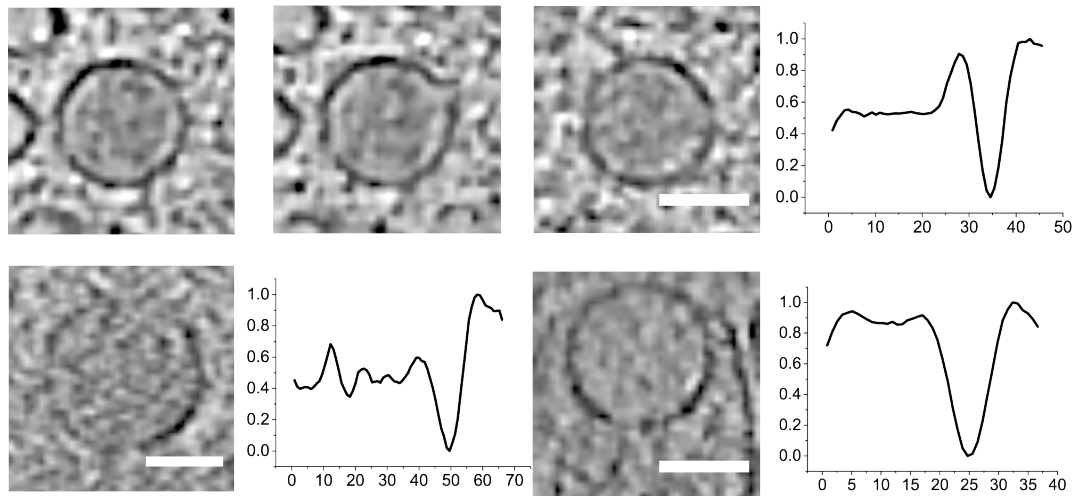
Figure 5.10: Radial profile of dense core vesicles. Upper row: Slices through a dense core vesicle with a prominent halo on the luminal side of the membrane. Right: Radial profile. Bottom row, left: Slice trough a DCV without a halo and corresponding radial profile. Bottom row, right: 100 nm vesicle without a dense core. Scalebars 50 nm

Type	total DCVs	n varicosities
Large varicosities	33	21
(SV rich)	30	19
Small varicosities	4	3
(SV rich)	1	1

Table 5.3: Dense core vesicles in varicosities. DCVs that are not accounted for in the table occurred in tubules.

the dense core vesicles 100 nm in diameter that are responsible for neuropeptide release in mature synapses [40].

Dense core vesicles appear both in small and big boutons, as well as in tubular processes. Most of DCVs were located in large boutons with more than 10 synaptic vesicles present (see table 5.3).

The lumen of DCVs appears darker than the surrounding cytosol with a varying level of granularity. The luminal face of membrane is followed by a lighter region . This can readily be seen when calculating the averaged radial profile of the central slice through a vesicle (see fig. 5.10, upper row). By using this method, we find a lighter halo on the luminal side of the membrane in 30 out of 42 DCVs. In some cases, protusions decorating the vesicle can be distinguished. They range from

very short stubbles to $\sim$ 18 nm long proteins (see fig. 5.11).

While some DCVs are in close proximity of or even connected to microtubules, most appear randomly distributed through the lumen of the varicosity. We measured the distance of each DCV to the nearest microtubule by calculating the distance from its center and subtracting the radius, allowing us to get a reliable measure of distance in three dimensions. A histogram of the distance of DCVs to the nearest microtubules shows a peak at 100 nm (fig. 5.9, B), however this does not take the size of the varicosities into account. An analysis of the distance to the nearest microtubule relative to the distance between microtubule and plasma membrane points to a distinct population closer to the microtubule (fig 5.9, C).
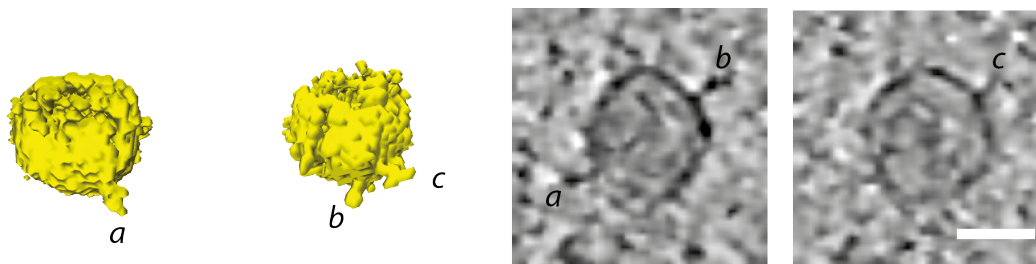
**Figure 5.11:** Proteins decorating a dense core vesicle. Scalebar 50nm
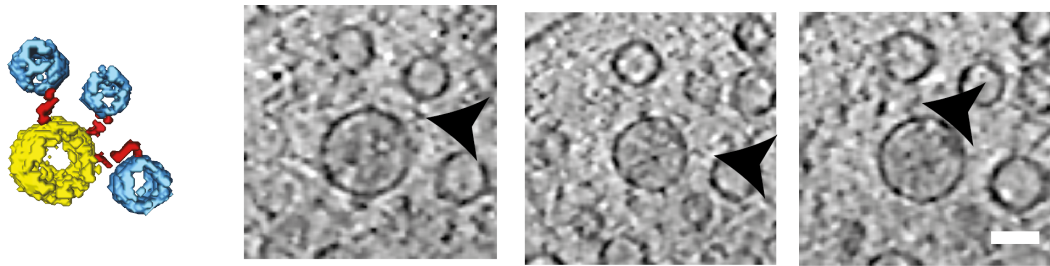
Figure 5.12: Example of a dense core vesicle connected to multiple synaptic vesicles. Scalebar 50nm.

5.8 Transport processes in Axons

In the developing neuron, the proteins and lipids required for synaptogenesis and synapse maintenance are constantly transported towards the distal processes. We were specifically trying to locate such transport processes in our tomograms. We did not restrict our analysis to big boutons but also investigated small boutons and processes without varicosities. All processes were screened for vesicles or other organelles connecting to microtubules.

Dense core vesicles (DCVs) have been implicated in synaptogenesis (see section 5.7). We find that some of these DCVs in proximity of microtubules form connectors. Of all DCVs, 9.5% connect to microtubules. This fraction rises to 17% if we only consider DCVs closer than 100 nm to microtubules. However, not all connectors might be detected by visual inspection as the three-dimensional positioning of putative connectors and the signal to noise ratio impede their detection. As mentioned in the previous section 5.7, DCVs are most commonly located ~100 nm apart from the microtubules. Kinesin I is the most likely candidate to transport PTVs, but likely other proteins are involved in linking the DCV to the motor protein [91].

33 out of 42 DCVs were found in varicosities with 10 or more synaptic vesicles and 11 DCVs showed putative connections to synaptic vesicles (fig. 5.12). We find a mix of short connectors and longer filaments, with an average length of 38 ± 3.1 nm (mean $\pm$ sem, n = 31 connectors). Notably, this is significantly larger than the average length of connectors between synaptic vesicles. While we do see more very long connectors by visual inspection between DCVs and synaptic vesicles than among synaptic vesicles alone, all statistical analysis on the connectors among synaptic vesicles was done by an automated detection algorithm that often fails to detect very long connectors. Therefore, a direct comparison between the connector length among synaptic vesicles in boutons from our statistical analysis (see ch. 5.9:
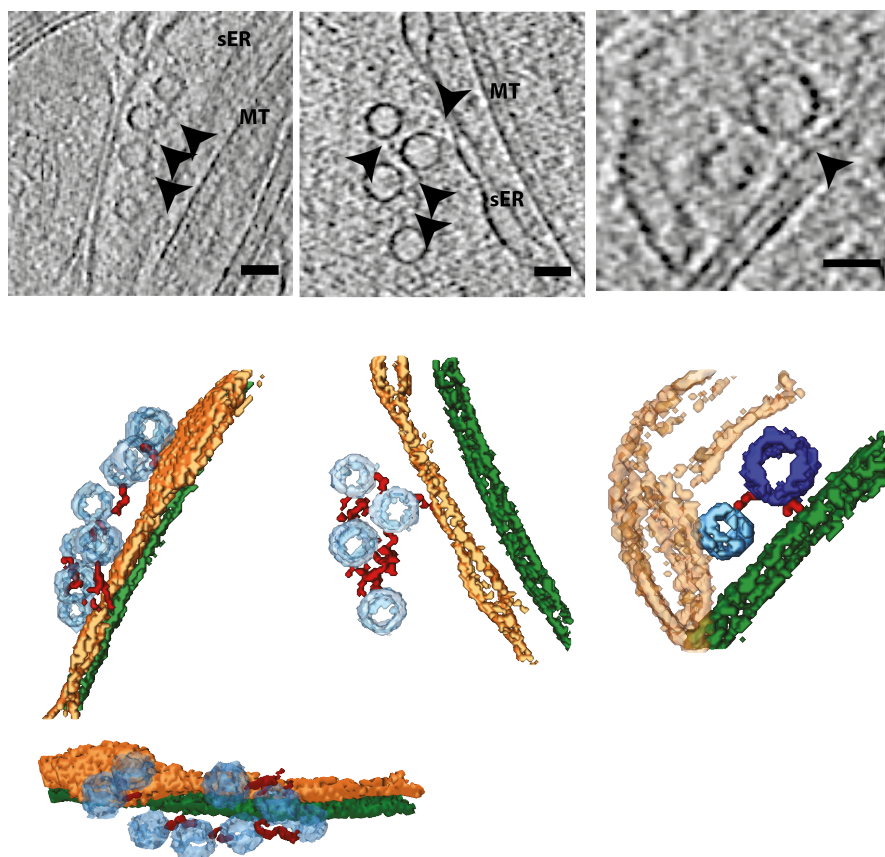
Figure 5.13: Small groups of tightly spaced vesicles (typically 4-8 ves.) often appear to be organized in strings of synaptic vesicles (left) as well as cluster-like packages (middle). Both are frequently aligned with smooth endoplasmatic Reticulum (sER) or microtubules (MT). In some cases, larger vesicles or dense core vesicles are also present (right). Scalebars 50 nm.

12.6 ± 1.7 nm, mean $\pm$ sem) and the connector length between DCVs and synaptic vesicles is not possible.

While DCVs close to microtubules occur either alone or in pairs, synaptic vesicles close to microtubules often occur in packs of five to ten vesicles. They appear to be interconnected loosely. Vesicle packs are present in two conformations: A string-like and a cluster-like confirmation (see fig. 5.13 left, middle). Packs of synaptic vesicles seem to engage and disengage microtubules, as similarly ordered packs of vesicles can also be found a considerable distance apart from the microtubules.

Larger vesicles and membrane sacks being connected to microtubules are also visible. Similar to the PTVs with a dark core described in the previous section,

tubular vesicles are also thought to be involved in the transport of newly synthesized proteins in axons [68]. In particular we found four cases of tubular vesicles in close proximity to or even surrounded by microtubules. Other, SV sized vesicles present form a row. Cluster-like configurations have not been observed. However, we could not detect any connectors among the vesicles. It is known that vesicular cargo frequently detaches and reattaches during the transport process, so tubular vesicles further than 100 nm from the microtubules are also candidates for transport vesicles. However, neuronal processes are full of membrane compartments of varying size and shape, so tubular vesicles further than 100 nm from microtubules were not considered as putative transport processes.

In summary, we were able to capture and visualize putative transport events *in situ*. PTVs both connected to synaptic vesicles and isolated as well as packets of synaptic vesicles are the major type of transport observed in our dataset, while tubular structures appear less frequently.
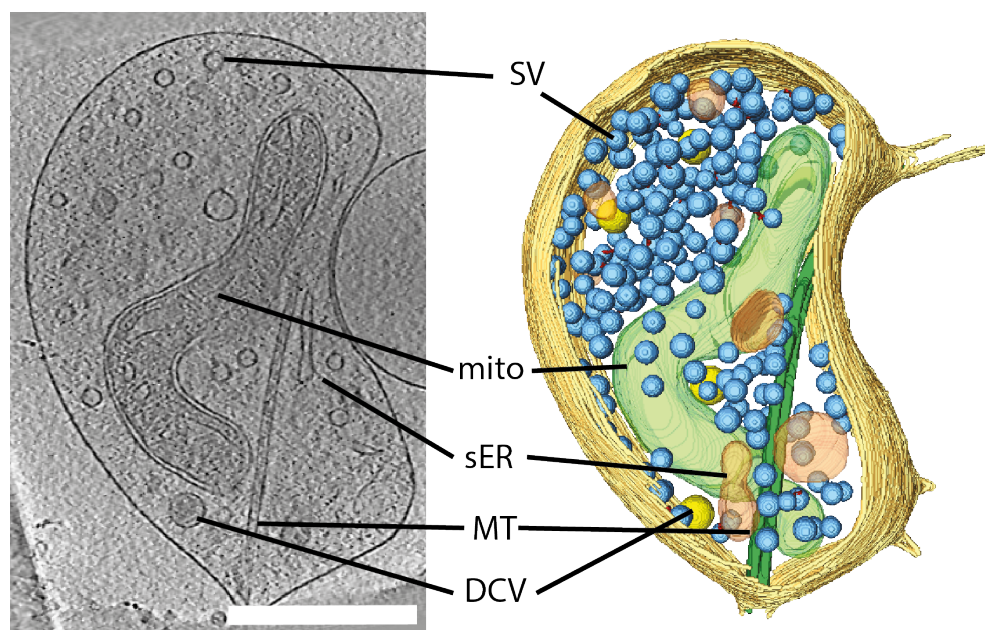
Figure 5.14: Example of a segmented bouton for analysis. Connectors detected by automated analysis are depicted in red. SV: synaptic vesicle, mito: mitiochondion, sER: smooth endoplasmic reticulum, MT: microtubule, DCV: dense core vesicle. Scalebar: 500nm

5.9   Analysis of presynaptic boutons

When stimulated, a fraction of varicosities in neurons grown in culture will undergo vesicle exocytosis and re-uptake [54]. However, the number of synaptic vesicle and active zone associated proteins in these orphan synapses is much lower compared to synapses [54]. The fact that vesicle exocytosis in orphan and mature synapses can be strongly attenuated by Tetanus toxin, and thus rely on VAMP2, indicates that both rely on a similar molecular machinery [54]. In *Aplysia* neurons, synaptic vesicles move in concert with the varicosities in an actin dependent manner [63].

We selected a subset of big boutons with a high number and density for analysis. 13 technically good boutons with with sufficient contrast for automated detection of connections among the vesicles and to the membrane were chosen. Among them were two dual-tilt tomograms, two tomograms collected on the carbon support film and on tomogram collected on a direct detector instead of a charge coupled device (CCD) camera. After manual segmentation of organelles, membranes and the median disk of vesicles, connectors among synaptic vesicles and tethers between vesicles and the enclosing membrane were automatically detected [29]. An example of a segmented bouton can be found in figure 5.14 and an overview over the selected
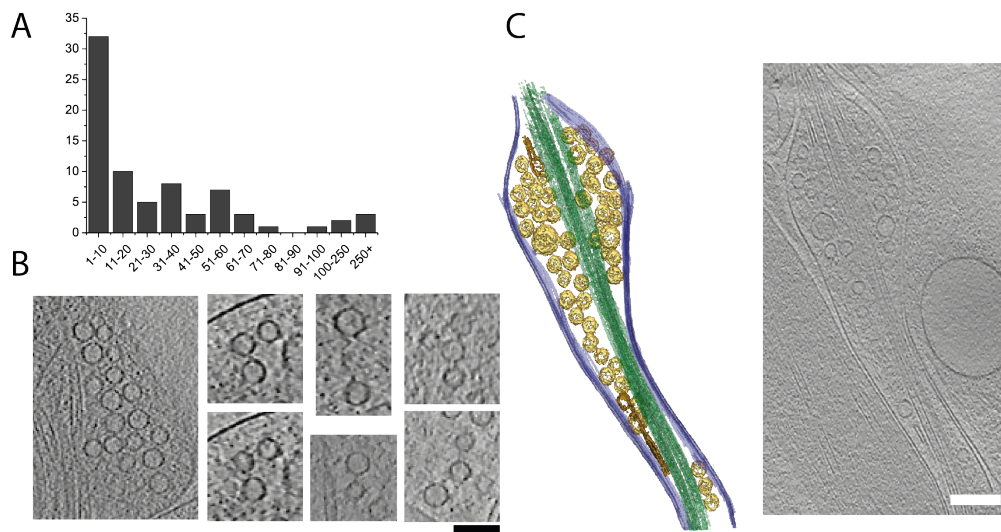
Figure 5.15: Synaptic vesicles in presynaptic boutons. **A**: Histogram of the number of synaptic vesicles in varicosities with more than 10 synaptic vesiclesW. **B**: Examples of connectors in presynaptic boutons. Scalebar 100 nm. **C**: Example of a small bouton with many vesicles. Scalebar 200 nm.

boutons is presented in table 5.4.

In presynaptic bouton, i.e. boutons that have a high number and density of synaptic vesicles, we detect connectors among the vesicles as well as tethers between the vesicles and the plasma membrane. We find that 58% of synaptic vesicles are connected, with an average of 1.8 ± 0.2 connectors per vesicle (mean ± sem). While the length and coarse morphology of the connectors are similar to those formed in mature synapses, the interconnectivity of the vesicles less pronounced compared to mature synapses. The fraction of connected vesicles and the amount of connectors per vesicle are both lower compared to our results from synaptosomes. Furthermore, the clusters of vesicles are smaller compared to mature synapses: We only find 14% of vesicles are in the largest cluster.

In order to test if vesicle arrangements similar to the synaptic vesicle packs described in section 5.8 exist in boutons with a high amount and density of synaptic vesicles, we performed a clustering analysis based on vesicle connectivity and vesicle distance. The cutoff for clustering by distance has to be chosen by visual inspection. A value of ~15 nm was used for most tomograms. Both clustering methods produced similar results with small differences in cluster size and shape. The detected vesicle clusters were mostly in the shape of the 'cluster'-type, and

Category	N boutons	SV analyzed	Proximal SVs	Connectors	Tethers
Under 100 SVs	9	845	77	326	136
Over 100 SVs	4	413	10	1129	30
DCV	6	515	57	342	110
no DCV	7	743	30	1131	56
total	13	1258	87		166

**Table 5.4:** Overview of analyzed presynaptic boutons.
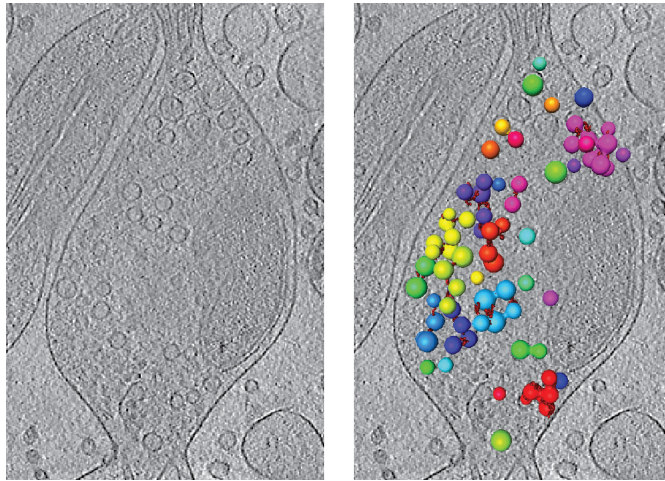
Figure 5.16: Clustering analysis of synaptic vesicles. Vesicles with the same color are interconnected. Scalebar 250 nm

only few string-like vesicle arrangements were found in the 13 boutons. Clustering by distance proved to be better in identifying strings of vesicles, because this clustering method does not depend on the sv connectivity.

The number of connections among the vesicles scales with their total number and density in the varicosity. We split our dataset into two categories: boutons with more than 100 SVs and boutons with less than 100 vesicles[3]. In varicosities with over 100 synaptic vesicles, 65.6% of SVs are connected to at least one other SV while in varicosities with less than 100 SVs only 42.4% are connected (p < 0.001 by paired t-test, see fig. 5.15, A). In varicosities with many synaptic vesicles, we therefore find a fraction of vesicles that are interconnected close to mature synapses (75%, compare ch. 6.4).

The number of connectors per synaptic vesicle also depends on the total number of

---

[3]Over 100 SVs per bouton: 4 boutons, 845 SVs in total; less than 100 SVs per bouton: 9 boutons, 413 SVs in total.
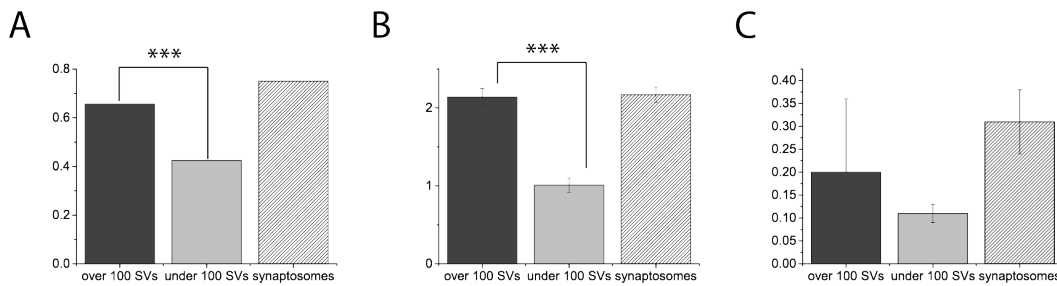
Figure 5.17: Statistical analysis of varicosities. In all graphs: Dark grey: over 100 SVs per bouton, n = 4 boutons, 845 SVs. Light grey: less than 100 SVs per bouton, n = 9 boutons, 413 SVs. Pattern: Data from wild-type synaptosomes, see chapter 6. **A**: Fraction of connected SVs. **B**: Number of connectors per synaptic vesicle. **C**: Amount of vesicles in the largest cluster.

vesicles. In boutons with more than 100 SVs, vesicles have on average 2.14 ± 3.08 connectors per vesicle, while in boutons with less than 100 SVs vesicles are on average only connected by 1.01 ± 1.82 filaments (p < 0.001, fig. 5.15, B).

The presynaptic boutons selected for analysis differ not only in total vesicle number, but also in the other organelles present in the bouton. We can therefore classify and analyze the dataset according to different features present in the varicosities. It has to be taken into consideration that the total number of varicosities, and ideally, the total number of synaptic vesicles analyzed in each category are balanced. This limits the parameters for classification.

We categorized the presynaptic boutons according to the presence of dense core vesicles (DCVs)[4], where we follow the definition of DCVs from chapter 5.7: vesicles with a dark lumen and a diameter of 70 - 90 nm. We found that in boutons lacking DCVs synaptic vesicles are more highly interconnected compared to boutons containing DCVs. In varicosities containing DCVs, only 43.1% of SVs are connected to at least one other SV, while this fraction rises to 68.2% in varicosities lacking DCVs (p < 0.001, Chi-square test, see fig. 5.18, A). The number of connectors per synaptic vesicle is significantly increased as well: in the presence of DCVs, SVs are connected on average by 1.09 ± 0.14 connectors (mean $\pm$ sem, n = 515 connectors), while in the varicosities without DCVs this number rises to 2.24 ± 0.09 (mean $\pm$ sem, n = 743 connectors, p < 0.001 by Kruskal-Wallis test).

In big boutons, synaptic vesicles are clustered towards the middle, leaving few vesicles in close proximity to the membrane. In the 13 boutons included in the

---

[4]DCV containing varicosities: 6, with 515 SVs in total; varicosities without DCVs: 5, with 743 SVs in total.
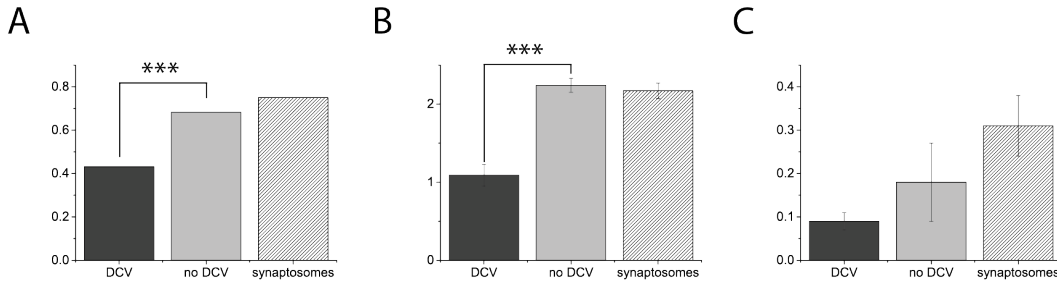
Figure 5.18: Statistical analysis of varicosities. In all graphs: Dark grey: DCVs present, n = 6 synapses, 515 SVs. Light grey: no DCVs present, n = 7, 743 SVs. Pattern: Data from wild-type synaptosomes, see chapter 6. **A**: Fraction of connected SVs. **B**: Number of connectors per synaptic vesicle. **C**: Amount of vesicles in the largest cluster.

analysis, we only find 87 proximal vesicles[5]. This equates to 2.15 ± 3.15 proximal SVs per µm^2 membrane and 15.83 ± 17.42 proximal SVs per µm^2 membrane for over and under 100 SVs containing boutons respectively. In mature synapses we find many more proximal vesicles, typically in the order of 80 to 100 proximal SVs per µm^2 active zone (see section 6.3). While the number of proximal vesicles per µm^2 membrane is significantly lower in varicosities compared to mature synapses, one has to take into consideration that the calculation for varicosities uses the entire membrane enclosing the varicosity that is visible in the tomogram while the calculation for synaptosomes uses the active zone as a measure where vesicles are concentrated. Depending on the vesicle distribution there can be large parts of the membrane that do not have any vesicles close to them. In contrast to big boutons, small tube-like varicosities often have many vesicles very close to the membrane due to the physical restriction of the membrane (see for example fig. 5.15).

Analyzing the differences in vesicle distribution in dependence of the presence of DCVs shows the importance of checking the results for individual boutons, especially if they are varying in many parameters as size, other organelles, total vesicle number and vesicle distribution. Looking at the number of proximal vesicles we find no statistical significant difference: In DCV containing boutons we find 15.8 ± 5.6 (mean $\pm$ sem) proximal vesicles per μm^2 membrane and in boutons without DCVs we find 8.04 ± 6.6 (mean $\pm$ sem) proximal vesicles per μm^2 membrane. The larger error in the latter category stems from one single bouton that is more closely confined by the surrounding membrane than most other boutons. Excluding this one bouton the mean number of proximal SVs in boutons without DCVs is reduced to 1.5 ± 1.10 per μm^2 membrane (mean $\pm$ sem, p < 0.05 by

---

[5]Total numbers: over 100 SVs: 10, n=4; under 100 SVs: 77, n=9.

Student's t-test).

It is known that at least a subset of presynaptic boutons lacking a postsynaptic partner are capable of synaptic vesicle release. In order to undergo exocytosis and release their neurotransmitter, synaptic vesicles are tethered to the membrane of the active zone in mature synapses. We therefore investigated if similar tethers are present in presynaptic boutons. As noted before, the number of proximal vesicles in presynaptic boutons is small compared to mature synapses. Therefore, we only find a small total number of vesicles tethered to the membrane. In all analyzed boutons together, 41 out of 87 proximal vesicles are tethered (47%). In boutons containing DCVs, where more proximal vesicles are present, we find that 60% of the proximal vesicles are tethered to the membrane, while boutons without DCVs are almost devoid of tethered proximal vesicles.

5.10   Shedding light on presynaptic boutons

Using cryo-electron tomography (cryo-ET) we can directly visualize developing neurons *in vitro*. While the axonal growth cone is often too big to access entirely - often measuring more than a micrometer in diameter [74], we can capture growing neurites and their filopodia. As a structural technique, the functional information cryo-ET can provide is limited. This limitation can be lifted by complementing the EM data with fluorescent labeling of proteins of interest. While we could capture many putative transport processes and boutons rich in synaptic vesicles in our data, further work on the correlative approach is necessary to unambiguously identify transport packages like Piccolo-Bassoon transport vesicles in cryo-ET tomograms. The light microscopy resolution and the correlation precision need to be improved to identify individual processes in the dense carpet of neurites.

In order to successfully target synapses in cultured neurons, advances will have to be made in the three dimensional correlation of features in the light and electron microscope. Synapses in the distal regions were too sparse to be routinely detected in our low density cultures and the proximal region was inaccessible without further thinning steps. Focused ion beam milling (FIB milling) allows thinning of samples down to ~100 nm thickness by preparing lamella or wedges of the sample. Capturing a synapse within a 150 - 300 nm thick lamella requires precise location of the synapse in three dimensions. While this was not possible with our setup comprising a Zeiss inverted light microscope together with the Cryostage^2, it may become an option with the CorrSight, developed by TIL Photonics. In addition, FIB milling requires two additional transfers yielding a higher risk of contamination or loss of the sample.

We could show that varicosities are abundant structures varying greatly in size and content. Many of the organelles present in varicosities are linked by filamentous connectors. These appear to be ubiquitous structures in neurons ranging from short connectors among synaptic vesicles to longer filaments linking for example the smooth endoplasmic reticulum (sER) to microtubules. These filamentous connectors are likely of different origin, but even connectors among synaptic vesicles may differ between presynaptic boutons and transport packages and may serve a unique function.

Synaptic vesicles interconnect in a similar manner in presynaptic boutons and in mature synapses. However, the size of synaptic vesicle clusters in these boutons is smaller. In addition, fewer vesicles are located towards the plasma membrane or tethered to it. It remains to be seen whether the connectors among synaptic vesicles in presynaptic boutons and mature synapses consist of an identical protein composition as those in mature synapses. We cannot say for sure if all of the

presynaptic boutons analyzed represent orphan synapses, because a correlation with FM-dye fluorescence was not established for all tomograms in our dataset. Furthermore, not all locations of FM-dye puncta correlated with boutons that fall under the 'presynaptic bouton' category. While synaptic vesicles and in some cases dense core vesicles (DCVs) are present in almost all varicosities correlated to FM-dye puncta, their density can vary greatly.

The differences in presynaptic boutons depending on the presence of DCVs point to a putative functional difference during synaptogenesis. Dense core vesicles occur either isolated or connected to synaptic vesicles (see ch. 5.7) and only rarely to other organelles. After phases of strong synaptogenesis, they are depleted from axons in developing neurons suggesting that they are transport vesicles involved in synaptogenesis [89]. It is likely that the DCVs observed represent Piccolo/Bassoon transport vesicles (PTVs). The lack of DCVs in some boutons is most likely not the result of them already fusing with the membrane, a step that is thought to occur during formation of the synapse, but presynaptic boutons lacking DCVs may represent an earlier or more immature type than those with DCVs. The packing further away from the membrane and the higher interconnectivity also support this idea.

Our correlative data is not sufficient to distinguish the role of dense core vesicles in growing neurons. While we did not establish a correlation with fluorescent data for all tomograms included in the analysis, we find tomograms collected at spots of FM-dye fluorescence in both categories, with and without DCVs. This suggests that the vesicles both with and without DCVs can undergo membrane fusion and vesicle recycling.

Chapter 6

α-Synuclein studies

6.1 α-Synuclein and Parkinson's disease

The publication of the results of this chapter is in preparation. It is a collaborative effort with Karen Vargas[1], Chriss Westphal[1], Ruben Férnandez-Busnadiego[2] and Sreeganga Chandra[1]. Karen Vargas and Nikolas Schrod share first authorship.

Author contributions:

Karen Vargas* Immuno-EM, Biochemistry

Nikolas Schrod* Cryo-electron tomography and analysis

Chriss Westphal Biochemistry

Ruben Férnandez-Busnadiego Preparation of synaptosomes

**Vladan Lucic** Study design, supervision of N.S.

Sreeganga Chandra Study design, supervision of K.V. and C.W.

Parkinson's disease affects over 4 million worldwide with a prevalence that strongly depends on age [76]. Parkinson's disease is characterized by muscular tremor and rigidity, as well as slowed movement and postural instability [47]. The dopaminergic neurons in the substantia nigra undergo apoptosis as the disease progresses. In addition to motoric impairments, this can lead to neuropsychiatric symptoms in patients.

---

[1]Yale University, New Haven, CT, United States
[2]Formerly Yale University, now MPI for Biochemistry
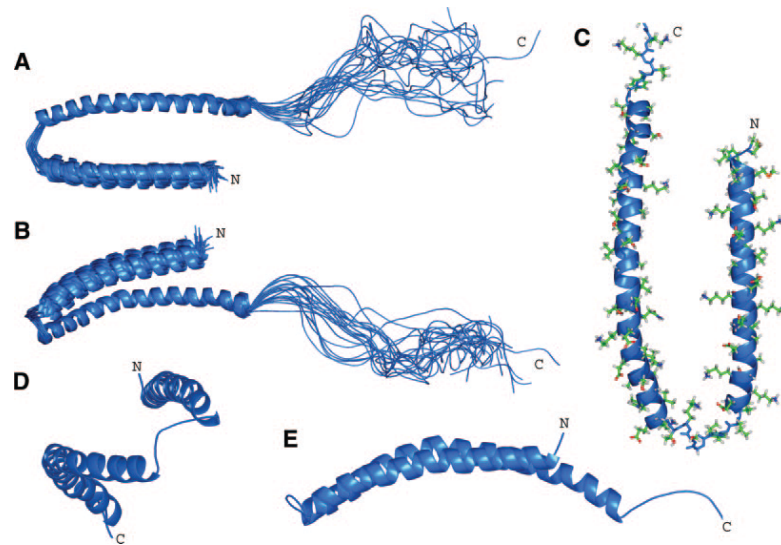
Figure 6.1: The structure of α-synuclein. α-synuclein forms a broken amphiphatic helix upon binding to a lipid bilayer. From [94]

Parkinson's disease was first described in 1817 by the english doctor James Parkinson's, in an empiric study of six subjects, one of which he only observed from afar [72]. In the following years, many advancements in the description and treatment of the disease were made, pioneered by Jean-Martin Charcot who also suggested the name to the disease. He also established the treatment of Parkinson's disease with belladonna alkaloids [71]. Their anticholinergic effect made them the treatment of choice for a long time, together with surgical treatments, until the development of Levodopa (or L-DOPA). Although being firstly synthesized in 1911, Levodopa did not enter clinical trials until 1967 when it lead to a new era in the treatment of Parkinson's disease. Early surgical treatments were mostly unsuccessful until Irving S. Cooper accidentally severed the anterior choroidal artery during a brain surgery in 1953 [14]. The resulting reduction in tremor and rigidity was significant and led to a wider prevalence of this therapy despite a mortality rate of about 10%. The advent of surgery came to a halt with the widespread therapeutic use of Levopoda.

Frederic Lewy discovered aggregates in the brain of deceased Parkinson's patients, later termed Lewy bodies. They consist mainly of α-Synuclein, an 140 kDa protein abundant in the central nervous system. α-Synuclein forms an broken amphiphatic helix when bound to lipid bilayers with an affinity that depends on the membrane curvature (fig. 6.1). In vitro studies suggest that α-Synuclein can not only sense, but also induce membrane curvature [66, 75, 97]. Most cases of Parkinson's are idiopathic, however, mutations in several proteins have been linked to the disease.

Among them are the parkin and most notably α-Synuclein where five point mutations have been identified. The A30P point mutation disturbs the amphiphatic helix and reduce the binding affinity to lipid bilayers [48, 55].

It is still under discussion if α-Synuclein aggregates or its oligomers are toxic to cells, but it has been shown that α-Synuclein fibrils injected in a healthy mouse brain can act in a prion like fashion and induce aggregation of native α-Synuclein in a similar pattern as observed in Parkinson's [61]. It is widely believed that α-Synuclein is an unordered monomer if not bound to a membrane, but it has also been suggested that it instead forms an iso-tetramer in its unbound state and that its ability to do so is impaired in mutations that are known to cause Parkinson's disease [4]. Despite its prevalence in Parkinson's disease and abundance in the central nervous system, the physiological function of α-Synuclein is not well understood.

6.2   Investigating the function of α Synuclein

Due to the prevalence of Lewy-bodies in Parkinson's disease, numerous studies have been conducted in animals overexpressing α-Synuclein or lacking one or all variants of the protein. Despite the abundance of α-Synuclein in the central nervous system, the effects of an Synuclein triple-knockout are relatively mild. Animals lacking all three forms of Synuclein die of younger age and exhibit minor motoric defects that correlate with the animal's age [39]. Classic electron microscopy revealed a reduction in resting pool vesicles in α-Synuclein knockout mice [11], while others reported only a reduction in the area synaptic vesicles were occupying without a change in numbers [39]. Synuclein-null-mice have higher basal transmission and a higher evoked response compared to their wildtype littermates. In response to the knockout, some synaptic proteins are up- or downregulated. Among the upregulated proteins are synapsin, complexin and amphiphysin, while the Synaptobrevin-2 is progressively downregulated with age [10].

The effects of α-Synuclein overexpression strongly differ between the expression of human α-Synuclein and mouse α-Synuclein in mice. While the effects of mouse α-Synuclein overexpression are negligible, mice overexpressing the human variant are being used as a model organism for Parkinson's disease.

Overexpression of α-Synuclein in mice leads to a reduction of the levels of various proteins, most of which are upregulated in TKO mice. Notable additions are Synaptobrevin/VAMP2[1] and Synaptophysin that are downregulated. The SNARE[2]-complex protein SNAP25[3] and synaptotagmin are expressed at elevated levels in α-Synuclein overexpressing mice [69].

In order to investigate the function of α-Synuclein in the healthy brain, we analyzed synaptosomes from animals lacking all three isoforms (triple-knockout, TKO) and compared them to wild-type (WT) animals. In addition, we investigated different overexpression systems: overexpression of human α-Synuclein (αOX), overexpression of human α-Synuclein on a TKO background and overexpression of the A30P mutation variant of α-Synuclein.

Synaptosomes are purified synapses from the neocortex. They retain their pysiological function for hours and are small enough to be directly accessible to cryo-EM. Importantly, they retain their ultrastructure and the filamentous connectors interlinking the vesicles (termed 'connectors') and linking vesicles and the active zone membrane (termed 'tethers') [30].

---

[1]vesicle associated membrane protein 2 (VAMP2)

[2]soluble NSF-attachment protein receptor (SNARE)

[3]synaptosomal associated protein, 25kDa (SNAP25)
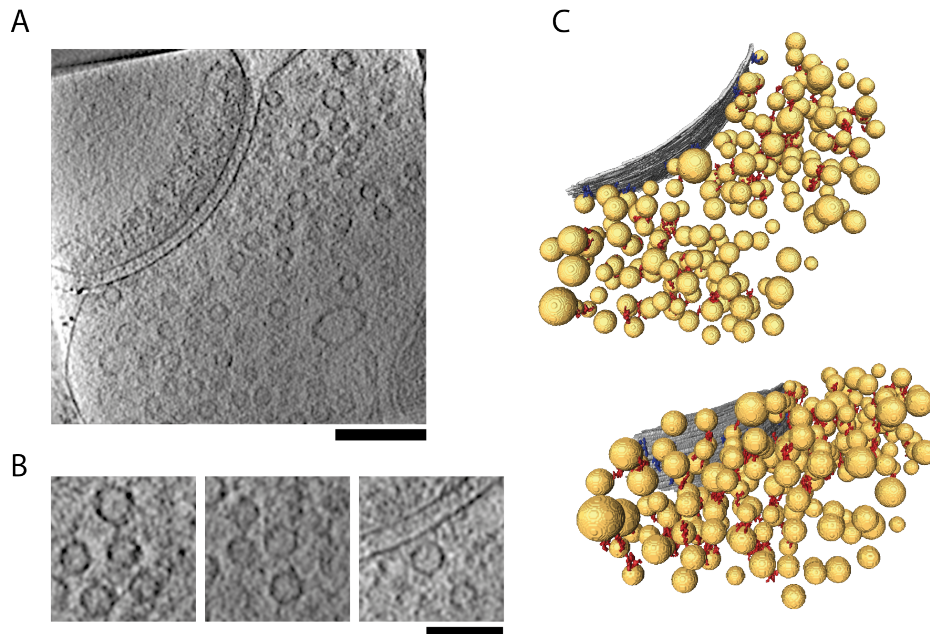
Figure 6.2: Segmentation of a synaptosome prepared from α-Synuclein triple knockout mice. **A**: Slice through tomogram. Scalebar 200nm. **B**: Synaptic vesicles with connectors (left, middle) and tethers (right). Scalebar 100nm. **C**: Segmented vesicles (yellow), active zone (grey), tethers (blue) and connectors (red)

We analyzed all tomograms of healthy synapses, namely those that included an enclosed presynaptic compartment, a complete postsynaptic density, a mitochondrium, intact spherical synaptic vesicles and a signal-to-noise ratio that allowed the detection of connectors in between the synaptic vesicles. A summary of the analyzed data can be found in table 6.1.

Treatment	Animals	Synapses	SVs	Connectors	Tethers
Wildtype (WT)	3	10	760	1176	56
Triple-knockout (TKO)	3	7	718	820	182
Overexpression of human α-Synuclein (αOX)	2	6	535	1089	53
αOX on TKO background (αOX on TKO)	2	9	756	2055	195
Overexpression of A30P mutant	3	10	830	1593	173

Table 6.1: Overview of synaptosomes selected for analysis

6.3   The morphology of synapses is not affected by α-Synuclein deficiency or overexpression

Firstly, we compared the overall morphology of the synapse among the different genotypes. Synaptosomes retain the native structure of the synapse [30]. In order to remove the influence of synapse size, we analyzed the first 250 nm from the active zone. Synapses of all genotypes showed normal vesicle distribution, characterized by the accumulation of vesicles in direct vicinity of the membrane (termed 'proximal vesicles'), followed by an intermediate zone (45-75nm from the AZ) with a significantly lower density of vesicles. The distal zone at > 75nm contains the majority of synaptic vesicles and has a higher vesicle density than then intermediate zone (see fig. 6.3, A).

We next surveyed the amount of proximal vesicles at the active zone. If these vesicles are tethered to the membrane they can be primed for neurotransmitter release. The density of synaptic vesicles, their interconnectivity and tethering to the membrane are crucial indicators for synaptic vesicle release. We found the distribution of proximal synaptic vesicles to be largely unaffected by the alteration of α-Synuclein levels. Only in the case of α-Synuclein overexpression on a wildtype background, there is a slight reduction of proximal vesicles per $1\mu m^2$ AZ-surface[4] (see fig. 6.3, B).

The mean minimal distance of proximal vesicles to the active zone is unaltered among the genotypes. However, it strongly depends on whether the vesicle is tethered to the membrane or not (see fig. 6.3, C, D). In a healthy chemical synapse, vesicles are pulled towards the active zone membrane to undergo fusion and neurotransmitter release. Therefore the dependence on tethering already indicates that no genotypes suffer from major neurotransmitter release defects. Interestingly, in mice overexpressing the A30P mutation, we find a unique dependence of the distance to the active zone on the connectivity of proximal vesicles. Vesicles connected to other vesicles are significantly closer to the AZ compared to WT synapses and compared to unconnected vesicles[5] (fig. 6.3, E). This indicates that lipid binding of α-Synuclein influences vesicle distance to the active zone.

---

[4]WT : 98.05 ±14.7; αOX: 64.56 ± 11.5, mean ± sem, p=0.1, Student's t-test

[5]connected: WT: 9.89 ± 1.07; A30P: 7.94 ± 0.40, p < 0.01, Student's t-test; not connected: A30P: 10.40 ± 1.59, p<0.05, Student's t-test
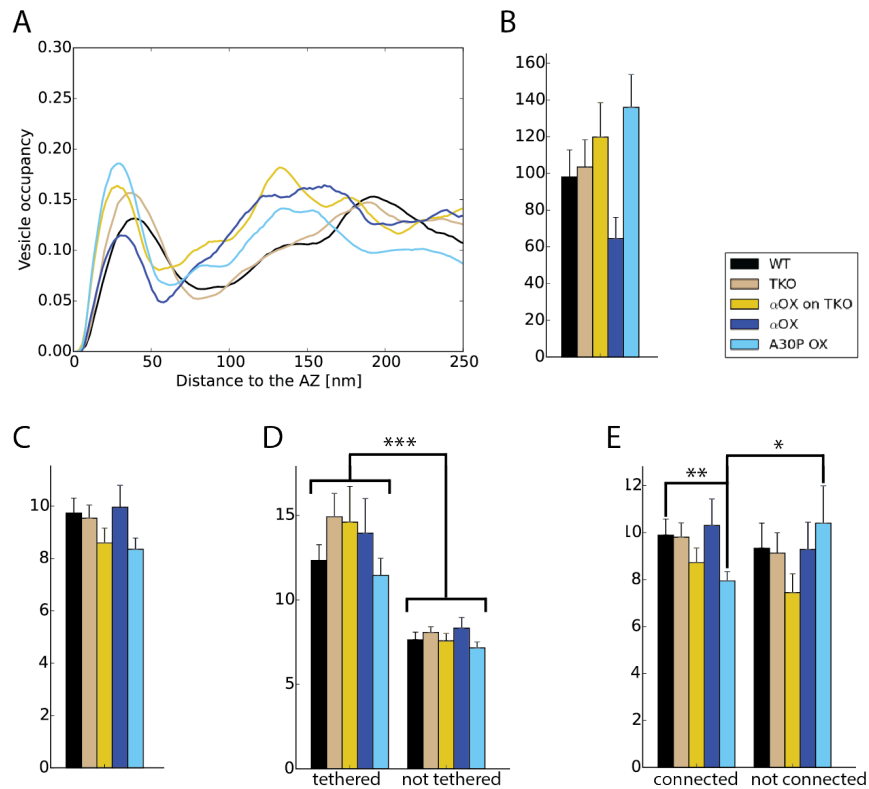
Figure 6.3: Morphology of α-Synuclein mutant synapses. **A**: Mean synaptic vesicle occupancy, averaged over all synapses of each genotype in dependance of the distance to the active zone (AZ). **B**: Amount of synaptic vesicles per 1 µm^2 AZ membrane surface. **C**: Mean minimal distance of synaptic vesicles to the AZ. **D**: Mean minimal distance of synaptic vesicles to the AZ in dependence of tethering. For all genotypes tethered vesicles are significantly closer to the AZ than vesicles that are not tethered ($p < 0.005$, Student's t-test). **E**. Mean minimal distance of synaptic vesicles to the AZ in dependence of connectivity. In A30P overexpressing mice connected vesicles are significantly closer to the AZ compared to wild-type ($p < 0.005$, Student's t-test) and compared to vesicles not connected in A30P mice ($p < 0.05$, Student's t-test).

6.4 α-Synuclein is involved in the formation of connectors among synaptic vesicles

Mice lacking all three Synuclein isoforms have less connectors among synaptic vesicles compared to animals with normal Synuclein levels[6]. Additionally, they have less connectors per vesicle compared to wild-type mice[7] (fig. 6.4). All animals that overexpressed α-Synuclein showed an increase in synaptic vesicle connectivity and an increase in the number of connectors pxer synaptic vesicle. Notably, the loss of connectors in the TKO is overcompensated if α-Synuclein is overexpressed in TKO mice. This overcompensation can also be seen in the amount of vesicles that are in the largest cluster of interconnected vesicles. While $31\% \pm 7\%$ (mean $\pm$ sem) of vesicles are in the largest cluster in wildtype, this amount is reduced to $17\% \pm 11\%$ (mean $\pm$ sem, not significant, Kruskal-Wallis test) in TKO and increased to $60\% \pm 6\%$ (mean $\pm$ sem, p<0.01, Kruskal-Wallis test data not shown) if human α-Synuclein is overexpressed on a TKO background. α-Synuclein is therefore involved in the formation of connectors among synaptic vesicles, either by being a constituent of the connectors or by involvement in their formation. Synapsin was proposed to be a major constituent of connectors suggesting a functional overlap with α-Synuclein. Synapsin is up-regulated in α-Synuclein triple-knockout mice, most likely to compensate for the loss of α-Synuclein. Synapsin levels may contribute to the overcompensation of the amount of connectors in α-Synuclein overexpression in TKO mice.

For proximal vesicles, the neither overexpression of α-Synuclein nor removal of Synuclein changed the vesicle connectivity or number of connectors significantly. However, overexpression of α-Synuclein showed a background dependent behavior: We observed an increase in connectivity in synapses from mice overexpressing α-Synuclein on a Synuclein-null background (p < 0.01, fig. 6.4, C) while α-Synuclein overexpression on a WT background only slightly increased connectivity. In α-Synuclein TKO synapses we observed a slight decrease. In order to investigate if Synuclein knockout and α-Synuclein overexpression were independent factors we performed factorial statistical analysis and found a significant interaction (p < 0.05, factorial design ANOVA). This suggests that the connectivity of proximal vesicles depends on the interaction of the α-Synuclein overexpression and the background level of Synucleins.

---

[6]Fraction of connected SVs: WT: 0.75, TKO 0.64, p<0.001, aOX on TKO: 0.86, p<0.001; aOX: 0.79, p<0.05; a30p: 0.81, p<0.001; all tests Chi-square test

[7]WT: 2.17 ± 0.08; TKO: 1.78 ± 0.09, p<0.001; aOX on TKO: 3.14 ± 0.10, p<0.001; aOX: 2.41 ± 0.10, p<0.05; a30p: 2.80 ± 0.09, p<0.001, all values mean $\pm$ sem; Kruskal-Wallis test
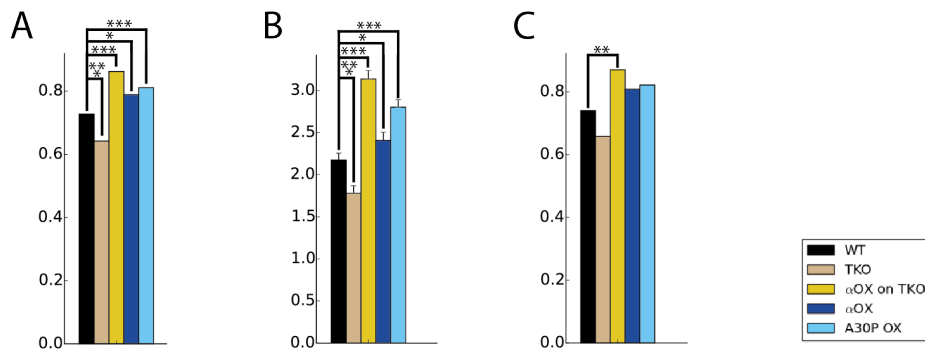
Figure 6.4: Vesicle connectivity in α-Synuclein mutant synapses. **A**: Fraction of total vesicles that are connected to at least one other vesicle. **B**: Average number of connectors per synaptic vesicles. **C**: Fraction of proximal vesicles that are connected.

6.5 α-Synuclein overexpression impedes vesicle tethering and release

Considering the number of vesicles and their distance to the active zone show only small variations among the genotypes, we next investigated how the vesicles are tethered to the membrane of the active zone.

Deletion of all three Synuclein isoforms leads to an increase of tethers formed between synaptic vesicles and the active zone. Tethering is not significantly increased if human α-Synuclein is overexpressed in mice, but in case of the A30P mutant a small increase is observed[8] (fig. 6.5). The amount of tethers follows a similar pattern and is also increased in both TKO systems and in A30P overexpression[9].

The increase in tethering is already a structural indicator of release competence, but to supply the energy necessary to undergo membrane fusion and neurotransmitter release, multiple short tethers have to be formed. Vesicles with more than two connectors constitute the structurally defined readily releasable pool (RRP) [29]. The number of vesicles belonging to the structural RRP is increased in TKO and αOX on TKO synapses[10]. This is a strong indication of elevated release

---

[8]Fraction of tethered SVs: WT: 0.55; TKO: 0.79, p<0.005; α synuclein overexpression on triple-knockout background (αOX on TKO): 0.86, p<0.001; aOX: 0.71, n.s.; A30P: 0.72, p<0.01, Chi-square test

[9]N tethers per proximal SV: WT: 0.98 ± 0.17; TKO: 2.17 ± 0.20, p<0.001; aOX on TKO: 2.80 ± 0.27, p<0.001, aOX: 1.37 ± 0.20, n.s., A30P: 1.92 ± 0.20, p< 0.005, all values mean $\pm$ sem, Kruskal-Wallis test

[10]Fraction of SVs in RRP: WT: 0.125, TKO: 0.357 p<0.005, aOX on TKO: 0.464, p<0.001; aOX: 0.158, n.s.; A30P: 0.311, p<0.05; Chi-square test
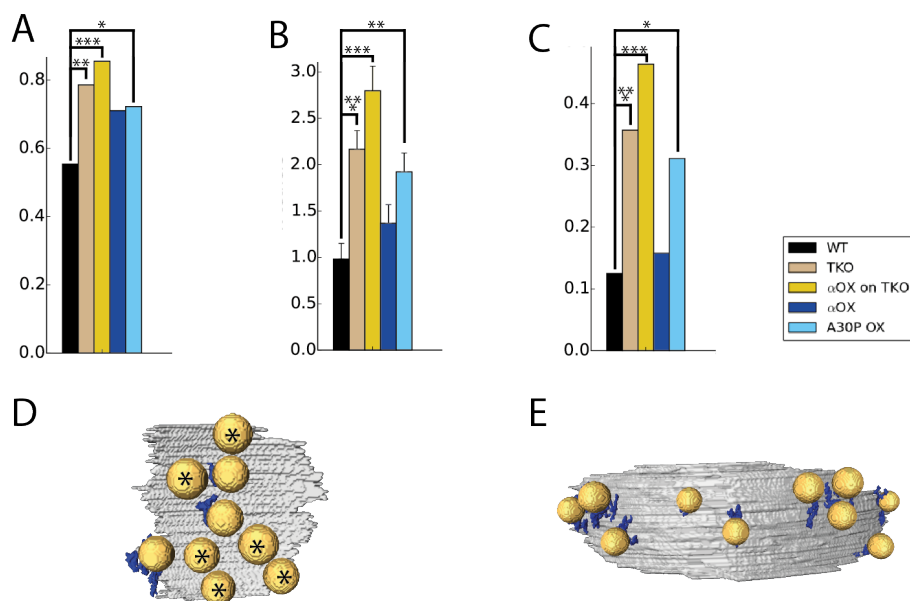
Figure 6.5: Vesicle tethering in dependence of α-Synuclein. **A**: Fraction of vesicles close to the active zone (proximal vesicles) that are tethered. **B**: Average number of tethers per proximal vesicle. **C**: Fraction of proximal vesicles that have more than two tethers, thus constituting the structurally defined RRP. **D, E**: Segmentation of proximal vesicles and tethers in a typical WT (D) and TKO (E) synapse. In WT synapses we find more untethered vesicles (marked by *) compared to TKO synapses.

competence in all α-Synuclein knockout genotypes.

As vesicles are primed for release, they are pulled towards the active zone and form additional tethers. We found no changes in overall tether length in dependence on α-Synuclein. However, in healthy synapses the distance to the active zone correlates with the amount of tethers [29], but a correlation does not exist in case of αOX synapses (see fig. 6.6). This points to a release defect present in mice that overexpress native α-Synuclein. Notably, the correlation is preserved in the A30P mutation, indicating that membrane binding of Synuclein is important for the release defect observed in αOX synapses.

Treatment	r	confidence	slope
WT	-0.38	0.03	-0.18
TKO	-0.41	0.007	-0.24
αOX on TKO	-0.53	0.00	-0.32
αOX	-0.22	0.27	-0.07
A30P OX	-0.41	0.00	-0.26
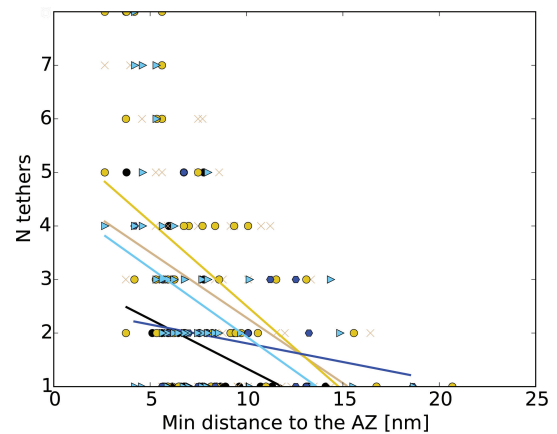
Figure 6.6: Correlation between the proximal vesicle distance to the active zone and the number of tethers.

6.6 The many roles of α-Synuclein

Overall, we observed that overexpression or knockout of α-Synuclein affects the synapse on multiple levels. Immuno-EM on fixed synaptosomes (Karen Vargas, Chandra Lab) showed gold-labeling both at the presynaptic membrane (16.7%) and on synaptic vesicles (74.6% of all gold-labeling).

We find that α-Synuclein contributes to the formation of connectors between synaptic vesicles in synaptosomes, both in the proximal and the distal region up to 250 nm from the active zone. Our finding that the connectivity among synaptic vesicles is decreased in synapses that lack α-Synuclein and increased in all conditions where various forms of α-Synuclein were overexpressed, suggest that both human and mouse α-Synuclein is involved in the formation of connectors. Synapsin is widely believed to be one of the most important proteins involved in connector formation [13] and is upregulated in TKO, likely compensating for the removal of Synuclein. Diao and colleagues showed in an in vitro assay that α-Synuclein can cluster vesicles together with Synaptobrevin/VAMP2 [20] while Nemani and colleagues found that α-Synuclein overexpression inhibits the reclustering of vesicles after release [69]. Together with our data, this suggests that synapsin plays the critical role for reclustering, with α-Synuclein putatively stabilizing the connectors.

α-Synuclein can bind to VAMP2 and promote the assembly of SNARE complexes [10] while at the same time electrophysiological measurements showed reduced level of basal neurotransmission and a lower evoked response after prolonged stimulation in α-Synuclein overexpressing mice [69]. This is supported by our data, showing a

mild release deficiency. In order to fuse with the membrane, multiple short tethers have to be formed between the vesicle and the active zone. In a healthy synapse we therefore find a correlation between the distance of proximal vesicles to the active zone and the amount of tethers that is absent in mice overexpressing human α-Synuclein. This indicates that α-Synuclein may stabilize the initial step of tether formation but inhibit the progression towards priming the vesicle for exocytosis. The A30P mutant does not show the same release defects pointing towards the importance of α-Synuclein's lipid bilayer binding affinity to inhibit priming of the vesicles for exocytosis. Light microscopic studies did indeed show that overexpressing the α-Synuclein A30P mutation variant did not inhibit synaptic vesicle exocytosis [69]. In TKO mice we find more vesicles tethered to the membrane and a higher fraction of vesicles in the readily releasable pool. This indication of an increase in release competence fits well with earlier reports [39]. It may occur due to the increased expression of other proteins involved in the formation of tethers or it may point to an active role of α-Synuclein in regulating release probability.

Chapter 7

SynCAM and the synaptic cleft

This work has been performed together with Geoffrey Kong[1] in collaboration with Thomas Biederer's lab[2] and Tom Blanpied[3]. The results are in published in: "Topographic Mapping of the Synaptic Cleft into Adhesive Nanodomains" [19]

Author contributions:

Karen Perez de Arce: Immuno EM, confocal imaging, STED imaging

Nikolas Schrod: Analysis of cryo-ET data

Sarah Metzbower: STORM

Edward Allgeyer: STED imaging and analyses

Geoffrey Kong: Cryo-ET acquisition

Aihui Tang: Development of 3D STORM analysis

Alexander Krupp: Mice and biochemistry support

Valentin Stein: Supervision of A.K.

Xinran Liu: Support of EM studies

Jörg Bewersdorf: Supervision of E.A.

Thomas A. Blanpied: Design of STORM studies and supervision of S.M. and A.T.

---

[1]Previously MPI for Biochemistry, Martinsried. Present address: Plant Molecular Biology Laboratory, University of Hong Kong, Hong Kong, P.R. China

[2]Department of Neuroscience, Tufts University School of Medicine, Boston, MA, USA

[3]Department of Physiology, Yale University School of Medicine, Baltimore, MD, USA

Vladan Lucic: Design of cryo-ET studies, development of analysis software, supervision of N.S and G.K

Thomas Biederer: Study design, supervision of K.P.d.A. and manuscript preparation

The development of the mammalian brain is a lengthy process with multiple stages. In the initial phase, neurons have to travel to their designated brain areas and form connections to the correct neurons. Both of these processes are regulated by a myriad of proteins.

Among those are Ephrins and their respective Eph receptors (reviewed in [73]). Ephrins are membrane bound extracellular proteins and can be classified into ephrin A and ephrin B families. Members of the Ephrin A family comprise a transmembrane domain, while ephrin B proteins are connected to the membrane via a GPI linker. Ephrin A ligands preferably bind to Eph-A receptors and ephrin B ligands respectively to Eph-B receptors. However, exceptions to the rule do exist.

Eph receptors fall under the large family of receptor tyrosine kinases and can activate a variety of cellular pathways. Apart from this forward signaling, Eph-Ephrin interaction allows reverse signaling which is less understood ([103]).

The interaction of ephrins with their respective receptors usually invokes a repulsive response between the cells but an attractive interaction does happen in some cases. For example, low levels of ephrin can promote attraction while higher levels promote repulsion ([65]). Interstingly, even initial attraction changing into repulsion in a time-dependend manner has been observed ([64]).

Neuroligins, neurexins and SynCAMs on the other hand induce cell adhesion. Neuroligin is a postsynaptic protein that is sufficient to induce the formation of presynaptic sites by binding to the presynaptic protein neurexin ([33]). There are three forms of neuroligin. Neuroligin-1 if found at exitatory synapses, neuroligin-2 at inhibitory synapses and neuroligin-3 at both. All of the neuroligin proteins form homodimers. Dimerization is required to promote synaptogenesis and likely also required to induce presynaptic differentiation via neurexin clustering ([88]). Synaptic plasticity is also influenced by neuroligin. Interestingly, the effect seems to require a difference in neuroligin levels among the cells ([56]).

SynCAM 1, the founding member of the SynCAM superfamily, is a 100 kDa protein consisting of three Ig domains with multiple glycosylation sites that can modulate the adhesion between SynCAM superfamily members [32]. During developmental stages SynCAM proteins make up 0.5% of the total synaptic membrane proteins [81]. The synaptic cleft contains a dense mesh of proteins connecting

Treatment	Synapses
Knockout	8
Knockout control	7
Overexpressor	5
Overexpressor crontrol	5

Table 7.1: Dataset of tomograms used for analysis

the pre- and postsynaptic membrane. Although we know many proteins of the synaptic cleft, their distribution among and especially within synapses is often unknown. We therefore investigated the effects of deletion or overexpression of the synaptic adhesion molecule SynCAM 1 on the synaptic cleft.

7.1 SynCAM shapes the edge of the synaptic cleft

In cryo-electron tomography, the synaptic cleft appears as a dense network of proteins with a complex topology [60]. In cryo-electron micrographs the heavily crowded cleft shows the highest density near the midline, slightly shifted towards the postsynaptic membrane (fig. 7.1B). In order to investigate the influence on SynCAM 1 levels on the morphology of the synaptic cleft and the protein distribution within the cleft we recorded tomograms of vitrified synaptosomes from mice either lacking SynCAM 1 or overexpressing the protein. Our dataset comprised 25 tomograms in total (see table 7.1).

We first surveyed the changes in cleft morphology in SynCAM 1 knockout mice. Deletion of SynCAM 1 does not alter the width of the synaptic cleft. We divided the cleft in four layers, from the postsynaptic to the presynaptic membrane (see fig 7.1 C, top). It is important to note that in cryo-electron tomograms absolute greyscale values cannot be compared without normalizing them first because during reconstruction, the mean of the greyscale values of the resulting tomogram is set to a predefined value. We therefore used the density of the membrane and the average density of the synaptic cleft to normalize our data. Averaging the greyscale values of each layer for a synapse and then combining all synapses of each genotype didn't yield a distinctive phenotype. However, when we further separated the cleft region into columns (see fig. 7.1 C, bottom) we found that in SynCAM 1 Ko mice, the outermost column contains less protein than than the inner columns, while WT mice showed the opposite behavior (fig. 7.1 F).

Applying the same method to investigate the effects of SynCAM 1 overexpression we found no significant increase in overall protein density in the outermost column. The cleft profile was well preserved in case of SynCAM 1 KO (fig. 7.1 E), with the highest protein density in layer 2. In contrast, overexpression of SynCAM 1 obliterates the density difference between layers 1 and 2 in the whole cleft and in particular in the outermost column (fig. 7.1 I, J).

Immuno-EM of high-pressure frozen sections of the CA1 hippocampus region from adult mice done by our collaborators confirmed that SynCAM 1 localizes towards the outer edge of the cleft. SynCAM 1 was found mostly on the postsynaptic membrane ($46 \pm 6\%$ of total synaptic labeling). In sections from SynCAM 1 KO mice, labeling was reduced by $84 \pm 4\%$, confirming the specificity of the antibody. Less labeling was found towards the center of the cleft, the post-synaptic cytomatrix, and at the presynaptic membrane. When the radius of the cleft is normalized, quantification of the location of labeled postsynaptic SynCAM 1 showed a distinct peak towards the edge of the PSD (normalized to 1 in fig 7.2 B).

7.2   SynCAM 1 and Eph-B2 localize to distinct areas within the synaptic cleft

Fluroescently labeled HOMER can be used to define the area of the PSD [62]. In addition to investigating the the location of fluorescently labeled SynCAM 1 relative to the area defined by HOMER labeling, our collaborators also looked at the location of a second protein present in the cleft of excitatory synapses: The tyrosine kinase receptor Eph-B2[4]. $74 \pm 9\%$ of HOMER puncta contained either SynCAM 1, Eph-B2 or both. $88 \pm 1\%$ of SynCAM1 puncta colocalized with Eph-B2 and all of the Eph-B2 puncta showed a SynCAM 1 signal. Going from conventional confocal microscopy to STED microscopy, it becomes apparent that SynCAM 1 localizes towards the edge of the area defined by the HOMER labelling, while Eph-B2 puncta are localized deeper within the HOMER labeled region (see fig 7.2, C, D).

3D-STORM [46, 96] was used to further investigate the three-dimensional subsynaptic distribution of SynCAM 1. 79% of synapses with HOMER labeling showed SynCAM staining within 500nm of the PSD border and SynCAM 1 puncta show a strong peak between 100 nm and 200 nm from the PSD border. Again, simultaneous Eph-B2 staining showed a different distribution further away form the PSD border and more towards the center of the synapse. 3D-STORM also enables

---

[4]An introduction to Eph receptors and Ephrins, their ligands, can be found in chapter 4.2

the quantificication of the area of SynCAM 1 and HOMER puncta. SynCAM 1 puncta likely consisting of multiple Syncam 1 molecules seem to label a specific subpopulation of synapses: The volume of HOMER clusters colocalizing with such SynCAM 1 clusters was almost twofold the volume of HOMER clusters colocalizing with no or small SynCAM 1 puncta ($13.1 \pm 2.3 \cdot 10^6$ nm^3 and $7.2 \pm 0.8 \cdot 10^6$ nm^3).

SynCAM 1 promotes the number of excitatory synapses [7, 31]. It is therefore conceivable that the distribution of SynCAM 1 can be altered by synapse activity. Indeed, application of a long term depression (LTD) inducing protocol and subsequent immunolabeling for SynCAM 1 and PSD-95 showed an increase in the area of SynCAM 1 puncta by $27 \pm 5\%$.

7.3 Discussion

It was shown previously that the cleft consists of a filamentous network [60]. However, the composition of the cleft and the distribution of proteins within the cleft were still unknown. Cryo-electron tomography revealed that SynCAM 1 knockout leads to a loss of protein in the outer cleft region and in mice overexpressing SynCAM 1, the typical density profile of the protein mesh within the cleft was abolished in the same cleft region at the edge of the cleft. Together, this points to a distinct subsynaptic distribution of SynCAM 1 towards the edge of the synaptic cleft. Although no complete structure of SynCAM 1 exists, the suggested tertiary structure of three equally sized extracellular lg domains likely masks the increased protein density in layer 2 of the cleft present in all genotypes except SynCAM 1 overexpressor. The distinct density profile of the synaptic cleft is therefore likely shaped by other proteins. A strong candidate would be Neuroligin, a postsynaptic membrane protein that binds to the presynaptic Neurexin. They form a density closer to Neuroligin [93, 101] and may be the main contributors to the central density we observe.

The localization of SynCAM 1 towards the edge of the synaptic cleft was confirmed in immunolabeling experiments in high-pressure frozen hippocampal sections and is consistent with the shortened PSDs and active zones in SynCAM 1 knockout mice [81].

Eph-B2 and SynCAM 1 localize to distinct areas in the cleft as shown by immunofluorescence. It is conceivable that Eph-B2 acts earlier in synaptogenesis while SynCAM 1 is needed to stabilize and maintain the synapse. The location towards the edge of the cleft and the known involvement in the regulation of

synaptic strength supports possibility of SynCAM 1 actively or passively recruiting proteins to the cleft.

Taken together, the three complementary techniques used in this study could show that SynCAM 1 and EphB2, and possibly other synaptic adhesion molecules localize to different areas within the synaptic cleft. The dense filamentous network in the cleft is therefore likely organized in molecular subdomains with distinct origin and function.
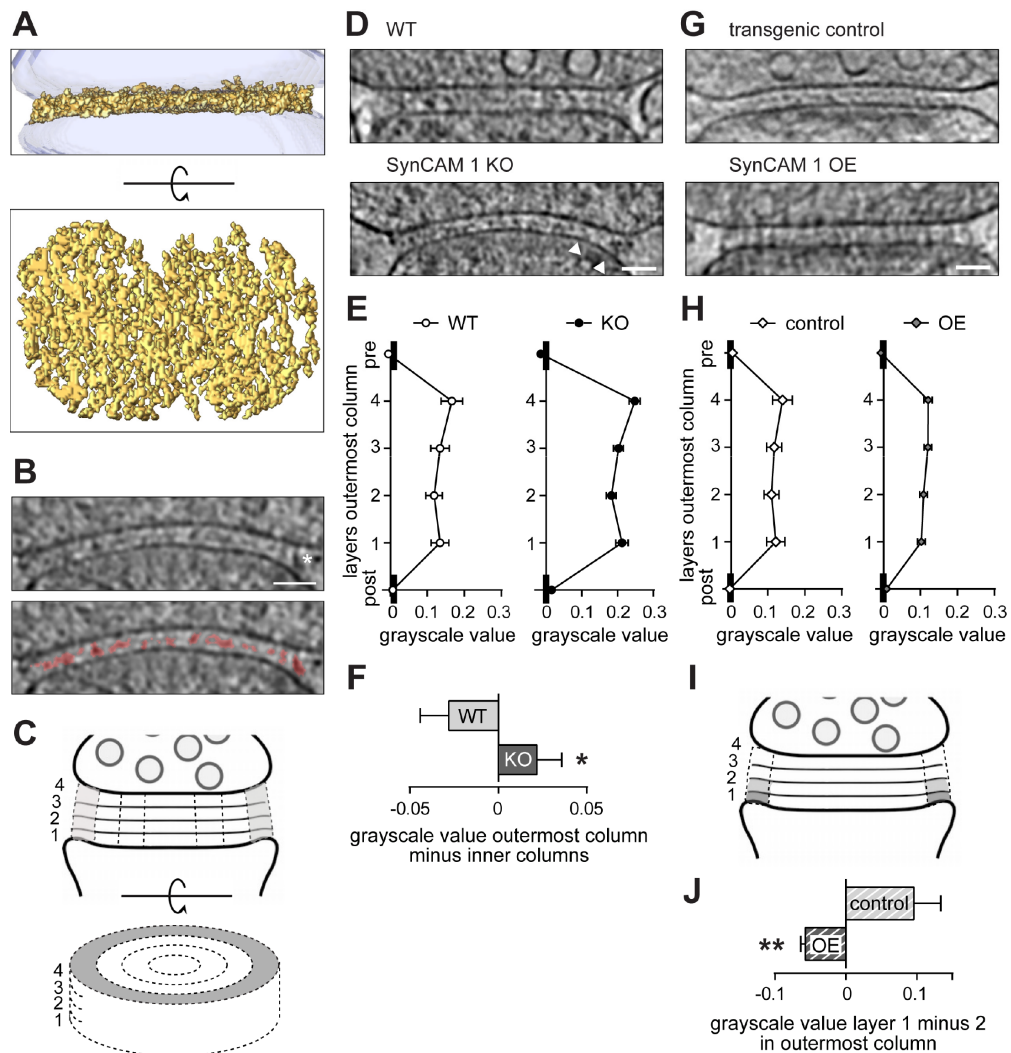
Figure 7.1: A: Top and sideview of a synaptic cleft segmented at a fixed greyscale value. **B**: Top: Tomographic slice depicting the synaptic cleft. Bottom: central density visualized by applying a threshold filter. **C**: Definition of cleft layers 1-4 from post- to presynaptic side and four concentric columns within the cleft. Dashed lines mark the columns. The outermost column is shown in grey. **D**: Representative cleft images from WT and SynCAM 1 KO synaptosomes. The less densely populated region towards the edge of the cleft is marked by arrowheads. **E**: Cleft density profile. Greyscale values of the four layers of the synaptic cleft in the outermost column, averaged over all synapses of each genotype. **F**: SynCAM 1 KO synapses have a higher grayscale value differential and hence lower relative protein density in the outermost column compared to the three central columns. For normalization, cleft mean was set to 1 while membrane mean was kept at 0. **G**: Representative cleft images from tomograms of WT (top) and SynCAM 1 overexpressor (OX) (bottom) synaptosomes. The elevated central cleft density of the control is barely visible in OX synapses. **H**: Flat cleft density profile of SynCAM 1 OX synaptosomes. Greyscale values across the four layers of the outermost cleft column are shown. Mean values of individual layers were calculated as in (E) for control (left) and OX synapses (right). **I, J**: Layer differences in were determined by subtracting grayscale values of volumes depicted in lighter gray from darker gray volumes. SynCAM 1 OX synapses have higher density in layer 2 relative to layer 1 in the outermost cleft column compared to controls. Normalization as in (F) (N=5 synapses each). Tomograms in (B), (D) and (G) are shown at a depth of 4 voxels (9.2 nm), scalebars 50 nm. Modified from [19]
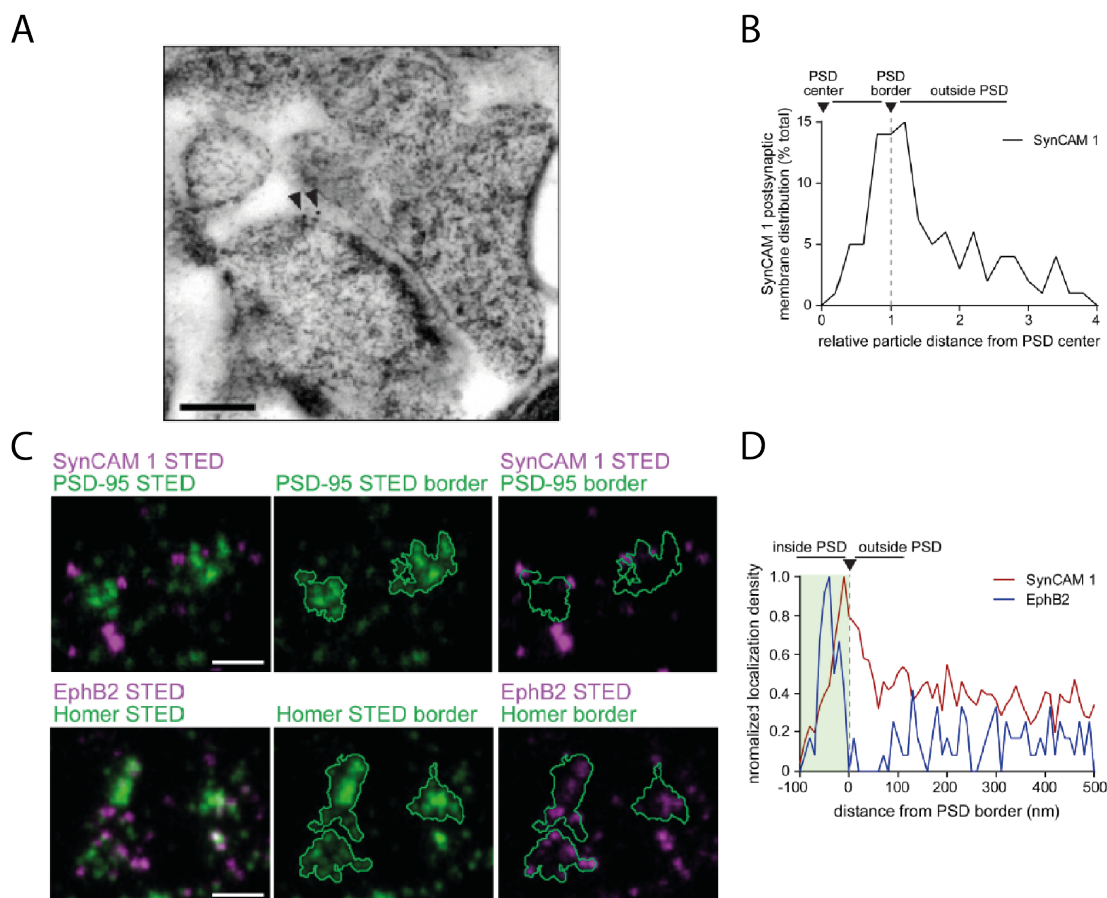
Figure 7.2: **A**: Immuno-EM of SynCAM 1 in high pressure frozen sections of the adult hippocampal CA1 region. Arrowheads indicate immunogold-labeled SynCAM 1 on the postsynaptic membrane at the edge of the cleft. **B**: Postsynaptic SynCAM 1 distribution. Distance of gold-labeled SynCAM 1s to the PSD center were measured, normalized to 1 corresponding to the PSD radius (N=97 micrographs, 3 mice). **C**: Dissociated hippocampal neurons at 14 div were subjected to sequential immunostaining for (upper row) surface SynCAM 1 (magenta) and PSD-95 (green) or (lower row) surface EphB2 (magenta) and Homer (green), and imaged by 2-channel STED microscopy. PSD borders calculated based on STED localizations are shown in the center and right panels. Scalebars 400 nm. **D**: Surface SynCAM 1 and EphB2 localizations were determined in STED images as in (C) and distances were measured from the PSD border defined by PSD-95 and Homer localizations, respectively. SynCAM 1 localization density (red) reached a maximum at the border of the PSD (green). SynCAM 1 localizations within the PSD were rare. EphB2 (blue) exhibited the most prominent localizations within the PSD and a minor peak at the border. Localization densities were normalized to the highest value. SynCAM 1 data were from 696 PSDs in 86 imaging fields and EphB2 data from 111 PSDs in 10 fields. Modified from [19]

Chapter 8

Materials and Methods

8.1 Neuronal cultures

Hippocampal neuronal cultures were prepared as described previously [3, 49]. In short, hippocampal neuronal cultures were prepared from E18 rat embryos or P0-P2 newborn rat pups. Animals were decapitated. The whole brain was extracted and moved to ice-cold calcium and magnesium free HBSS (CMF-HBSS, Invitrogen, 14185-052) buffer containing 5 mM HEPES (Invitrogen, 15630-080). The same buffer was used for all further steps, unless otherwise denoted. After removal of the meninges the hippocampi were dissected and transferred to pre-warmed buffer containing 0.25% trypsin (Invitrogen, 25300-054). After 20 min in a 37° waterbath the trypsin was removed by washing three times with ice-cold buffer, with 5 min rest at room temperature in between washing steps.

Cells were dissociated with a normal Pasteur pipette (10 - 15 times) followed by a Pasteur pipette fire polished to half the diameter. After trituration, cells are passed through a 70 μm cell strainer before cell counting.

Grids were coated overnight in poly-L-Lysine solution and washed twice with autoclaved MilliQ water for 2-3 hours each. Grids were immersed in culturing medium at least one hour before plating and stored in the incubator at 37° and 7% CO_2.

Cell were plated with a density of $2.5 \cdot 10^5$ cells per 35 mm dish in neuronal plating medium (MEM with Earl's salt and L-glutamine (Invitrogen, 11095-080) containing 0.6% wt/vol Glucose (Sigma, G8769) and 5% FBS (Gibco, 10082139)). After 5 hours medium was changed to either B27 supplemented medium or pre-conditioned neuronal maintenance medium.

B27 supplemented medium [9] was prepared with Neurobasal (Invitrogen 21103-049) supplemented with GlutaMAX (Invitrogen 35050-061) and B27 serum free supplement (Invitrogen 17504-044).

Glial cultures were prepared from P1 rat embryos as described in [49]. After decapitation the whole brain was extracted and meninges were carefully removed. The cerebral hemispheres from 2 - 3 animals were isolated, collected and cut into small pieces using a scalpel before being transfered into CMF-HBSS containing 0.25% trypsin and 1% DNAse I. The cells were incubated in a 37°C waterbath for 5 minutes, swirling the tube occasionally. After trituration with a 10 ml pipette (10 - 15 times), the solution was returned to the waterbath for another 10 minutes before the final trituration using a 5 ml pipette (10 - 15 times). Cells were centrifuged for 7 minutes at 120 g in order to remove enzymes and lysed cells. Afterwards they were filtered through a 70 µm cell strainer. Cell density was determined using a hemacytometer and $7.5 \cdot 10^6$ cells were plated per 75 cm^2 flask. When $\sim$ 70% - 80% confluence was reached, cells were harvested by changing the medium to trypsin/EDTA. After a short incubation (~3-5 min), cells were collected and centrifuged at 120 g for 7 min. Cells were afterwards plated at a density of $7.5 \cdot 10^6$ cells per 75 cm^2 flask. In order to generate preconditioned medium, glial medium was exchanged to neuronal maintenance medium (MEM with Earl's salt and L-glutamine (Invitrogen, 11095-080) containing 0.6% wt/vol Glucose (Sigma, G8769) and N2 supplement (Sigma 17502-048)) after the glial cultures reached $\sim$ 70% - 80% confluence. After 15 - 20 hours, medium was harvested and used for hippocampal neuronal cultures.

Neuronal cultures were grown in the incubator at 37°, 7% CO_2. Most cultures were frozen at day in vitro (DIV) 9, during the time of strong synaptogenesis [38]. It has been reported, that neurons show distinct cytoplasmic transport packages at DIV 7 [1, 21]. To give the neurons more time for synaptogenesis, we also froze cultures at DIV 14.

8.2   Transfection and immunostaining

Transfection with Lipofectamine   Briefly, the medium was replaced with fresh Neurobasal (Gibco, Invitrogen, Carlsbad, CA, USA) containing 2% B27 (Invitrogen) supplement and 2mM Glutamin (Invitrogen). The old medium was stored in the incubator. Per dish 50µl Optimem with 2% Lipofectamine (v/v) and 2% DNA (w/v) was added. After pipetting the medium twice to mix it, the sample was incubated for one hour. Afterwards cultures were washed with Neurobasal before reapplying the old medium.

FM staining Cells were stained either with a styryl dye (FM1-43 or FM4-64, Invitrogen, [15]). All buffers were prewarmed to 37°C. After replacement of the culturing medium with HBSS, cells were allowed to rest for about 10 to 20 minutes. Afterwards, cells were first washed again with HBSS, followed by application of 10µM FM1-43 and 100mM KCl in HBSS. After two minutes, residual flurophores were removed by washing with 10ml HBSS.

Co-staining of synaptotagmin. For staining with the synaptotagmin antibody (Synaptic Systems, Cat. No. 105 311C3) and QD605, cells were incubated with the antibody for one hour prior to FM1-43 staining. After FM1-43 staining cells were incubated with the secondary antibody for one hour. Afterwards the cells were washed with 10ml HBSS.

8.3 Synaptosome preparation

Synaptosomes were prepared from six to eight week old mice as described in [23]. Briefly, animals were sacrificed by cervical dislocation and then decapitated. The cerebral cortex was removed and placed in ice-cold homogenization buffer (HB: 0.32 M sucrose, 50 mM EDTA, pH 7.4 with cOmplete Mini EDTA-free, Roche; 7 tablets in 70 ml HB). After removal of white matter and blood vessels, the cortex was submerged in 3 ml HB and homogenized at up to 700 rpm in a teflon-glass homogenizer. The homogenate was centrifuged for two minutes at 2000 g to remove large debris and unbroken cells and the supernatant was centrifuged at 9500 g for 12 minutes. The pellet containing the synaptosomes was further purified by a Percoll (GE Healthcare) gradient (3%, 10%, 23%). The fraction between 10% and 23% was collected and diluted in Ca^2+-free Hepes buffered medium (140 mM NaCl, 5 mM KCl, 5 mM $NaHCO_3$, 1.2 mM $Na_2HPO_4$4, 1 mM $MgCl_2$, 10 mM glucose, 10 mM Hepes, pH 7.4). Percoll was reomved by centrifugation at 22000 g for 10 min and resuspension in HMB supplemented with 1.12 mM $CaCl_2$.

8.4 Plunge-freezing

Cultures Cultures were plunged with a manual plunger. Single dishes with up to four grids were moved from the incubator to the plunger. Individual grids were fixed in the plunger using Dumont negative action tweezer. 4 µl of pre-mixed gold fiducials (10 nm and 15 nm beads, concentrated 5-10x from stock solution) were added to the grid while mounted in the plunger. Depending on the amount of

liquid retained on the grid after removal from the dish, the blotting time had to be adjusted by feel. Typical blotting times were 4-7 seconds.

After plungefreezing, grids were inserted into Autogrids (FEI, The Netherlands) using a transfer chamber developed in the department.

Synaptosomes   Plunge-freezing of synaptosomes was performed as previously described ([29]). Part of the dataset was plunged using an automated plunger (Vitrobot, FEI).

8.5   Correlative microscopy

Cryo-light microscopy (cryo-LM) was carried out using the Cryostage[2] [79] (see fig. 8.1) mounted on a Zeiss Axiovert 200M light microscope and connected to a liquid nitrogen pump (Norhof LN2 Microdosing system, Series #900, Maarsen, The Netherlands). The stage was cooled for an additional 15 min after the temperature stabilized at -186°. Images were acquired using the Zeiss Axiovision software. The MosaiX and Z-stack modules were used to produce maps of the entire grid. Phase contrast maps and fluroescent maps were acquired seqentially to speed up the process. Whole grid maps were acquired using a 20x Ph2 objective (numerical aperture 0.4) and selected regions were additionally imaged with a 63x Ph2 objective (numerical aperture 0.75).
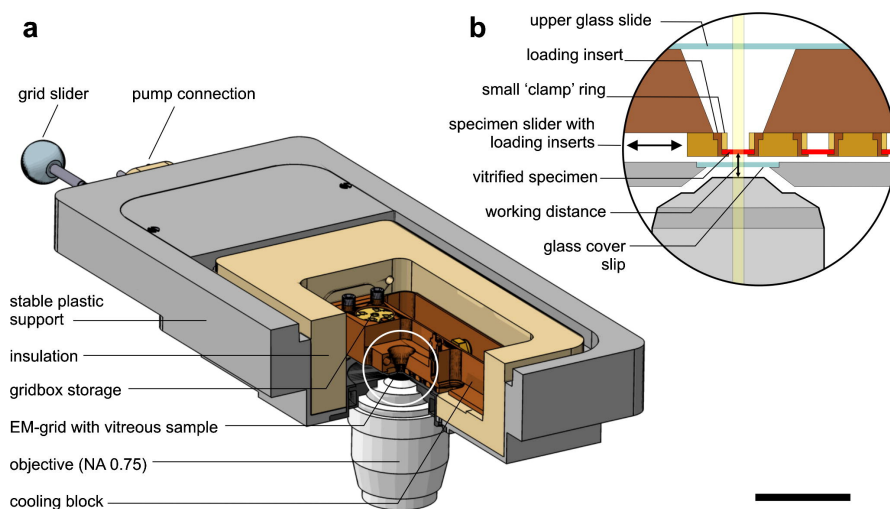
Figure 8.1: a) Cut-away view of the Cryostage[2]. b) Magnified view of white circle in a). Scalebar 40 mm. Inset not drawn to scale. From [79])
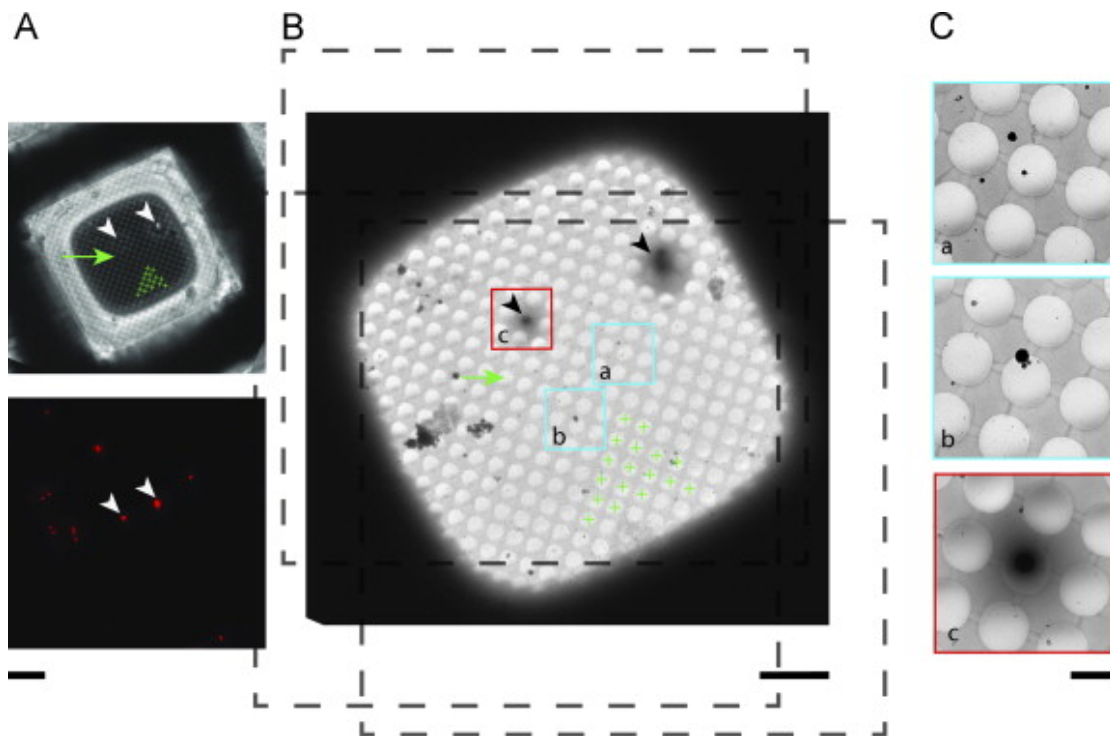
Figure 8.2: Correlation between light and electron microscopy. **A**: Cryo-phasecontrast and cryo-fluoresence image of a grid containing 1 µm fluorescent beads. Scalebar: 20 µm. **B**: EM overview image. Dashed lines illustrate how the overview images were shifted in the 'move overview' mode. Scalebar: 10 µm. **C**: Top and middle: search images corresponding to the blue squares in (B) used for the 'move search' mode. Bottom: Correlated location of fluorescent bead from (A, bottom). Scalebar: 2 µm

Due to grid bending, z-stacks spanning more than 60 *µm* were common. To facilitate navigation, a maximum intensity z-projection was created in ImageJ.

Upon loading the grid in the electron microscope, a map of the entire grid was acquired at low magnification (170x - 250x) using the TOM Acquisition package [52]. If a region of interest identified in the cryo-LM images was suitable for imaging in the electron microscope, the correlation was performed for this region.

ImageJ and a Python script developed by Vladan Lucic [59] were used for the correlation. The correlation was carried out in two steps. First the correlation between a low magnification image in the electron microscope (EM-overview image) and the light microscopy image (LM image) is established. Afterwards, a correlation between the EM-overview image and the stage coordinates of the electron microscope is established.

The correlation between the LM images and the EM overview image can be done in two ways. One possibility is to use landmarks visible in both images, for cracks in the carbon film or contamination. Grid bars can also be used but are less ideal as they are obfuscated by the ice in the EM-overview image. For the second method, a pattern composed of holes in the carbon support film is marked in the EM-overview image and in the LM image. This pattern is used to calculate the rotation, magnification change and possible shearing between the images. An additional single spot is then used to calculate the translation. This method is not as precise as the first one, due to the calculation of the translation by only one spot. However, this is sometimes necessary if not enough landmarks can be identified or the landmarks have not been preserved in light and electron microscopy images.

Next, a correlation between the EM-overview image and the physical stage coordinates has to be established. Currently, two methods are implemented for that purpose: In the 'move search' mode, the coordinates of landmarks in the EM-overview image are used to establish a direct correlation. In a second method the stage is shifted and additional EM-overview images are taken. The correlation between the EM-overview image and the stage coordinates of the microscope is then determined using the shifts and the corresponding pixel shifts of one landmark in the EM-overview images.

For the actual correlation, a position of an object of interest in a LM image was used to calculate the corresponding position in the EM stage coordinate system. In some cases the correlation proceeded in the opposite direction, namely to use the EM stage coordinates where a tomogram was recorded in order to calculate its position in the LM image.

8.6 Electron Tomography

Tomograms were acquired using a FEI Tecnai CM300 microscope or one of two FEI Tecnai G2 Polara microscopes, all equipped with an FEG and an energy filter. The FEI tomography software was used during acquisition. For α-Synuclein studies the magnification was chosen to correspond to a object pixel size of 0.47 nm. For neuronal cultures a object pixel size of ~0.8 nm was used for most tomograms. The area used for focus adjustment and tracking was shifted by $\approx 5\mu m$ along the tilt axis. Tracking after image acquisition was sufficient in most cases.

Tomograms at the earlier stages of the project were acquired using two half series starting from $0°$ to the negative and positive maximum angles ($\sim \pm65°$). Later this scheme was changed to two series, one starting from $-40°$ to the maximum

positive angle and the second one from $-40°$ to the maximum negative angle. The angular increment was set to either $1.5°$ or $2°$. For the synuclein project the applied defocus was -7 µm. For tomography of neuronal processes a defocus between -8 µm and -12 µm was applied.

8.7 Reconstruction and postprocessing

Tomograms were mostly reconstructed using the TOM package in Matlab [70]. Some tomograms from neuronal cultures were reconstructed with the Imod reconstruction package ETOMO [53].

In TOM, fiducial gold markers were manually tracked. Bad gold fiducials were removed if a sufficient amount of markers was available so that an error between one and two pixels was achieved for most tomograms.

A weighted back projection (WBP) algorithm was used for reconstruction. For the analysis, an analytical WBP approach was used. To facilitate segmentation, we additionally generated a reconstruction using an exact WBP algorithm with an 800 pixels setting for specimen thickness. That way, low frequencies, such as membranes, were enhanced in the reconstruction.

To improve downstream computation times, tomograms were cropped in all three dimensions to contain only relevant parts. Cropping was performed using a small script for EM package [41].

To reduce the noise in tomograms while preserving the signal as good as possible, anistotropic nonlinear diffusion (AND, [27, 28]) was used. Parameters and denoising steps were chosen to achieve best preservance of the signal and not strong noise reduction.

8.8 Statistical Analysis of synaptosomes and presynaptic boutons

In synaptosomes tomograms were binned 4x, yielding a final pixel size of 1.87 to 1.88 nm, depending on the microscope. The active zone, the synaptic vesicle median disc and the area of analysis were manually segmented in Amira (Visualization Sciences Group). In varicosities the is no defined active zone. There the entire membrane, microtubules, smooth endoplasmic reticulum, mitochondria and other organelles were segmented in addition.

Tethers and connectors were detected using the Pyto package (a software package written in Python), combining the watershed transform with connectivity based segmentation [29]. Analysis of synaptic vesicle size and distribution, their tether and connectors was all carried out using the Pyto package. For both datasets, the confidence tests used in analysis were Student's t-test for Gaussian distributed values, Kruskal-Wallis test for values not following a normal distribution and Chi-square test for values in discrete bins. Pearson's coefficient and t-test were used for correlation analysis. In all graphs, confidence values are indicated as: * : $p < 0.05$; ** : $p < 0.01$; *** : $p < 0.001$.

For all Synuclein projects, data acquisition and analysis was performed blind of condition.

Dense core vesicle profiles were created with ImageJ, using the Radial Profile Plot plugin (http://rsb.info.nih.gov/ij/plugins/radial-profile.html). A circle with the same center as the median disc of the DCV is marked in the tomogram. The radius of the circle is chosen to be at least 5 pixels larger than the radius of the DCV. The plugin is then used to average the pixel values along concentric circles. For figures or in cases where the resulting graph was not clear the slice of the tomogram used was first interpolated to 5x size, improving the formation of averages along concentric circles.

Acronyms and abbreviations

AZ   active zone

cryo-EM   cryo-electron microscopy

cryo-ET   cryo-electron tomography

CCD   charge coupled device

CLEM   correlative light- and electron microscopy

CTF   contrast transfer function

DCV   dense core vesicle

DIV   days *in vitro*

EM   electron microscopy

ET   electron tomography

FEG   field emission gun

FIB   focused ion beam

LM   light microscopy

MTF   modulation transfer function

MVB   multi-vesicular body

PTV   Piccolo/Bassoon transport vesicle

RRP   readily releasable pool

sER   smooth endoplasmic reticulum

SNARE   soluble NSF-attachment protein receptor

SNAP25   synaptosomal associated protein, 25kDa

SNR	signal to noise ratio
SPA	single particle analysis
SV	synaptic vesicle
TKO	triple-knockout
α**OX**	α synuclein overexpression
α**OX on TKO**	α synuclein overexpression on triple-knockout background
VAMP2	vesicle associated membrane protein 2 , also called synaptobrevin
WBP	weighted back projection
WT	wild-type
t-test	Student's t-test, used for Gaussian distributed values
KWT	Kruskal-Wallis test, used for values not following a normal distribution
Chi^2	Chi-square test, used for values in discreet bins

Acknowledgments

At this point I would like to thank the people who have made this work possible.

Firstly, I would like to thank Professor Baumeister for giving me the opportunity to work in the department of structural biology. This allowed me to not only to use the state of the art equipment but to work with great colleagues over the years.

I also want to thank Vladan Lucic, my direct supervisor, for his support and guidance during all my studies and ventures. It was pleasure working with you - and skiing with you as well.

A warm thank you goes to the members of the neurons group: Uli, Shoh, Fuku, Zdravko, Dimitri and Antonio. Thank you for your help in the lab, the many discussions and all the fun in and outside of the lab.

Professor Júrgen Plitzko's and Günter Pfeiffer's help with the electron microscopy was invaluable. Thank you for the support during day and night time.

I also want to thank all the technical staff who keep everything running smoothly: Inga for the computer support and the workshop for repairs and producing all kinds of nifty tools. A special thank you goes to Tim for great ideas, small and big, as well as numerous ad-hoc repairs.

My family has always supported me and made me the person I am today. I will always be grateful to both my parents and sisters. Thank you all for always being there for me.

And lastly, but most importantly, I want to thank my wife Alexa for her eternal patience. You always had my back no matter how sleep-deprived or stressed we have been. I am proud of our little family and you are the joy of my life.

Bibliography

[1] Ahmari, S. E., Buchanan, J., and Smith, S. J. (2000). Assembly of presynaptic active zones from cytoplasmic transport packets. *Nature neuroscience*, 3:445.

[2] Bammes, B., Rochat, R., Jakana, J., Chen, D.-H., and Chiu, W. (2012). Direct electron detection yields cryo-em reconstructions at resolutions beyond 3/4 nyquist frequency. *Journal of structural biology*, 177(3):589–601.

[3] Banker, G. A. and Cowan, W. M. (1979). Further observations on hippocampal neurons in dispersed cell culture. *Journal of comparative neurology*, 187(3):469–493.

[4] Bartels, T., Choi, J. G., and Selkoe, D. J. (2011). α-synuclein occurs physiologically as a helically folded tetramer that resists aggregation. *Nature*, 477(7362):107–10.

[5] Bartheld, C. V. and Altick, A. (2011). Multivesicular bodies in neurons: distribution, protein content, and trafficking functions. *Progress in Neurobiology*, 93(3):313–340.

[6] Bell, M., Bourne, J., Chirillo, M., Mendenhall, J., Kuwajima, M., and Harris, K. (2014). Dynamics of nascent and active zone ultrastructure as synapses enlarge during long-term potentiation in mature hippocampus. *Journal of comparative neurology*, 522(17):3861–84.

[7] Biederer, T., Sara, Y., Mozhayeva, M., Atasoy, D., Liu, X., Kavalali, E., and Südhof, T. (2002). Syncam, a synaptic adhesion molecule that drives synapse assembly. *Science*, 297(5586):1525–31.

[8] Bodian, D. (1970). An electron microscopic characterization of classes of synaptic vesicles by means of controlled aldehyde fixation. *The Journal of cell biology*, 44(1):115–24.

[9] Brewer, G. and Torricelli, J. (2007). Isolation and culture of adult neurons and neurospheres. *Nature protocols*, 2(6):1490–1498.

[10] Burré, J., Sharma, M., Tsetsenis, T., Buchman, V., Etherton, M., and Sdhof, T. (2010). Alpha-synuclein promotes snare-complex assembly in vivo and in vitro. *Science*, 329(5999):1663–1667.

[11] Cabin, D., Shimazu, K., Murphy, D., Cole, N., Gottschalk, W., McIlwain, K., Orrison, B., Chen, A., Ellis, C., Paylor, R., Lu, B., and Nussbaum, R. (2002). Synaptic vesicle depletion correlates with attenuated synaptic responses to prolonged repetitive stimulation in mice lacking alpha-synuclein. *The Journal of neuroscience*, 22(20):8797–807.

[12] Chen, S.-Y. and Cheng, H.-J. (2009). Functions of axon guidance molecules in synapse formation. *Current Opinion in Neurobiology*, 19(5):471–478.

[13] Chi, P., Greengard, P., and Ryan, T. (2003). Synaptic vesicle mobilization is regulated by distinct synapsin i phosphorylation pathways at different frequencies. *Neuron*, 38(1):69–78.

[14] Cooper, I. S. (1953). Ligation of the anterior choroidal artery for involuntary movements; parkinsonism. *Psychiatric quarterly*, 27(2):317–9.

[15] Cousin, M. A. (2008). Use of fm1-43 and other derivatives to investigate neuronal function. *Current protocols in neuroscience / editorial board, Jacqueline N.Crawley ...[et al.]*, Chapter 2:Unit 2.6.

[16] Craig, A., Graf, E., and Linhoff, M. (2006). How to build a central synapse: clues from cell culture. *Trends in Neurosciences*, 29(1):8–20.

[17] Crowther, R. A. (1971). Procedures for three-dimensional reconstruction of spherical viruses by fourier synthesis from electron micrographs. *Philosophical transactions - Royal Society. Biological sciences*, 261(837):221–230.

[18] Dalby, B., Cates, S., Harris, A., Ohki, E., Tilkins, M., Price, P., and Ciccarone, V. (2004). Advanced transfection with lipofectamine 2000 reagent: primary neurons, sirna, and high-throughput applications. *Methods*, 33(2):95–103.

[19] de Arce, K. P., Schrod, N., Metzbower, S. W. R., Allgeyer, E., Kong, G. K.-W., Tang, A.-H., Krupp, A., Stein, V., Liu, X., Bewersdorf, J., Blanpied, T., Lucic, V., and Biederer, T. (2015). Topographic mapping of the synaptic cleft into adhesive nanodomains. *Neuron*, 88(6):1165–72.

[20] Diao, J., Burré, J., Vivona, S., Cipriano, D., Sharma, M., Kyoung, M., Südhof, T., and Brunger, A. (2013). Native α-synuclein induces clustering of synaptic-vesicle mimics via binding to phospholipids and synaptobrevin-2/vamp2. *eLife*, 2:e00592–e00592.

[21] Dresbach, T., Torres, V., Wittenmayer, N., Altrock, W. D., Zamorano, P., Zuschratter, W., Nawrotzki, R., Ziv, N. E., Garner, C. C., and Gundelfinger, E. D. (2006). Assembly of active zone precursor vesicles: obligatory trafficking of presynaptic cytomatrix proteins bassoon and piccolo via a trans-golgi compartment. *The Journal of biological chemistry*, 281:6038.

[22] Dubochet, J., Adrian, M., Chang, J.-J., Homo, J.-C., Lepault, J., McDowall, A., and Schultz, P. (1988). Cryo-electron microscopy of vitrified specimen. *Quaterly Review of Biophysics*, 21(2):129–228.

[23] Dunkley, P., Jarvie, P., and Robinson, P. (2008). A rapid percoll gradient procedure for preparation of synaptosomes. *Nature Protocols*, 3(11):1718–28.

[24] Faas, F. G. A., Bárcena, M., Agronskaia, A. V., Gerritsen, H. C., Moscicka, K. B., Diebolder, C. A., van Driel, L. F., Limpens, R. W. A. L., Bos, E., Ravelli, R. B. G., Koning, R. I., and Koster, A. J. (2013). Localization of fluorescently labeled structures in frozen-hydrated samples using integrated light electron microscopy. *Journal of structural biology*, 181(3):283–90.

[25] Fejtova, A., Davydova, D., Bischof, F., Lazarevic, V., Altrock, W., Romorini, S., Schne, C., Zuschratter, W., Kreutz, M., Garner, C., Ziv, N., and Gundelfinger, E. (2009). Dynein light chain regulates axonal trafficking and synaptic levels of bassoon. *The journal of cell biology*, 185(2):341–355.

[26] Fernandez, J., Li, S., and Crowther, R. (2006). Ctf determination and correction in electron cryotomography. *Ultramicroscopy*, 106(7):587–596.

[27] Fernandez, J. J. (2009). Tomobflow: feature-preserving noise filtering for electron tomography. *BMC bioinformatics*, 10:178.

[28] Fernandez, J. J. and Li, S. (2003). An improved algorithm for anisotropic nonlinear diffusion for denoising cryo-tomograms. *Journal of structural biology*, 144:152.

[29] Fernandez-Busnadiego, R., Zuber, B., Maurer, U., Cyrklaff, M., Baumeister, W., and Lucic, V. (2010). Quantitative analysis of the native presynaptic cytomatrix by cryoelectron tomography. *The journal of cell biology*, 188(1):145–156.

[30] Fernández-Buznadiego, R. (2010). *Structural Analysis of Presynaptic Architecture by Cryoelectron Tomography*. PhD thesis, Departement of Structural Molecular Biology, MPI of Biochemistry (Technische Universität München).

[31] Fogel, A., Akins, M., Krupp, A., Stagi, M., Stein, V., and Biederer, T. (2007).

Syncams organize synapses through heterophilic adhesion. *The Journal of neuroscience*, 27(46):12516–30.

[32] Fogel, A., Li, Y., Giza, J., Wang, Q., Lam, T., Modis, Y., and Biederer, T. (2010). N-glycosylation at the syncam (synaptic cell adhesion molecule) immunoglobulin interface modulates synaptic adhesion. *Journal of biological chemistry*, 285(45):34864–74.

[33] Fu, Z., Washbourne, P., Ortinski, P., and Vicini, S. (2003). Functional excitatory synapses in hek293 cells expressing neuroligin and glutamate receptors. *Journal of neurophysiology*, 90(6):3950–7.

[34] Gaffield, M. and Betz, W. (2006). Imaging synaptic vesicle exocytosis and endocytosis with fm dyes. *Nature Protocols*, 1(6):2916–21.

[35] Garner, C. C., Waites, C. L., and Ziv, N. E. (2006). Synapse development: still looking for the forest, still lost in the trees. *Cell and tissue research*, 326:249.

[36] Garvalov, B., Zuber, B., Bouchet-Marquis, C., Kudryashev, M., Gruska, M., Beck, M., Leis, A., Frischknecht, F., Bradke, F., Baumeister, W., Dubochet, J., and Cyrklaff, M. (2006). Luminal particles within cellular microtubules. *The Journal of cell biology*, 174(6):759–765.

[37] Gerrow, K., Romorini, S., Nabi, S., Colicos, M., Sala, C., and El-Husseini, A. (2006). A preformed complex of postsynaptic proteins is involved in excitatory synapse development. *Neuron*, 49(4):547–562.

[38] Grabrucker, A., Vaida, B., Bockmann, J., and Boeckers, T. (2009). Synaptogenesis of hippocampal neurons in primary cell culture. *Cell Tissue Res*, 338.

[39] Greten-Harrison, B., Polydoro, M., Morimoto-Tomita, M., Diao, L., Williams, A. M., Nie, E. H., Makani, S., Tian, N., Castillo, P. E., Buchman, V. L., et al. (2010). $\alpha\beta\gamma$-synuclein triple knockout mice reveal age-dependent neuronal dysfunction. *Proceedings of the National Academy of Sciences*, 107(45):19573–19578.

[40] Harris, K. and Weinberg, R. (2012). Ultrastructure of synapses in the mammalian brain. *Cold Spring Harbor perspectives in biology*, 4(5).

[41] Hegerl, R. (1996). The em program package: A platform for image processing in biological electron microscopy. *Journal of structural biology*, 116(1):30–34.

[42] Helenius, J., Brouhard, G., Kalaidzidis, Y., Diez, S., and Howard, J. (2006). The depolymerizing kinesin mcak uses lattice diffusion to rapidly target microtubule ends. *Nature*, 441(7089):115–9.

[43] Hjorth, J., Blackwell, K., and Kotaleski, J. (2009). Gap junctions between striatal fast-spiking interneurons regulate spiking activity and synchronization as a function of cortical activity. *The journal of neuroscience*, 29(16):5276–5286.

[44] Hoppe, W., Gassmann, J., Hunsmann, N., Schramm, H. J., and Sturm, M. (1974). Three-dimensional reconstruction of individual negatively stained yeast fatty-acid synthetase molecules from tilt series in the electron microscope. *Hoppe-Seyler's Zeitschrift für physiologische Chemie*, 355(11):1483–1487.

[45] Hoppe, W. and Hegerl, R. (1976). Influence of electron noise on three-dimensional image reconstruction. *Zeitschrift für Naturforschung. Teil A, Physik, physikalische Chemie, Kosmophysik*, 314(12):1717–1721.

[46] Huang, B., Wang, W., Bates, M., and Zhuang, X. (2008). Three-dimensional super-resolution imaging by stochastic optical reconstruction microscopy. *Science*, 319(5864):810–3.

[47] Jankovic, J. (2008). Parkinson's disease: clinical features and diagnosis. *Journal of Neurology, Neurosurgery & Psychiatry*, 79(4):368–376.

[48] Jensen, P. H., Nielsen, M. S., Jakes, R., Dotti, C. G., and Goedert, M. (1998). Binding of alpha-synuclein to brain vesicles is abolished by familial parkinson's disease mutation. *Journal of biological chemistry*, 273(41):26292–4.

[49] Kaech, S. and Banker, G. (2006). Culturing hippocampal neurons. *Nat Protoc*, 1:2406–15.

[50] Knoll, M. and Ruska, E. (1932). Das elektronenmikroskop. *Zeitschrift fÃ¼r Physik A Hadrons and Nuclei*, 78(5):318–339.

[51] Koenig, E., Kinsman, S., Repasky, E., and Sultz, L. (1985). Rapid mobility of motile varicosities and inclusions containing alpha-spectrin, actin, and calmodulin in regenerating axons in vitro. *The journal of neuroscience*, 5(3):715–729.

[52] Korinek, A., Beck, F., Baumeister, W., Nickell, S., and Plitzko, J. (2011). Computer controlled cryo-electron microscopy–tom^2 a software package for high-throughput applications. *Journal of structural biology*, 175(3):394–405.

[53] Kremer, J. R., Mastronarde, D. N., and McIntosh, J. R. (1996). Computer visualization of three-dimensional image data using imod. *Journal of structural biology*, 116(1):71–6.

[54] Krueger, S., Kolar, A., and Fitzsimonds, R. (2003). The presynaptic release apparatus is functional in the absence of dendritic contact and highly mobile within isolated axons. *Neuron*, 40(5):945–957.

[55] Krüger, R., Kuhn, W., Müller, T., Woitalla, D., Graeber, M., Kösel, S., Przuntek, H., Epplen, J. T., Schöls, L., and Riess, O. (1998). Ala30pro mutation in the gene encoding alpha-synuclein in parkinson's disease. *Nature Genetics*, 18(2):106–8.

[56] Kwon, H.-B., Kozorovitskiy, Y., Oh, W.-J., Peixoto, R. T., Akhtar, N., Saulnier, J. L., Gu, C., and Sabatini, B. L. (2012). Neuroligin-1-dependent competition regulates cortical synaptogenesis and synapse number. *Nature neuroscience*, 15(12):1667–74.

[57] Lau, T., Gage, G., Berke, J., and Zochowski, M. (2010). Local dynamics of gap-junction-coupled interneuron networks. *Physical biology*, 7:16015–16015.

[58] Lucic, V. and Baumeister, W. (2005). Neuroscience. monte carlo places strong odds on ectopic release. *Science (New York, N.Y.)*, 309:387.

[59] Lucic, V., Kossel, A. H., Yang, T., Bonhoeffer, T., Baumeister, W., and Sartori, A. (2007). Multiscale imaging of neurons grown in culture: from light microscopy to cryo-electron tomography. *Journal of structural biology*, 160:146.

[60] Lucic, V., Yang, T., Schweikert, G., Forster, F., and Baumeister, W. (2005). Morphological characterization of molecular complexes present in the synaptic cleft. *Structure (London, England : 1993)*, 13:423.

[61] Luk, K. C., Kehm, V., Carroll, J., Zhang, B., O'Brien, P., Trojanowski, J. Q., and Lee, V. M.-Y. (2012). Pathological α-synuclein transmission initiates parkinson-like neurodegeneration in nontransgenic mice. *Science*, 338(6109):949–53.

[62] MacGillavry, H., Song, Y., Raghavachari, S., and Blanpied, T. (2013). Nanoscale scaffolding domains within the postsynaptic density concentrate synaptic ampa receptors. *Neuron*, 78(4):615–22.

[63] Malkinson, G., Fridman, Z., Kamber, D., Dormann, A., Shapira, E., and Spira, M. (2006). Calcium-induced exocytosis from actomyosin-driven, motile varicosities formed by dynamic clusters of organelles. *Brain Cell Biology*, 35(1):57–73.

[64] Marston, D. J., Dickinson, S., and Nobes, C. D. (2003). Rac-dependent trans-endocytosis of ephrinbs regulates eph-ephrin contact repulsion. *Nature Cell Biology*, 5(10):879–88.

[65] McLaughlin, T., Hindges, R., Yates, P. A., and O'Leary, D. D. M. (2003). Bifunctional action of ephrin-b1 as a repellent and attractant to control bidi-

rectional branch extension in dorsal-ventral retinotopic mapping. *Development*, 130(11):2407–18.

[66] Mizuno, N., Varkey, J., Kegulian, N. C., Hegde, B. G., Cheng, N., Langen, R., and Steven, A. C. (2012). Remodeling of lipid vesicles into cylindrical micelles by α-synuclein in an extended α-helical conformation. *Journal of Biological Chemistry*, 287(35):29301–29311.

[67] Murk, J. L. A. N., Humbel, B. M., Ziese, U., Griffith, J. M., Posthuma, G., Slot, J. W., Koster, A. J., Verkleij, A. J., Geuze, H. J., and Kleijmeer, M. J. (2003). Endosomal compartmentalization in three dimensions: implications for membrane fusion. *Proceedings of the National Academy of Sciences of the United States of America*, 100(23):13332–13337.

[68] Nakata, T., Terada, S., and Hirokawa, N. (1998). Visualization of the dynamics of synaptic vesicle and plasma membrane proteins in living axons. *The Journal of cell biology*, 140:659.

[69] Nemani, V., Lu, W., Berge, V., Nakamura, K., Onoa, B., Lee, M., Chaudhry, F., Nicoll, R., and Edwards, R. (2010). Increased expression of alpha-synuclein reduces neurotransmitter release by inhibiting synaptic vesicle reclustering after endocytosis. *Neuron*, 65(1):66–79.

[70] Nickell, S., Frster, F., Linaroudis, A., Net, W. D., Beck, F., Hegerl, R., Baumeister, W., and Plitzko, J. (2005). Tom software toolbox: acquisition and analysis for electron tomography. *Journal of structural biology*, 149(3):227–234.

[71] Ordenstein, L. (1868). *Sur la paralysie agitante et la sclérose en plaques généralisée.* Delahaye.

[72] Parkinson, J. (1817). The shaking palsy. *Sherwood, Neely and Jones, London.*

[73] Pasquale, E. B. (2005). Eph receptor signalling casts a wide net on cell behaviour. *Nature reviews. Molecular cell biology*, 6(6):462–75.

[74] Peters, A., Palay, S. L., et al. (1976). *Fine structure of the nervous system.* Saunders.

[75] Pranke, I. M., Morello, V., Bigay, J., Gibson, K., Verbavatz, J.-M., Antonny, B., and Jackson, C. L. (2011). α-synuclein and alps motifs are membrane curvature sensors whose contrasting chemistry mediates selective vesicle binding. *The Journal of cell biology*, 194(1):89–103.

[76] Pringsheim, T., Jette, N., Frolkis, A., and Steeves, T. D. L. (2014). The prevalence of parkinson's disease: a systematic review and meta-analysis. *Movement disorders*, 29(13):1583–90.

[77] Radon, J. (1917). über die bestimmung von funktionen durch ihre integralwerte längs gewisser mannigfaltigkeiten. *Berichte Sächsische Akademie der Wissenschaften, Leipzig, Mathematisch-Physikalische Klasse*, 69:262–277.

[78] Reimer, H. K. L. (2008). *Transmission Electron Microscopy, 5th Ed.* Springer, fifth edition edition.

[79] Rigort, A., Bäuerlein, F. J. B., Leis, A., Gruska, M., Hoffmann, C., Laugks, T., Böhm, U., Eibauer, M., Gnaegi, H., Baumeister, W., and Plitzko, J. (2010). Micromachining tools and correlative approaches for cellular cryo-electron tomography. *Journal of structural biology*, 172(2):169–79.

[80] Rigort, A., Günther, D., Hegerl, R., Baum, D., Weber, B., Prohaska, S., Medalia, O., Baumeister, W., and Hege, H.-C. (2012). Automated segmentation of electron tomograms for a quantitative description of actin filament networks. *Journal of structural biology*, 177(1):135–44.

[81] Robbins, E. M., Krupp, A. J., de Arce, K. P., Ghosh, A. K., Fogel, A. I., Boucard, A., Sãdhof, T. C., Stein, V., and Biederer, T. (2010). Syncam 1 adhesion dynamically regulates synapse number and impacts plasticity and learning. *Neuron*, 68(5):894–906.

[82] Roberts, T., Tschida, K., Klein, M., and Mooney, R. (2010). Rapid spine stabilization and synaptic enhancement at the onset of behavioural learning. *Nature*, 463(7283):948–52.

[83] Sabatini, B. L., Maravall, M., and Svoboda, K. (2001). Ca(2+) signaling in dendritic spines. *Current Opinion in Neurobiology*, 11(3):349–56.

[84] Schweikert, G. (2004). *Quantitativer Vergleich der Strahlschädigung biologischer Proben im Transmissions-Elektronenmikroskop bei Stickstoff- und Helium-Temperatur*. PhD thesis, Departement of Structural Molecular Biology, MPI of Biochemistry (Technische Universität München).

[85] Shapira, M., Zhai, R. G., Dresbach, T., Bresler, T., Torres, V., Gundelfinger, E., Ziv, N., and Garner, C. (2003). Unitary assembly of presynaptic active zones from piccolo-bassoon transport vesicles. *Neuron*, 38(2):237–52.

[86] Shepherd, G. M. and Harris, K. M. (1998). Three-dimensional structure and composition of ca3–>ca1 axons in rat hippocampal slices: implications for presynaptic connectivity and compartmentalization. *The journal of neuroscience*, 18(20):8300–8310.

[87] Shepherd, G. M. and Raastad, M. (2003). Axonal varicosity distributions

along parallel fibers: a new angle on a cerebellar circuit. *Cerebellum (London, England)*, 2:110.

[88] Shipman, S. L. and Nicoll, R. A. (2012). Dimerization of postsynaptic neuroligin drives synaptic assembly via transsynaptic clustering of neurexin. *Proceedings of the National Academy of Sciences of the United States of America*, 109(47):19432–7.

[89] Sorra, K. E., Mishra, A., Kirov, S. A., and Harris, K. M. (2006). Dense core vesicles resemble active-zone transport vesicles and are diminished following synaptogenesis in mature hippocampal slices. *Neuroscience*, 141(4):2097–106.

[90] Stagi, M., Fogel, A. I., and Biederer, T. (2010). Syncam 1 participates in axodendritic contact assembly and shapes neuronal growth cones. *Proceedings of the National Academy of Sciences of the United States of America*, 107(16):7568–73.

[91] Su, Q., Cai, Q., Gerwin, C., Smith, C., and Sheng, Z.-H. (2004). Syntabulin is a microtubule-associated protein implicated in syntaxin transport in neurons. *Nature Cell Biology*, 6(10):941–53.

[92] Sui, H. and Downing, K. (2010). Structural basis of interprotofilament interaction and lateral deformation of microtubules. *Structure*, 18(8):1022–31.

[93] Tanaka, H., Miyazaki, N., Matoba, K., Nogi, T., Iwasaki, K., and Takagi, J. (2012). Higher-order architecture of cell adhesion mediated by polymorphic synaptic adhesion molecules neurexin and neuroligin. *Cell Reports*, 2(1):101–110.

[94] Ulmer, T., Bax, A., Cole, N., and Nussbaum, R. (2005). Structure and dynamics of micelle-bound human alpha-synuclein. *Journal of biological chemistry*, 280(10):9595–9603.

[95] Unverdorben, P., Beck, F., Śledź, P., Schweitzer, A., Pfeifer, G., Plitzko, J., Baumeister, W., and Förster, F. (2014). Deep classification of a large cryo-em dataset defines the conformational landscape of the 26s proteasome. *Proceedings of the National Academy of Sciences of the United States of America*, 111(15):5544–9.

[96] van de Linde, S., Löschberger, A., Klein, T., Heidbreder, M., Wolter, S., Heilemann, M., and Sauer, M. (2011). Direct stochastic optical reconstruction microscopy with standard fluorescent probes. *Nature Protocols*, 6(7):991–1009.

[97] Varkey, J., Isas, J., Mizuno, N., Jensen, M., Bhatia, V., Jao, C., Petrlova, J., Voss, J., Stamou, D., Steven, A., and Langen, R. (2010). Membrane curvature

induction and tubulation are common features of synucleins and apolipoproteins. *Journal of biological chemistry*, 285(42):32486–32493.

[98] Vaughn, J. E. (1989). Fine structure of synaptogenesis in the vertebrate central nervous system. *Synapse (New York, N.Y.)*, 3:255.

[99] Waites, C. L., Craig, A. M., and Garner, C. C. (2005). Mechanisms of vertebrate synaptogenesis. *Annu. Rev. Neurosci.*, 28:251–274.

[100] Westphal, V., Rizzoli, S. O., Lauterbach, M. A., Kamin, D., Jahn, R., and Hell, S. W. (2008). Video-rate far-field optical nanoscopy dissects synaptic vesicle movement. *Science (New York, N.Y.)*, 320:246.

[101] Wittenmayer, N., Krber, C., Liu, H., Kremer, T., Varoqueaux, F., Chapman, E., Brose, N., Kuner, T., and Dresbach, T. (2009). Postsynaptic neuroligin1 regulates presynaptic maturation. *Proceedings of the National Academy of Sciences of the United States of America*, 106(32):13564–13569.

[102] Xu, K., Zhong, G., and Zhuang, X. (2013). Actin, spectrin, and associated proteins form a periodic cytoskeletal structure in axons. *Science*, 339(6118):452–6.

[103] Xu, N.-J. and Henkemeyer, M. (2012). Ephrin reverse signaling in axon guidance and synaptogenesis. In *Seminars in cell & developmental biology*, volume 23, pages 58–64. Elsevier.

[104] Zanetti, G., Riches, J., Fuller, S., and Briggs, J. A. G. (2009). Contrast transfer function correction applied to cryo-electron tomography and sub-tomogram averaging. *Journal of structural biology*, 168(2):305–312.

[105] Zhai, R., Olias, G., Chung, W. J., Lester, R. A., Dieck, S. T., Langnaese, K., Kreutz, M. R., Kindler, S., Gundelfinger, E. D., and Garner, C. C. (2000). Temporal appearance of the presynaptic cytomatrix protein bassoon during synaptogenesis. *Molecular and cellular neurosciences*, 15(5):417–428.

[106] Zhai, R. G., Vardinon-Friedman, H., Cases-Langhoff, C., Becker, B., Gundelfinger, E. D., Ziv, N. E., and Garner, C. C. (2001). Assembling the presynaptic active zone: A characterization of an active zone precursor vesicle. *Neuron*, 29:131–143.

List of Figures